The segregation of Indium from polycrystalline Copper crystals

by

Moshawe Jack Madito

B.Sc Hons.

A thesis presented in fulfillment of the requirements for the degree

MAGISTER SCIENTIAE

in the Faculty of Natural and Agricultural Sciences,
Department of Physics,
at the University of the Free State,
Republic of South Africa.

Supervisor: **Prof. J.J. Terblans**

Co-supervisor: **Prof. H.C. Swart**

Submitted: **February 2012**

Acknowledgements

The author wishes to express his sincere appreciation to Prof. H.C. Swart and Prof. J.J. Terblans, the author's promoters, for their patience, support and great ideas in the field of this study, the personnel of the Department of Physics (UFS), for their advices and interest in this study, the National Research Foundation (NRF), the Cluster program of the University of the Free State and the Inkaba yeAfrica programme for financial assistance.

Key Words

- Diffusion
- Fick's model
- Equilibrium segregation
- In diffusion in Cu
- In segregation energy
- S diffusion in Cu
- S segregation energy
- In-Cu alloy system
- Polycrystalline Cu crystal
- e-beam evaporation of In
- Auger Electron Spectroscopy
- X-ray diffraction

Acronyms

- **UHV**: Ultra-high vacuum
- **APPH**: Auger peak to peak height
- **ppm**: Parts per million
- **SIMS**: Secondary-ion mass spectrometry
- ***e*-beam**: electron beam
- **AES**: Auger electron spectroscopy
- **XRD**: X-ray diffraction
- **JCPDS**: International Centre for Diffraction Data
- **CMA**: Cylindrical mirror analyzer
- **SED**: Secondary electron detector
- **FWHM**: Full width at half maximum

Abstract

In this study the surface segregation of In from a dilute Cu(In) alloy to the surface was investigated. The Cu(In) alloy was prepared by diffusion doping. A thin layer of In was deposited onto the backside of a polycrystalline Cu crystal. The In layer was covered with a thin Cu layer to prevent the In from melting and evaporating from the Cu crystal. The Cu crystal was annealed in an Ar gas atmosphere. During annealing the temperature was increased stepwise from 150 ℃ to 900 ℃ to prevent the In layer from melting. Finally the Cu crystal was annealed at 900 ℃ for 456 hours. As a result, the polycrystalline Cu crystal was successfully doped with an In concentration of 0.059 at%.

Using Auger electron spectroscopy (AES) coupled with an Ar^+ ion gun (for surface sputter cleaning) and a programmed crystal heater inside the ultra high vacuum (UHV) chamber, the segregation profiles where recorded by monitoring the surface condition of In and S on the Cu crystal during linear heating and constant temperatures heating.

The constant temperature segregation measurements were performed in the temperature range 460 ℃ to 580 ℃. The segregation profiles showed that both In and S segregates from the Cu crystal. In segregates to the surface at a much higher rate than S. In reached a maximum surface coverage of $\approx$ 25 % for the temperatures 460 ℃, 490 ℃ and 520 ℃ and $\approx$ 16 % for temperatures 550 ℃ and 580 ℃. Both the In and S segregation profiles were fitted with semi-infinite solution of Fick's equation and the segregation parameters (Q and D_0) were

obtained for In as $Q = 191.9$ kJ.mol^{-1}, $D_0 = 1.1 \times 10^{-5}$ m^2.s^{-1} and for S as $Q = 201.1$ kJ.mol^{-1}, $D_0 = 4.4 \times 10^{-2}$ m^2.s^{-1}.

The linear temperature measurements were carried out from the temperature range 100 ℃ to 800 ℃ at heating rates of 0.025; 0.05; 0.1 and 0.2 ℃.s^{-1}. All segregation profiles showed In segregation to the surface that reached a surface maximum coverage of 23−25 %. The segregation of In was accompanied by a slow segregating S that replaced the In completely from the surface. The surface concentration of In reached a maximum coverage of 29−32 %. The replacement of In by S is due to a large difference between the segregation energies of In and S with S having the more negative segregation energy. The segregation profiles were fitted with the modified semi-infinity model of Fick to obtain the segregation parameters (pre-exponential factor (D_0) and activation energy (Q)). The segregation profiles were also fitted with the Guttmann model to obtain the segregation energies (ΔG) and interaction energies (Ω) for In and S segregation in Cu. Finally, using segregation parameters obtained from these fits (Fick and Guttmann) the segregation profiles were fitted with modified Darken model to yield the segregation parameters for In and S segregation in Cu crystal. The segregation parameters for In that were obtained were $Q = 184.1$ kJ.mol^{-1}, $D_0 = 1.6 \times 10^{-5}$ m^2.s^{-1}, $\Delta G = -60.4$ kJ.mol^{-1} and $\Omega_{\text{In-Cu}} = 3.0$ kJ.mol^{-1}. The segregation parameters for S that were obtained were $Q = 212.4$ kJ.mol^{-1}, $D_0 = 9.1 \times 10^{-3}$ m^2.s^{-1}, $\Delta G = -120.0$ kJ.mol^{-1}, $\Omega_{\text{S-Cu}} = 23.0$ kJ.mol^{-1}. The interaction energy for In and S was determined as $\Omega_{\text{In-S}} = -4.0$ kJ.mol^{-1}.

The segregation parameters (Q and D_0) obtained in this study for In segregation from a Cu crystal compare well with those reported in literature for In tracer

diffusion in a Cu(In) bulk system. The segregation parameters (Q and D_0) obtained in this study for S compare well with those reported in literature for both S segregation from a Cu crystal and S tracer diffusion in a Cu(S) bulk system.

Table of Contents

1

Introduction

Segregation is the exchange of atoms between the surface layer and the bulk layers until the total energy of the crystal is lowest (the equilibrium is reached). Segregation result from bulk diffusion and the driving force behind diffusion is the concentration gradient according to Fick. According to Darken, the chemical potential gradient is the driving force behind diffusion of atoms from a region of high chemical potential (bulk) to a region of low chemical potential (surface). As a result of segregation, impurities with concentrations in the order of few parts per million (ppm) can reach high concentrations at the surface or an interface.

The segregation of impurities to surfaces and interfaces can influence the physical and chemical properties of the alloy. For instance, segregation to grain boundaries influences the bonds at grain boundaries that influence the strength and hardness of a material. Segregation to the surface influences the corrosion property of the material.

Today technology is shrinking transistors and integrated circuits to improve the performance of micro-chips. An Al alloy is used as gate and interconnect material in thin-film transistor liquid-crystal display (TFT-LCD) and in ultra-large-scale integrated (ULSI) devices because Al can form a protective oxide layer on the surface that prevent further Al oxidation [1, 2, 3]. However, Al suffers from electromigration that influence the device performance and reliability. Due to Cu's excellent electrical properties Cu is a promising substitute of Al [1]. However, Cu cannot form a protective oxide layer on the surface. Note that the Al-doped Cu improves oxidation resistance, but the resistivity of Al-doped Cu is higher than that of pure Cu [3]. In has a higher oxygen affinity than Cu and it also improves the adhesion of Cu on glass [2]. Therefore, surface segregation of In in In-doped Cu will form an In oxide layer on the Cu surface that will protect Cu during oxidation. In-doped Cu with In segregation is a promising material for applications in LCDs and ULSI devices.

Multicomponent segregation can play a very significant role to engineer the composition at grain boundaries during heat treatments to meet industrial requirements. Single and multicomponent segregation of Sb, Sn, S, Ag and Bi in a Cu crystal were experimentally investigated [4, 5, 6, 7, 8]. However, In segregation in Cu has not received attention. According to the author's best knowledge and an extensive literature survey on In-Cu systems no bulk-to-surface segregation study of In in a dilute Cu(In) system has been done. Therefore, this study is most likely the first to report on the segregation of In in a dilute Cu(In) system. Nevertheless, In tracer diffusion in a Cu(In) bulk system was investigated by Krautheim *et al.* [9], Gorbachev *et al.* [10] and Gust *et al.* [11].

1.1 The objectives of the study

The main objective of this study is to investigate the segregation behaviour of In from a Cu crystal. This will be made possible by the following objectives (in sequence).

1. Dope a polycrystalline Cu crystal with small fraction of In ($\sim$ 0.1 at% In).
    - i. The doping process is carried out at high annealing temperature of 900 ℃. This annealing temperature is above the melting point of In (156.6 ℃) and it will cause In to melt and wet the crystal and most likely evaporate. To overcome this problem the following will be done.
        - a. The In layer will be covered with a Cu layer and annealed at a low temperature to form intermetallic phases ($\mathrm{Cu}_x\mathrm{In}_y$) with higher melting points. The annealing temperature will be increased stepwise without melting the In layer and $\mathrm{Cu}_x\mathrm{In}_y$ phases until the final annealing temperature (900 ℃).
2. Heat the Cu crystal at both constant temperatures and linear temperatures while monitoring the surface of the Cu crystal with Auger electron spectroscopy (AES) to measure the segregation of In.
3. Obtain the segregation parameters, namely the pre-exponential factor (D_0), activation energy (Q), segregation energy (ΔG) and interaction energy (Ω) for In segregation from a Cu crystal.

1.2 Layout of the thesis

Chapter 1: An overview of the segregation process, studies done on Cu crystal and the objectives of this study.

Chapter 2: An overview of the phase diagram of the Cu/In system and the intermetallic compounds that form during In-Cu thin films growth.

Chapter 3: This is a summary of the diffusion theory that includes the diffusion mechanisms and Fick's equation.

Chapter 4: A brief overview on the theory of thermodynamics during surface segregation and the theoretical models that are used to simulate segregation.

Chapter 5: An overview of all the techniques and procedures used in this study.

Chapter 6: A discussion on the results obtained for both In/Cu thin films and Cu(In) segregation results.

Chapter 7: A conclusive summary of the experimental results obtained in this study.

Part I

THEORY

2

Overview of the Cu-In system

2.1 Introduction

Metallic In (body centered tetragonal (BCT)) is ductile and malleable. In general, In improves strength, hardness, and corrosion resistance of alloys [12]. Indium is produced mainly from residues generated during zinc ore processing but is also found in iron, lead, and copper ores [12]. The melting point of In is 156.6 ℃ [13].

Cu (face centered cubic (FCC)) is a ductile metal, with very high thermal and electrical conductivity. Cu is extracted from Cu ore which is mined or extracted as Cu sulfides. Cu has a melting point of 1084.6 ℃ [13].

Lately, most investigations of the Cu-In system have focused on thin films particularly for applications of solar cells, thin-film transistor liquid-crystal display (TFT-LCD) and ultra-large-scale integrated (ULSI) devices [3, 14]. In the Cu/In system, In improves the adhesion of Cu on glass and provide Cu with a self-passivation layer under oxidizing conditions [15].

This chapter gives a brief discussion of previous work done on the Cu-In system.

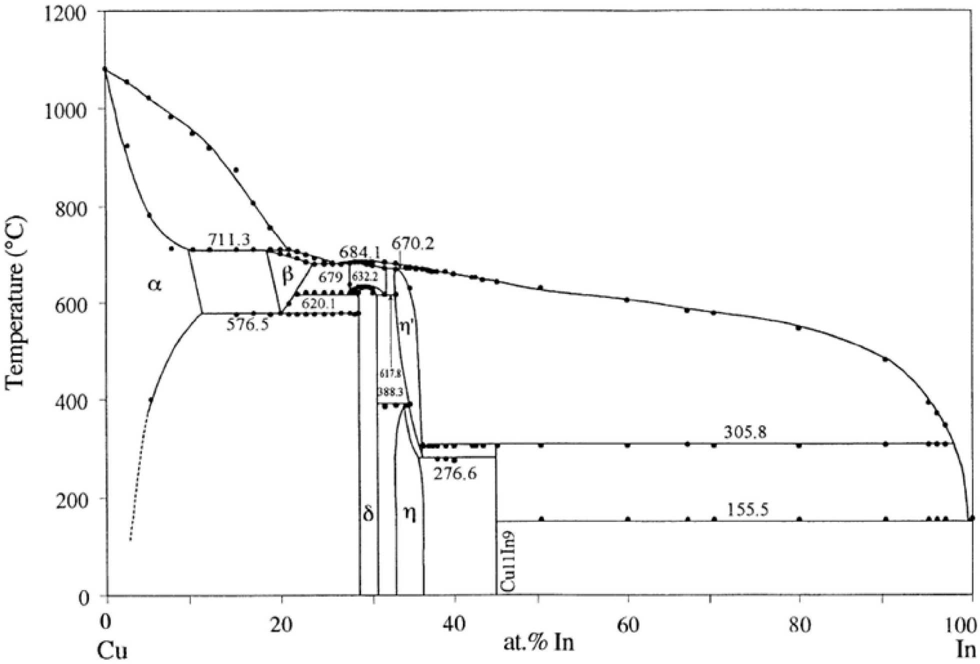

Figure 2.1: Cu-In equilibrium phase diagram [16].

2.2 Cu-In equilibrium phase diagram

The phase diagram in figure 2.1 is the phase diagram for a Cu-In system. From the phase diagram it is seen that there are two solid solutions regions. The first region is the αCu solution which has an In solubility ranging from 1.2 at% In at a temperature of 240 ℃ up to 11 at% In at temperature of about 560 ℃ and the second region is the In solid solution which is very close to pure In. Six stable intermediate phases shown in figure 2.1 are listed in table 2.1 and the melting temperatures of these phases [16]. These phases are crystalline and stronger but less ductile than In [17]. They can cause failures in applications that are sensitive to shock or thermal cycling. There are phases that exist in the Cu-In thin films that are not shown in the bulk phase diagram (Figure 2.1). For instance, the $CuIn_2$ phase that was observed in thin film system by Keppner [18].

Table 2.1: Six stable intermediate phases shown in figure 2.1 and the corresponding melting temperatures [16].

Phases	Melting temperatures (℃)
$Cu_{11}In_9$	305.8
η-Cu_2In	388.3
δ-Cu_7In_3	632.2
η'-Cu_2In	670.2
γ-Cu_7In_3	684.1
β-Cu_4In	711.3 and 679

2.3 Cu/In thin films interface reactions

Previous studies on the Cu-In thin films have reported the formation of $CuIn_2$ and $Cu_{11}In_9$ phases at room temperature [14, 19, 20, 21], in these studies the $Cu_{11}In_9$ was observed to form from $CuIn_2$ and Cu through solid state reaction in the In rich side of the Cu-In films [20]. It has also been found by Manna *et al.* [22], Vianco *et al.* [23] and Kim *et al.* [24] that the $Cu_{11}In_9$ intermetallic phase exists even at the interface between a bulk copper metal and a deposited thin layer of In.

After the first compound has formed ($CuIn_2$) from the starting metals (In and Cu) in the In rich side of Cu-In system, the formation of the next compound ($Cu_{11}In_9$) from the $CuIn_2$ compound and Cu material, takes place with $CuIn_2$ compound decomposition.

2.4 In diffusion in Cu(In) bulk system

The interdiffusion in Cu(In) bulk system was investigated by both Krautheim *et al.* [9] and Gorbachev *et al.* [10] using constant temperature measurements in the temperature range 778.0 to 1081.0 °C with tracers diffusion. In this investigations a polycrystalline Cu crystal and an $^{114\text{m}}$In isotope was used. The radioactivity of $^{114\text{m}}$In was measured using a scintillation counter from which the diffusion coefficients were worked-out to determine the diffusion parameters (pre-exponential factor D_o and the activation energy Q)(Table 2.2).

Table 2.2: Summary of the diffusion parameters found in the literature.

Source	Q (kJ.mol^{-1})	D_0 (m^2.s^{-1})
[9]	196.25 ± 3.09	$1.87(+ 0.66, - 0.49)\times10^{-4}$
[10]	193.47 ± 1.09	$1.30(+ 0.15, - 0.13)\times10^{-4}$
[11]	178.0 ± 6.0	$0.219(+ 0.386, - 0.140)\times10^{-4}$

Gust *et al.* [11] used secondary-ion mass spectrometry (SIMS) to study the bulk diffusion of indium in a copper crystal. The annealing temperatures for these measurements were in the range 329 to 1078 °C. In this case, a monocrystalline copper was used and the indium isotope $^{115\text{m}}$In as to give parameters, D_o and Q (Table 2.2), computed for the low temperature range only, $T \leq 600$ °C.

3

Diffusion in Metals

3.1 Introduction

Bulk diffusion in metals describes a random motion of atoms (with thermal energy as a driving force) from a region of high concentration to a region of low concentration.

Industrially, bulk diffusion plays an essential role in the manufacturing of materials, changing properties of certain materials by diffusing impurities to free surfaces and interfaces through heat treatment.

This chapter is a summary of the existing basic theory of impurity diffusion in metals.

3.2 Atom movement during diffusion

In metals, substitutional and interstitial diffusion are the dominating diffusion mechanisms. The diffusion of some impurities combines the two mechanisms. These two types of diffusion mechanisms are briefly discussed in this section.

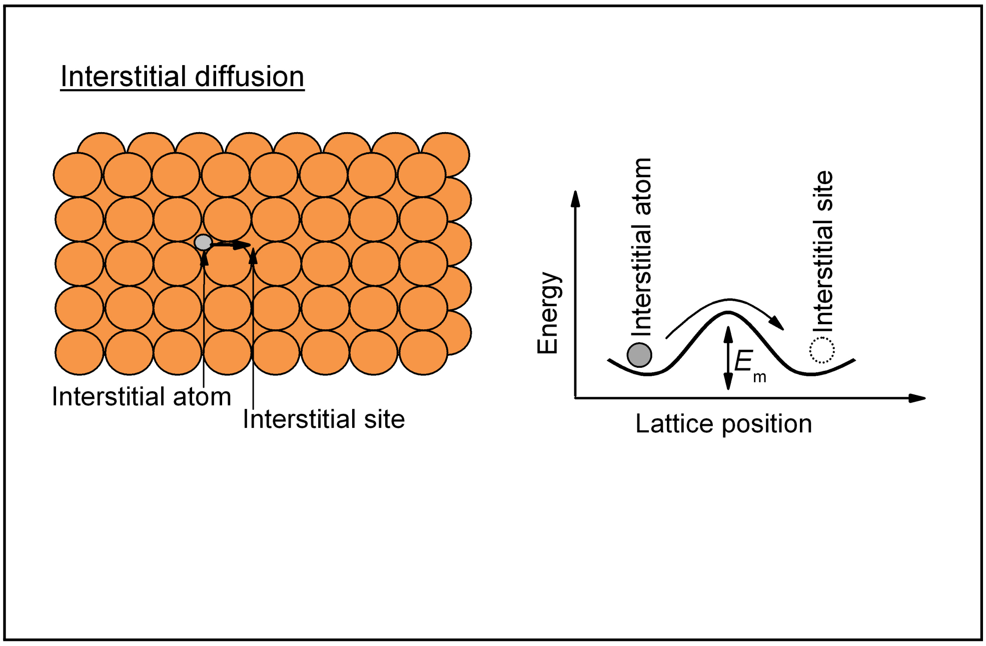

Figure 3.1: A schematic representation of the Interstitial diffusion mechanism.

3.2.1 Interstitial diffusion

Interstitial diffusion is the movement of an interstitial impurity from one interstitial site to another interstitial site (Figure 3.1). This diffusion mechanism is charecteristic of small atom impurities. For instance, the diffusion of C, N and H in Fe (FCC) is interstitial diffusion [25]. In Figure 3.1 it is also shown that for diffusion to take place the diffusing atom should have the migration energy E_m. The activation energy for diffusion in interstitial diffusion is equal to the migration energy.

3.2.2 Substitutional/Vacancy diffusion

During substitutional diffusion, atoms jumps from one lattice site to another vacant lattice site (Figure 3.2). The movement of atom into a vacant site corresponds to the movement of vacancy in the opposite direction. This diffusion

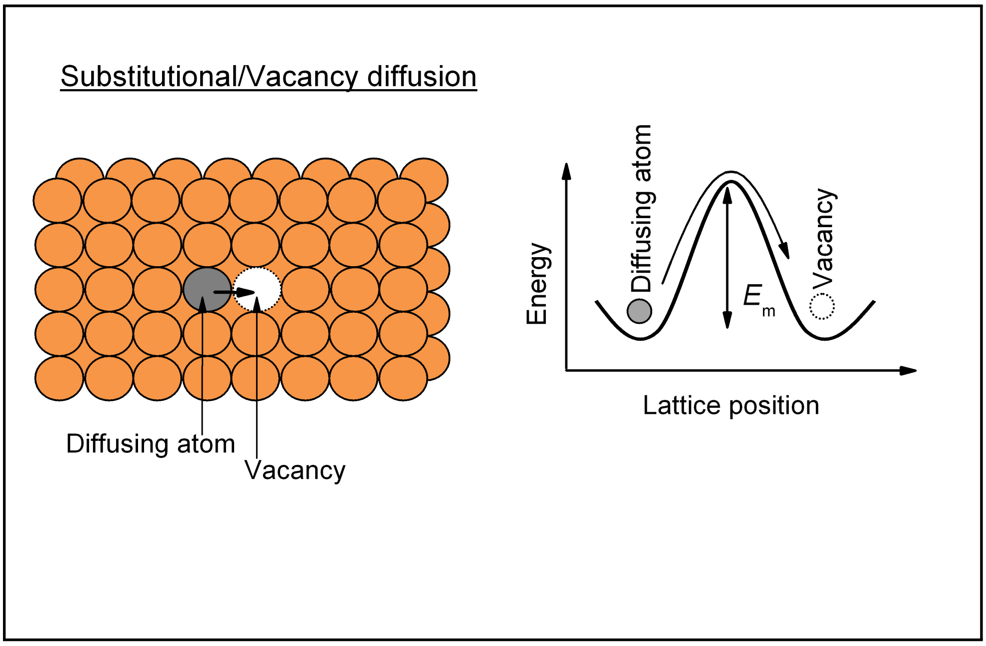

Figure 3.2: A schematic representation of the substitutional/vacancy diffusion mechanism.

mechanism is characteristic of impurity atoms that have similar atomic size as the matrix atoms. For instance, the diffusion of In ($a^{\infty}_{In} = 2.97\,\text{Å}$)[1] in Cu matrix ($a^{\infty}_{Cu} = 2.28\,\text{Å}$) will be substitutional whereby a Cu lattice site will be occupied by an In atom.

The number of thermal vacancies in the crystal is given by [25]

$$N_v = N_0 e^{(-E_v/RT)} \tag{3.1}$$

where N_0 is the amount of lattice positions in the crystal, E_v is vacancy formation energy, R is the universal gas constant and T is the temperature.

---

[1] Atom size from Seah [26]

The probability (P_v) that a vacancy is found next to a diffusing atom is:

$$\begin{aligned} P_v &= \frac{N_v}{N_0} \\ &= e^{(-E_v/RT)} \end{aligned} \tag{3.2}$$

and the probability (P_m) that a single atom will migrate from one position to adjacent vacancy is given by

$$P_m = e^{(-E_m/RT)}. \tag{3.3}$$

where E_m is atom migration energy.

Thus, the diffusion probability (P_D) is expressed as

$$P_D = P_m \times P_v. \tag{3.4}$$

From equation 3.4, the diffusion coefficient can be written as

$$D = kP_D \tag{3.5}$$

where k is a constant.

Taking k as pre-exponential factor and inserting equation 3.2 and 3.3 into equation 3.5, the following expression is obtained.

$$D = D_0 \left[e^{(-E_m/RT)}\right]_{P_m} \left[e^{(-E_v/RT)}\right]_{P_v} \tag{3.6}$$

Equation 3.6 can be written as

$$\begin{aligned} D &= D_0 e^{-(E_m+E_v)/RT} \\ &= D_0 e^{-Q/RT} \end{aligned} \tag{3.7}$$

where $Q = E_m + E_V$.

In equation 3.7 it can be seen that the diffusion coefficient of atoms depends on the atomic migration and vacancy formation energy. Hence, substitutional diffusion in a solid requires the presence of vacancies next to the diffusing (moving) atom. In equation 3.7, the diffusion coefficient varies with temperature.

The next section focuses on the Fick's equations and solutions.

3.3 Fick's second law

Fick's second law describes how diffusion causes the concentration to vary with position and time. Fick's second law is given by expression [25]

$$\frac{\partial C_x}{\partial t} = D\frac{\partial^2 C_x}{\partial x^2}, \tag{3.8}$$

where C_x is the concentration of the diffusing atoms at a position x after time t has elapsed, and D is the diffusion coefficient.

3.3.1 Fick's solution for finite systems

Using the following initial conditions [27]

$$C = C_0 \quad \text{for} \quad x \leq 0 \quad \text{and} \quad C = 0 \quad \text{for} \quad x > 0 \quad \text{at} \quad t = 0, \tag{3.9}$$

and boundary conditions [27]

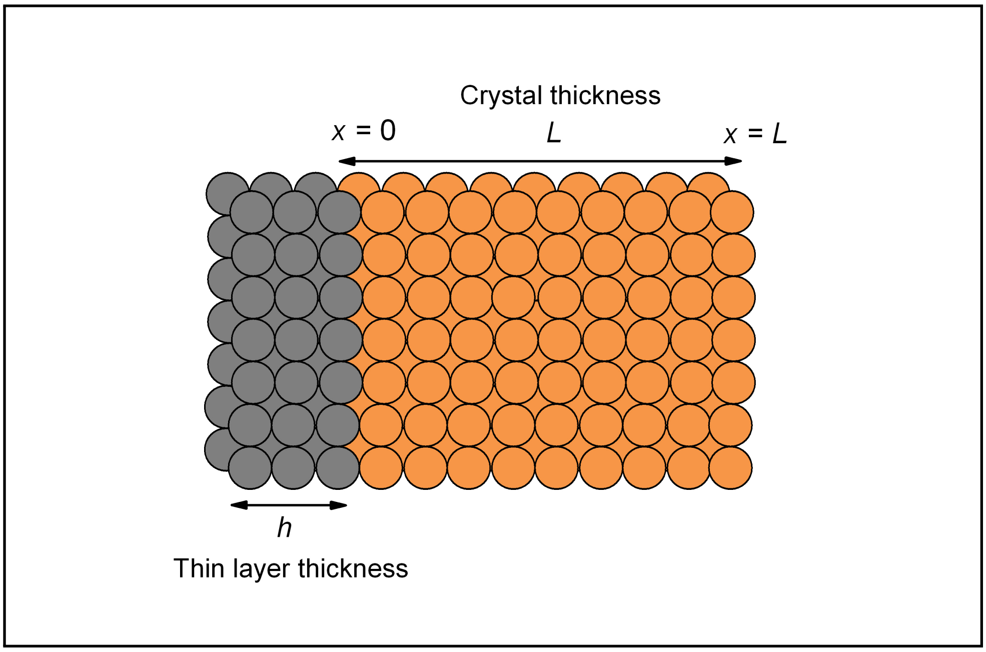

Figure 3.3: A schematic representation of the initial and boundary conditions.

$$\partial C/\partial x = 0 \quad \text{at} \quad x = L \quad \text{for} \quad t \geq 0. \tag{3.10}$$

With these conditions the solution to equation 3.8 is

$$C = C_0 \sum_{n=-\infty}^{\infty} \left[\operatorname{erf}\left(\frac{h + 2nL - x}{2\sqrt{Dt}}\right) + \operatorname{erf}\left(\frac{h - 2nL + x}{2\sqrt{Dt}}\right)\right] \tag{3.11}$$

where L is the crystal thickness with the surface at $x = 0$ and h is the thickness of a thin layer consisting of the diffusing atoms (see figure 3.3).

Equation 3.11 is most useful for calculating the concentration distribution in terms of diffusion depth x and time t.

3.3.2 Semi-infinite solution of Fick's equations

The semi-infinite solution of Fick's equations is used to calculates the surface concentration of the impurities that segregates (diffuse from the bulk to the surface) during segregation measurements. This solution is discussed in this chapter since is derived from the diffusion equation of Fick (Equation 3.8).

Using the initial conditions [28]

$$C = C^B \quad \text{for} \quad x > 0 \quad \text{and} \quad t = 0, \tag{3.12}$$

and boundary conditions [28]

$$C = 0 \quad \text{for} \quad x = 0 \quad \text{and} \quad t \geq 0, \tag{3.13}$$

a solution to equation 3.8 can also be written as [28]:

$$C^\phi = C^B \left[1 + \frac{2}{d} \left(\frac{Dt}{\pi} \right)^{\frac{1}{2}} \right]. \tag{3.14}$$

where C^ϕ is the surface concentration, C^B is the bulk concentration of impurities and d is the thickness of the segregated layer.

The initial condition and the boundary condition of equation 3.14 are based on the following assumptions [28]:

i. The initial surface concentration of the segregating atoms is equal to the bulk concentration C^B.

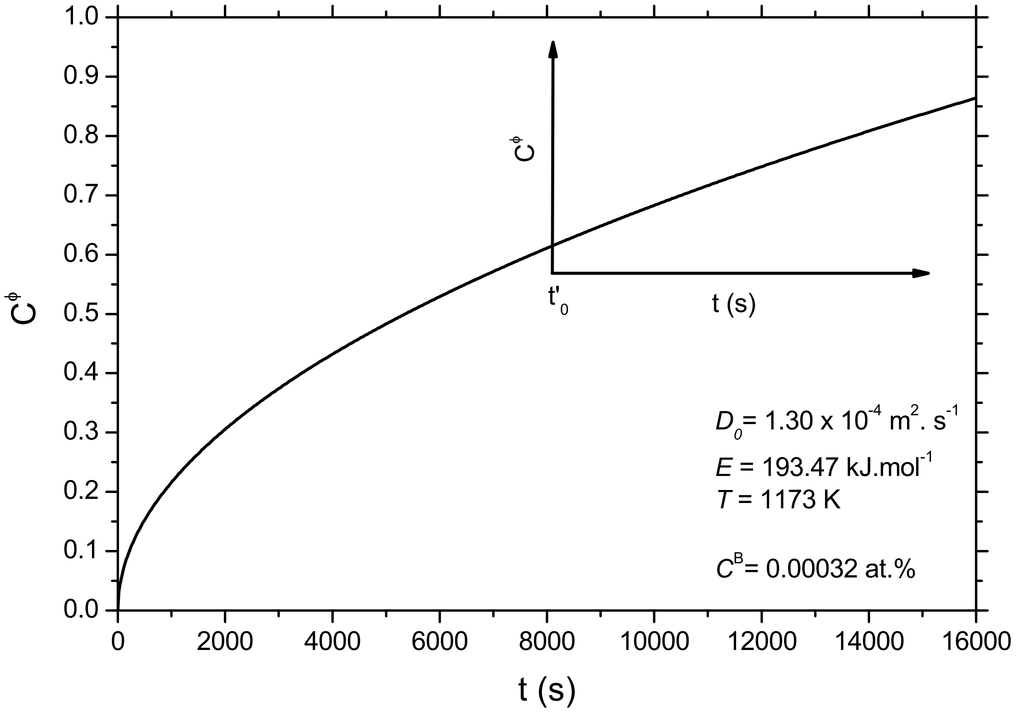

Figure 3.4: Plot of semi-infinite solution of Fick's equation.

ii. There is no interaction between segregating atoms.

Equation (3.14) describes the time dependence of the segregated surface concentration at a constant temperature (Figure 3.4).

Equation 3.14 is only valid under the following conditions [28]:

i. The initial bulk condition is a uniform concentration distribution.

ii. For a constant diffusion coefficient D at constant temperature T.

iii. Surface coverage relates to short times t.

In equation 3.14, the sputtering effects are not considered. To compensate for sputtering, Du Plessis *et al.* [29] modified equation 3.14 by defining the time scale when sputtering begin as t', sputter time as t'_0 and the time scale for the surface concentration measurements as t. The segregation start simultaneously with the sputtering at $t' = 0$ (Figure 3.4). When segregation starts the bulk concentration is uniform and the temperature is constant. Equation 3.14 was re-written by Du Plessis as [29]:

$$C^{\phi} = C_0^{\phi} + C^B \left[1 + \frac{2}{d} \left(\frac{D(t + t_0')}{\pi} \right)^{\frac{1}{2}} \right] - C^B \left[\frac{2}{d} \left(\frac{D t_0'}{\pi} \right)^{\frac{1}{2}} \right]. \tag{3.15}$$

Equation 3.15 is adapted to compensate for the segregation that occurs during sputtering [8, 29].

Note that equation 3.14 and 3.15 are applicable only for constant temperature experiments. For a linear heating experiment, the crystal is pre-heated at T_0 and the crystal temperature (T) is increased linearly with time at a constant heating rate (α). The relation is given by [30]

$$T = T_0 + \alpha t \tag{3.16}$$

By defining a surface enrichment factor $\beta = (C^{\phi} - C^B)/C^B$ equation 3.14 can be solved for linear heat as [5, 30]:

$$\beta^2 = \frac{4 D_0}{\pi \alpha d^2} \int_{T_0}^{T_E} e^{-Q/RT} dT. \tag{3.17}$$

It was shown that the integral part of equation 3.17 can be approximated by [5, 30]

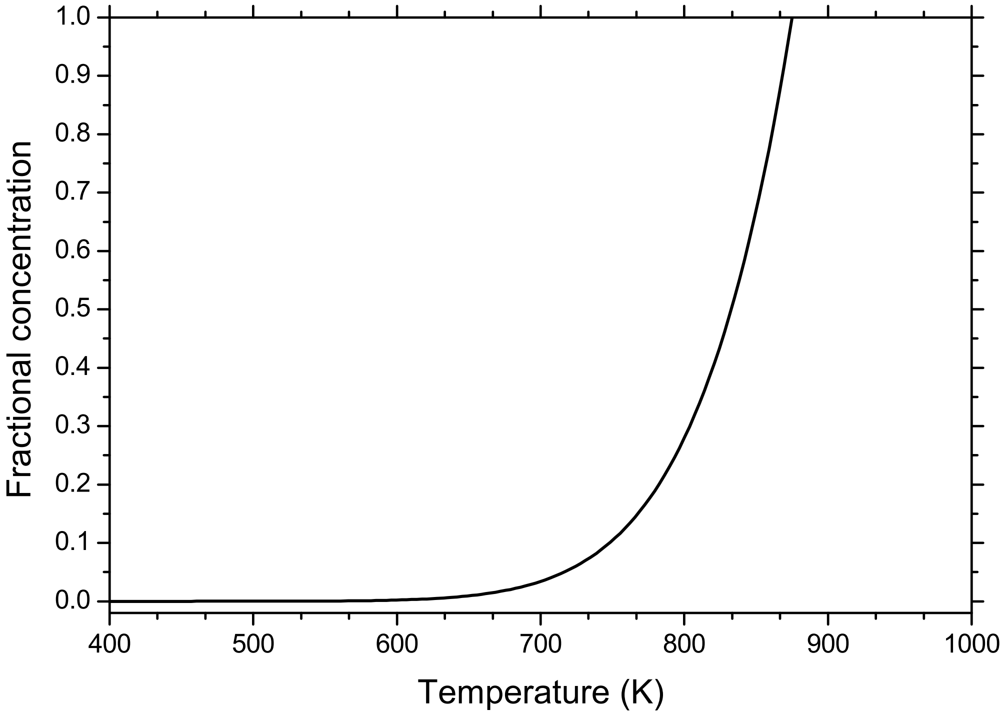

Figure 3.5: Fick's integral plot

.

$$\int_{T_0}^{T_E} e^{-Q/RT} dT \approx \left[\frac{RT^2}{Q} e^{Q/RT} \right]. \tag{3.18}$$

Thus,

$$\beta^2 = \frac{4D_0}{\pi \alpha d^2} \left[\frac{RT^2}{Q} e^{Q/RT} \right]. \tag{3.19}$$

A plot of equation 3.19 is shown in figure 3.5.

4

Thermodynamics of Surface Segregation

4.1 Introduction

Surface segregation is the enrichment at the surface or surface region of one component of an alloy as a result of diffusion of that element from the bulk to the surface region [31], which takes place only if the total energy of the crystal is lowered. The frequency with which dissolved atoms jump out of the surface layer is lower than the frequency of jumps into the surface layer [32], hence there is an accumulation of atoms at the surface. Therefore, segregation takes place.

In this chapter, the equilibrium conditions will be discussed for a crystal and crystal layers using thermodynamics theory of the equilibrium surface segregation. In addition, the theoretical segregation models will be discussed.

4.2 Equilibrium conditions for a crystal

Lupis [33] describes a crystal as a closed thermodynamic system divided into two phases, surface and bulk which are both open systems. Now, for a closed system of p phases the equilibrium condition in terms of energy is given by [28, 33]

$$(\delta E)_{S,V,n_i} = \sum_{\nu=1}^{p} \delta E^{\nu} \geq 0, \tag{4.1}$$

where E is the total energy, S is the entropy, V is the volume of the system and n_i is the total number of moles of component i. The entropy and volume of the total system remain unchanged.

From the definition of enthalpy H and Gibbs free energy G [33] it follows that

$$\delta E = T\delta S - P\delta V + \delta G, \tag{4.2}$$

for constant temperature and pressure. Now, using equation 4.1, equation 4.2 reduces to

$$(\delta E)_{n_i} = (\delta G)_{n_i} \geq 0, \tag{4.3}$$

for the equilibrium state of the crystal.

Therefore, it is sufficient to consider the variation of the Gibbs free energy during constant temperature and pressure. The advantage of this formulation is that the Gibbs free energy may be expanded in terms of the chemical potentials of the various constituents and that the equilibrium conditions may then be expressed as a function of the chemical potential [28].

4.3 The chemical potential

The Gibbs free energy of the crystal is a function of temperature T, pressure P and the total number of moles of the chemical component i, n_i, as discussed in the previous section:

$$G = G(T, P, n_i), \tag{4.4}$$

The exact differential of G may be written [34]

$$dG = \left(\frac{\partial G}{\partial T}\right)_{P,n_i} dT + \left(\frac{\partial G}{\partial P}\right)_{T,n_i} dP + \left(\frac{\partial G}{\partial n_i}\right)_{T,P,n_{j\neq i}} dn_i. \tag{4.5}$$

From the definition of Gibbs free energy and enthalpy given in the previous section:

$$dG = d(E - TS + PV) = dE - TdS - SdT + PdV + VdP. \tag{4.6}$$

Using equation 4.2, equation 4.6 can be written as

$$dG = VdP - SdT, \tag{4.7}$$

Therefore, equation 4.5 and equation 4.7 implies that

$$\left(\frac{\partial G}{\partial T}\right)_{P,n_i} = -S, \tag{4.8}$$

$$\left(\frac{\partial G}{\partial P}\right)_{T,n_i} = V \tag{4.9}$$

and the partial derivative of G with respect to n_i is the **chemical potential** of component i, μ_i [33, 34]

$$\mu_i = \left(\frac{\partial G}{\partial n_i}\right)_{T,P,n_{j\neq i}}. \tag{4.10}$$

In particular, μ_i may be viewed as the rate of change of the total Gibbs free energy of the system when, holding the temperature and the pressure constant, a very small amount of the component i is added to the system without changing the number of moles of the other components j [33]. Note that for a system consisting of a single component the chemical potential of this component is identical to its molar Gibbs free energy (that is, to the Gibbs free energy of one mole of that substance) [33]. If the chemical substance is free to move from one place to another, then it will move spontaneously to the state of lower chemical potential [35].

4.4 Equilibrium conditions for phases

Equation 4.7 can for an open system be expressed as [33, 34]

$$dG = VdP - SdT + \sum_i \mu_i dn_i. \tag{4.11}$$

If the temperature and pressure is the same for all the phases, equation 4.11 reduces to

$$G^\nu = \sum_{i=1}^{m} n_i^\nu \mu_i^\nu dn_i, \tag{4.12}$$

where G^ν is the Gibbs free energy for the phase ν consisting of m components, n_i^ν is the number of moles of the chemical component i in phase ν and μ_i^ν is the chemical potential of the chemical component i in phase ν.

4.4.1 Equilibrium conditions for two bulk phases

Considering a system of two phases (designated A and B) in the bulk where atoms of component i are exchanged between phase A and B. Therefore, the Gibbs free energy of the system is the sum of the Gibbs free energies of the two phases given by [28, 33]

$$G = G^A + G^B. \tag{4.13}$$

Substituting equation 4.12 into equation 4.13, the variation of G is

$$\delta G = \left(\sum_{i=1}^{m} \delta n_i^A \mu_i^A + \sum_{i=1}^{m} \delta n_i^B \mu_i^B \right) + \left(\sum_{i=1}^{m} n_i^A \delta \mu_i^A + \sum_{i=1}^{m} n_i^B \delta \mu_i^B \right). \tag{4.14}$$

The second bracket on the right-hand side of equation 4.14 is Gibbs-Duhem equation and is equal to zero (at constant temperature and pressure)[33, 34]. For a closed system, the total number of atoms is conserved (i.e. $\delta n_i^A = -\delta n_i^B$). As a result, using equation 4.3, equation 4.14 reduces to

$$\delta G = \sum_{i=1}^{m} (\mu_i^A - \mu_i^B) \delta n_i^A \geq 0. \tag{4.15}$$

At the equilibrium, the variation of G is zero and that is satisfied by equation 4.15 only if δn_i^A's are independent and

$$(\mu_i^A - \mu_i^B) = 0. \tag{4.16}$$

Therefore, the equilibrium condition for two bulk phases in contact is expressed in terms of the chemical potential as

$$\mu_i^A = \mu_i^B \quad \text{for } i = 1, 2, ..., m. \tag{4.17}$$

This relation implies that, at equilibrium the chemical potential must be constant throughout the bulk of the system for each substance that is free to move.

4.4.2 Equilibrium conditions for surface and bulk phases

In a substitutional alloy, the number of moles in the surface ϕ layer is fixed and that can be written as [28]

$$\sum_{i=1}^{m} n_i^{\phi} = n^{\phi}. \tag{4.18}$$

Thus, for conservation of atoms in the surface layer equation 4.18 is expressed as

$$\delta n_1^{\phi} + \delta n_2^{\phi} + \cdots + \delta n_m^{\phi} = 0 \tag{4.19}$$

where the m-th term is further written in terms of the previous $m-1$ terms:

$$-\delta n_m^{\phi} = \delta n_1^{\phi} + \delta n_2^{\phi} + \cdots + \delta n_{m-1}^{\phi}. \tag{4.20}$$

Therefore, equation 4.15 for surface and bulk reduces to

$$\delta G = \left[\sum_{i=1}^{m-1} (\mu_i^{\phi} - \mu_i^{B})\delta n_i^{\phi}\right] + (\mu_m^{\phi} - \mu_m^{B})\delta n_m^{\phi} = \sum_{i=1}^{m-1} (\mu_i^{\phi} - \mu_i^{B} - \mu_m^{\phi} + \mu_m^{B})\delta n_i^{\phi} \geq 0. \tag{4.21}$$

Equation 4.21 satisfy the equilibrium conditions only if

$$(\mu_i^{\phi} - \mu_i^{B} - \mu_m^{\phi} + \mu_m^{B}) = 0. \tag{4.22}$$

Thus, equation 4.22 represents the equilibrium condition for atoms segregating from the bulk B into the surface ϕ of a crystal.

4.5 The modified Darken model

Fick's model take the concentration gradient as the driving force behind diffusion, but the Darken model take the chemical potential gradient as the driving force behind diffusion of atoms from a region of high chemical potential (bulk) to a region of low chemical potential (surface) and in the process minimizes the total energy of the crystal.

In the Darken model, the flux J_i of species i through a plane at $x = b$ is given by [28, 36]

$$J_i = -M_i C_i^{(b)} \left(\frac{\partial \mu_i}{\partial x} \right)_{x=b} \tag{4.23}$$

where M_i is the mobility of species i in the bulk, $C_i^{(b)}$ is the concentration of species i in the plane and μ_i is the chemical potential of species i.

Du Plessis [28] in his modification of the Darken model defines a crystal as a closed system divided into $N+1$ open subsystems (discrete atomic layers parallel to the surface layer) of thickness d and wrote the term in parentheses of equation 4.23 as

$$-\frac{\partial \mu_i}{\partial x} = \frac{\Delta \mu_i^{(j+1) \to j}}{d} \tag{4.24}$$

where $\Delta \mu_i^{(j+1 \to j)} = (\mu_i^{(j+1)} - \mu_i^{(j)}) - (\mu_m^{(j+1)} - \mu_m^{(j)})$.

Du Plessis wrote term $C_i^{(b)}$ in equation 4.23 as the supplier of atoms ($C_i^{(j+1)}$) (the concentration of species i in the $j+1$-th layer) from a layer $j+1$ into a layer j.

Therefore, equation 4.23 can be written as

$$J_i^{(j+1\to j)} = M_i^{(j+1\to j)} C_i^{(j+1)} \left(\frac{\Delta\mu_i^{((j+1)\to j)}}{d} \right) \tag{4.25}$$

for the flux of atoms diffusing from layer $j+1$ to layer j, and for the flux of atoms in opposite direction (from layer j to layer $j+1$) as

$$J_i^{(j\to j+1)} = M_i^{(j\to j+1)} C_i^{(j)} \left(\frac{\Delta\mu_i^{((j+1)\to j)}}{d} \right) \tag{4.26}$$

Equation 4.25 and 4.26 describe the flux between two adjacent layers j and $j+1$ in the crystal, but only one is relevant at a definite time. For instance, if $\Delta\mu_i^{(j+1\to j)} > 0$, the Gibbs free energy will decrease when atoms move from layer $j+1$ to j, and equation 4.25 will be appropriate for calculations and if $\Delta\mu_i^{(j+1\to j)} < 0$, the free energy will decrease when atoms move from layer j to $j+1$, making equation 4.26 appropriate for calculations.

Following from equation 4.25 and 4.26, the rate at which the concentration $C_i^{(j)}$ in layer j is changing with time (t) can be calculated as [28]

$$\begin{aligned} \frac{\partial C_i^{(j)}}{\partial t} &= \frac{J_i^{(j+1\to j)} - J_i^{(j\to j-1)}}{d} \\ &= \left[\frac{M_i^{(j+1\to j)} C_i^{(j+1)}}{d^2} \Delta\mu_i^{(j+1\to j)} - \frac{M_i^{(j\to j-1)} C_i^{j}}{d^2} \Delta\mu_i^{(j\to j-1)} \right]. \end{aligned} \tag{4.27}$$

The concentration is now written in terms of the fractional concentration as:

$$\partial C_i^{(j)} = X_i^{(j)} \frac{1}{d^3} \tag{4.28}$$

Similarly, the concentration change of species i in discrete layers as a function of time is given as [28]

$$\begin{aligned}
\frac{\partial X_i^{\phi}}{\partial t} &= \left[\frac{M_i^{(B_1\to\phi)}X_i^{B_1}}{d^2}\Delta\mu_i^{(B_1\to\phi)}\right];\\
\frac{\partial X_i^{B_1}}{\partial t} &= \left[\frac{M_i^{(B_2\to B_1)}X_i^{B_2}}{d^2}\Delta\mu_i^{(B_2\to B_1)} - \frac{M_i^{(B_1\to\phi)}X_i^{B_1}}{d^2}\Delta\mu_i^{(B_1\to\phi)}\right];\\
&\vdots\\
\frac{\partial X_i^{j}}{\partial t} &= \left[\frac{M_i^{(j+1\to j)}X_i^{(j+1)}}{d^2}\Delta\mu_i^{(j+1\to j)} - \frac{M_i^{(j\to j-1)}X_i^{j}}{d^2}\Delta\mu_i^{(j\to j-1)}\right] \qquad (4.29)
\end{aligned}$$

where B_1 and B_2 are the first (subsurface layer) and second bulk layers respectively.

The mobility is related to the diffusion coefficient via

$$M_i = \frac{D_i}{RT}. \qquad (4.30)$$

The set of differential equations 4.29 describe the rate at which the concentration of species i changes with time in terms of the chemical potential and the mobility of the segregating species and can be solved numerically. Equation 4.29 is normally used to yield all segregation parameters in metal alloys.

4.6 Guttmann model

During segregation, the concentration change between the bulk layer (subsurface layer) and the surface layer takes place until equilibrium is reached. For a ternary system ($i = 1, 2$ and $m = 3$), the equation 4.22 can be given by

$$\mu_1^\phi - \mu_1^B - \mu_3^\phi - \mu_3^B = 0$$
$$\mu_2^\phi - \mu_2^B - \mu_3^\phi - \mu_3^B = 0 \tag{4.31}$$

Using the regular solution model [28, 33], equation 4.31 can be expanded to give the following equilibrium segregation equations known as Guttmann equations [28]:

$$X_1^\phi = \frac{X_1^B \exp(\Delta G_1/RT)}{1 - X_1^B + X_1^B \exp(\Delta G_1/RT) - X_2^B + X_2^B \exp(\Delta G_2/RT)} \tag{4.32}$$

$$X_2^\phi = \frac{X_2^B \exp(\Delta G_2/RT)}{1 - X_2^B + X_2^B \exp(\Delta G_2/RT) - X_1^B + X_1^B \exp(\Delta G_1/RT)} \tag{4.33}$$

where

$$\Delta G_1 = \Delta G_1^0 + 2\Omega_{13}(X_1^B - X_1^\phi) + \Omega'(X_2^\phi - X_2^B) \tag{4.34}$$

$$\Delta G_2 = \Delta G_2^0 + 2\Omega_{23}(X_2^B - X_2^\phi) + \Omega'(X_1^\phi - X_1^B) \tag{4.35}$$

and

$$\Omega' = \Omega_{12} - \Omega_{13} - \Omega_{23} \tag{4.36}$$

with ΔG_i the segregation energy of species i and Ω_{ij} is the interaction energy between species i and j.

At equilibrium the surface concentration of the specie with the highest segregation energy (more negative) has the highest equilibrium concentration on the surface.

In the regular solution [33], if specie 1 (segregating) and specie 3 (crystal) atoms differ in size, the interaction parameter between specie 1 and 3 is not zero ($\Omega_{13} \neq 0$). The $\Omega_{13} > 0$ is usually interpreted as attraction between the atoms of specie 1 and specie 3 (set preference for unlike first-neighbor bonds) and lead to a higher enrichment of specie 1 in a dilute alloy. The attractive interaction indicates the tendency of compound formation. The $\Omega_{13} < 0$ is interpreted as repulsion between the atoms of specie 1 and specie 3 (preference for like first-neighbor bonds) and a weak enrichment of specie 1 in the surface is accompanied by an increased amount of the specie 3 in the surface sublayer.

In the case of interaction between the two segregating species Ω_{12}, attractive interaction $\Omega_{12} > 0$ lead to a lower equilibrium concentration of specie 2 and a higher equilibrium concentration of specie 1 [37]. A repulsive interaction $\Omega_{12} < 0$ lead to a higher equilibrium concentration of specie 2 and a lower equilibrium concentration of specie 1 [37].

Part II

EXPERIMENT AND PROCEDURE

5

Experimental Details

5.1 Introduction

In the first chapter of this study, it was mentioned that a Cu crystals will be doped with In, firstly by depositing an In layer onto the backside of a Cu crystal and then secondly coating the In layer with a Cu layer. Then anneal the crystal at a low temperature to form intermetallic phases (Cu_xIn_y) with higher melting points and then increase the annealing temperature stepwise without melting the In layer and the Cu_xIn_y phases until the final annealing temperature (900 ℃). This chapter firstly focused on the preparation and the analysis method of In/Cu thin films that were deposited on a SiO_2 substrate and secondly on the In diffusion doping of Cu crystal. A brief discussion on the operation of techniques used during these experiments is also included.

5.2 In/Cu thin films preparation and analysis

In/Cu thin films were prepared on passivated Si. SiO_2 substrates were prepared by wet oxidation of Si (100) at 1000 ℃ for 1 hour. The SiO_2 is a diffusion barrier and prevents the In and Cu from diffusing into Si.

Figure 5.1: A photo of the evaporation system.

The SiO_2 substrates ($1cm^2$ in size) were cooled to room temperature and loaded inside the electron beam evaporation system (shown in figure 5.1). An In films of 500 Å were deposited on the substrate (SiO_2) at a deposition rate of 3 Å/s. The In films were then coated with Cu films that range in thickness from 500 Å to 1000 Å. The Cu films were also grown in the same evaporation system without breaking the vacuum. The deposition rate of the Cu was 12 Å/s. The emission current during deposition of In was 40 mA and for Cu it was 55 mA and the voltage was 4 kV. During the film growth the base pressure in the vacuum chamber was 2.5×10^{-5} Torr and was attained with rotary vane and turbo molecular pump. The films thicknesses were monitored during the evaporation with an Inficon Leybold Heraeus XTC thin film monitor.

The In films coated with a 500 Å and 1000 Å Cu layer were annealed in a vacuum tube furnace with a base pressure of 8.0×10^{-5} Torr. The annealing temperatures

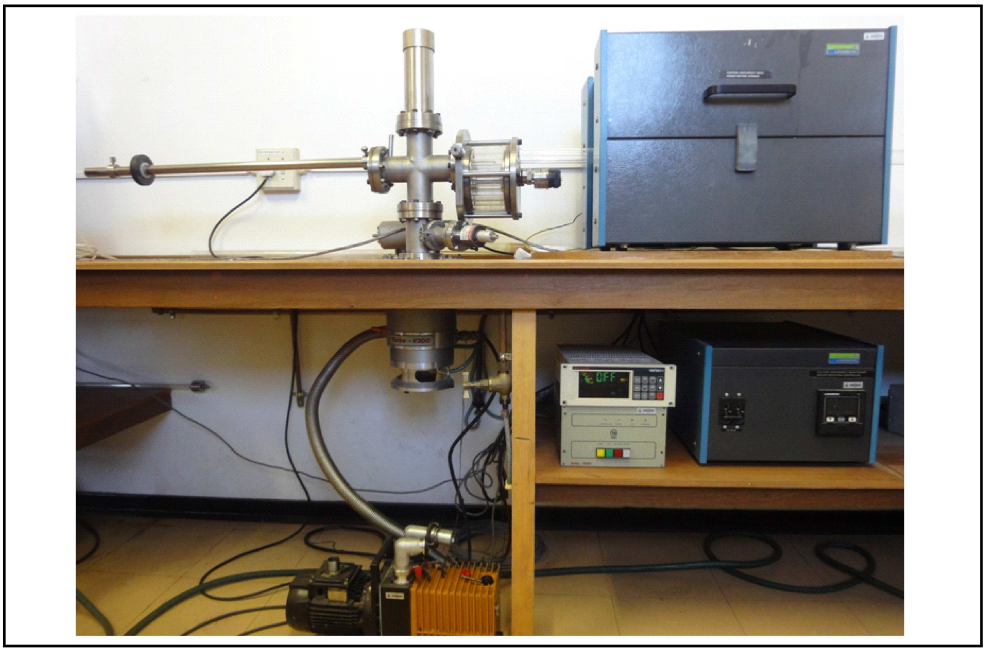

Figure 5.2: A photo of the vacuum annealing system.

were, 150 ℃, 200 ℃, 250 ℃ and 300 ℃ for 49 minutes. The vacuum tube furnace (Figure 5.2) is connected to a carousel holder that allow multiple samples to be loaded into the system and annealed one by one without breaking vacuum.

5.2.1 XRD measurements

The Bruker AXS D8 ADVANCE X-ray diffractometer (Figure 5.3) with a Cu anode and monochromatic Ni-filter produce X-rays with a wavelength of λ= 1.5406 Å. During the XRD measurements the system was operated at a voltage of 40 kV and a current of 40 mA. The diffraction angle (2θ) was scanned from 30° to 60° with an increment step of 0.01° and the x-ray photons counted for 1 second at each step. The XRD measurements were used to characterize (indentifying the compounds that formed) the samples after evaporation and annealing.

Figure 5.3: A photo of the XRD system.

5.2.2 AES depth profiles measurements

In AES the target is irradiated with a high energy primary electron beam. On the target, the incident electron beam of high-energy electrons causes Auger transitions within the target and the subsequent emission of Auger electrons. The kinetic energies of the Auger electrons are analyzed with the cylindrical mirror analyzer (CMA). The voltages on the plates of the CMA can be adjusted so that only electrons with certain energy can pass through the CMA and get counted. The Auger electrons are analyzed as a function of energy (the peak positions and shapes) and are used to identify the elements and the chemical states present on the target surface. There is also emission of secondary and backscattered electrons from the target surface. The secondary electrons are collected with a secondary electron detector (SED). These secondary electrons contain information about the topography of the sample surface and can be used to generate an

Figure 5.4: A photo of the PHI 600 SAM.

image of the sample surface. The backscattered electrons are used to position the target at the focal point of the CMA.

The electron gun of the Auger system uses a lanthanum hexaboride (LaB_6) crystal as filament. LaB_6 has lower work function, greater emissivity, long life and stability. This filament (cathode) generates a beam of electrons that can be focused to a very small spot (< 1 μm). During operation, a current of 1.4 A is passed through the filament to heat the filament.

The Auger depth profiles measurements in this study were performed on a PHI 600 Scanning Auger Microscopy (SAM) (Figure 5.4). Before any measurements were made the system was turned on and allowed to stabilize for two hours.

AES depth profiles of the In/Cu thin films were obtained utilizing Ar^+ ion etching with a 2.0 keV ion beam with an ion current density of 0.113 A/m^2 at a raster area of 2 mm × 2 mm. The AES measurements were performed with a 10.0 keV electron beam with a beam current of 4.8 μA. During spectrum acquisition the base pressure in the main chamber was 9.0×10^{-8} Torr and the ion gun was operated at an argon pressure of 3.4×10^{-5} Torr in the ionization chamber. The sample was tilted with the normal of the film surface at a 30° with respect to the direction of the incident electron beam. Auger peak to peak heights (APPHs) were recorded as a function of the sputtering time for In (301-440 eV)[1], Cu (870-950 eV), O (450-530 eV), Si (60-105 eV) and C (230-300 eV). All the depth profiles were measured at room temperature.

Electron beam size and ion beam current density

A Faraday cup (with a hole of 300 μm) was used to measure the beam current of the electron and ion beam. A 10.0 keV electron beam with a beam current of 4.8 μA (that was used for thin films analysis) was scanned across the edge of the Faraday cup and the SED signal was recorded and plotted in figure 5.5(a). The derivative of the SED signal with respect to distance was obtained (Figure 5.5(b)). In figure 5.5(b), the diameter of the electron beam was obtained as 1.2 μm in x-direction and 1.3 μm in y-direction from the full width at half maximum (FWHM). The shape of the beam used was nearly round as preferred in AES analysis.

In depth profiling, the ion beam current density is one of the important parameters. If a Faraday cup is used to measure the ion current density then a cross-sectional area A at $\theta > 0$ of the entrance hole of a Faraday cup is given by

$$A = A_0 \cos\theta, \tag{5.1}$$

---

[1] Energy range monitored during measurements

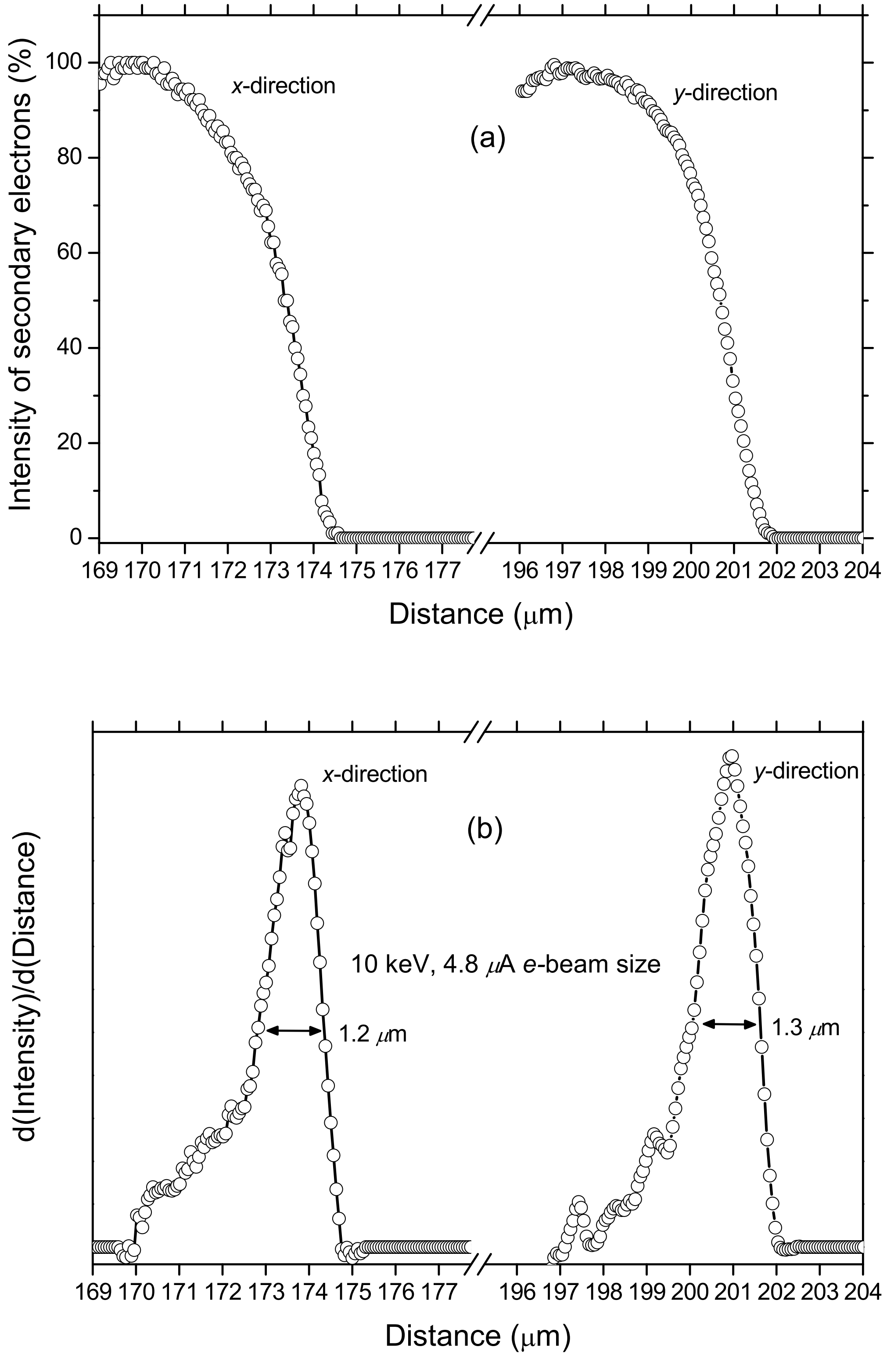

Figure 5.5: (a) The intensity of secondary electrons as function of scan distance across the edge of the Faraday cup and (b) the diameter of 10.0 keV primary electron beam.

where A_0 is a cross-sectional area of the entrance hole of a Faraday cup at $\theta = 0$, θ is the angle between the ion beam and the sample surface ($\theta = 50°$).

Using a Faraday cup and equation 5.1 the ion current density was obtained for different ion beam energies and are listed in table 5.1. The results tabulated in table 5.1 were plotted in figure 5.6. During thin films depth profiling, an ion beam with low current density (2.0 keV) was preferred for its good depth resolution.

Table 5.1: Ion current density measured as function of Ar^+ ion beam energy.

Ar^+ ion beam energy E (keV)	Ion current density ($\mu A/cm^2$)
0.5	3.7
1.0	7.6
2.0	14.8
3.0	31.4
4.0	51.5

AES quantification (Thin films)

Quantitative analysis in AES, gives the average concentrations of a range of elements within the area under analysis. This analysis relates the measured APPH to the actual elemental composition of the sample. The first approach that is usually adopted is to assume that the composition of the sample in the near surface region is homogeneous then a good approximation for the atomic concentration (C_A) of an element A in a sample is given by [38]

$$C_A = \frac{(\mathrm{APPH})_A/(\mathrm{APPH})_A^\infty}{\sum_i (\mathrm{APPH})_i/(\mathrm{APPH})_i^\infty}, \tag{5.2}$$

where $(\mathrm{APPH})_i^\infty$ is the Auger signal from a pure elemental standard measured

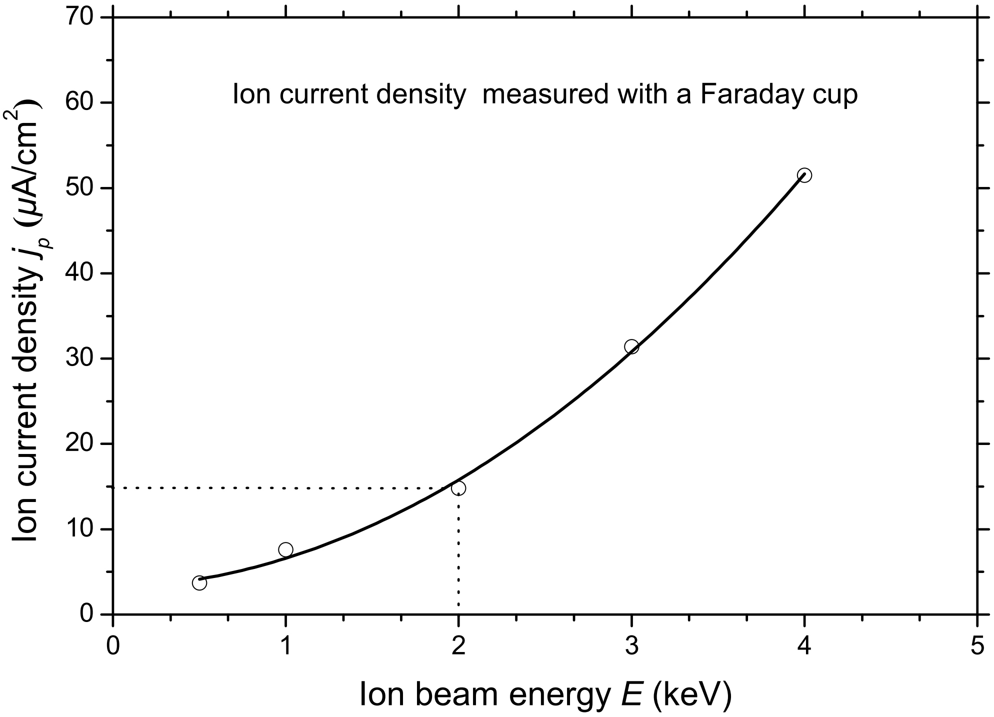

Figure 5.6: Ion current density as function of Ar^+ ion beam energy at an argon pressure of 3.4×10^{-5} Torr and emission current of 25mA.

under identical conditions, also known as sensitivity factor.

Although, equation 5.2 gives good estimates of composition it ignores matrix effects.

Figure 5.7(a) shows the APPH *vs.* sputter time graph (depth profile) obtained from the In/Cu thin films deposited onto SiO_2. The APPH axis was converted to a concentration scale using equation 5.2 (see figure 5.7(b)). The sensitivity factors used were measured from pure elemental standards under the same conditions used for the depth profiles. The sputter time needs to be converted to a depth scale. With the assumption that the primary ion current density is constant under the area of analysis, the average sputtering rate is given by [26]

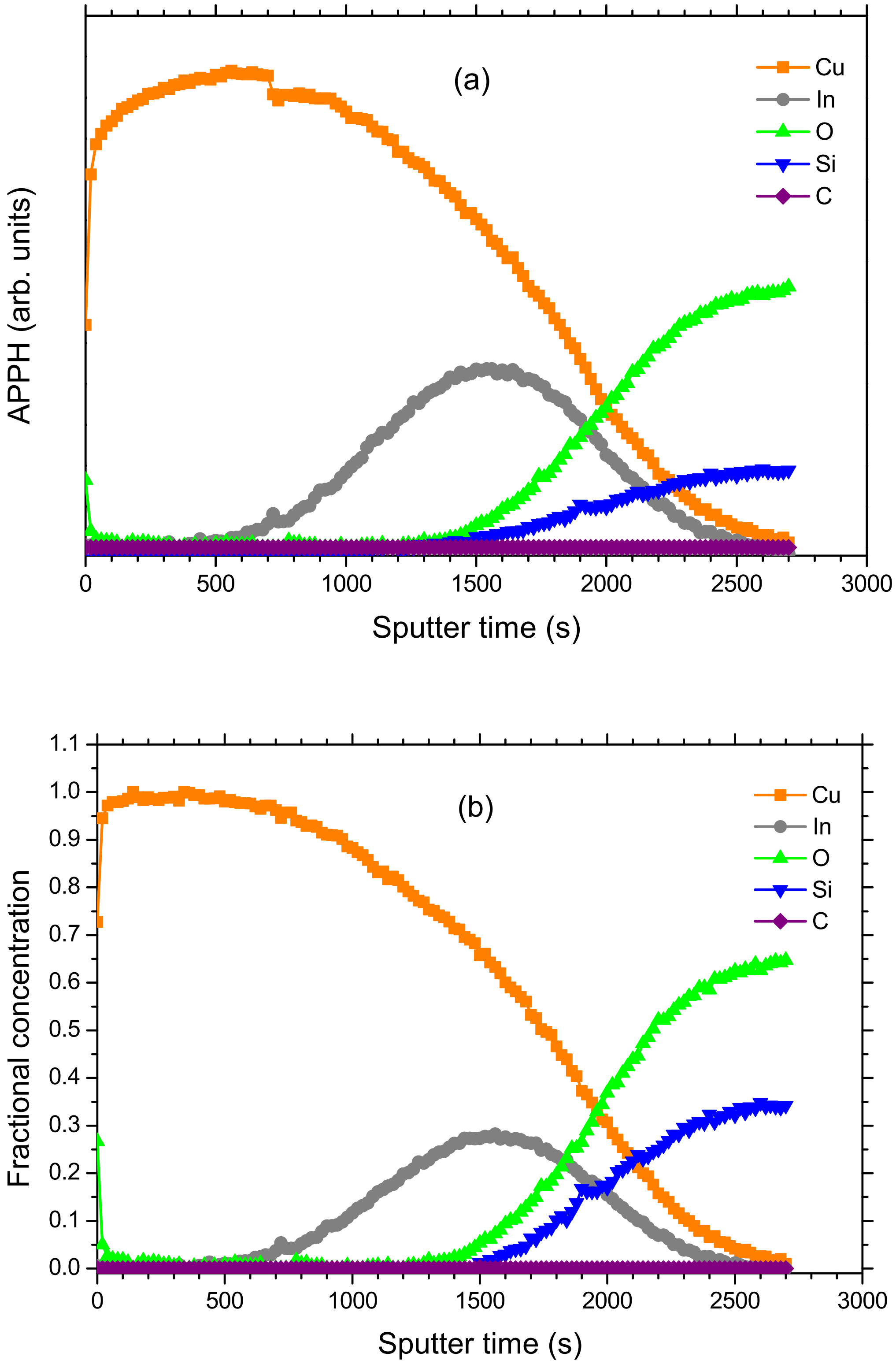

Figure 5.7: (a) APPH *vs.* sputter time and (b) fractional concentration *vs.* sputter time depth profiles of the In/Cu thin films deposited onto SiO_2 substrate.

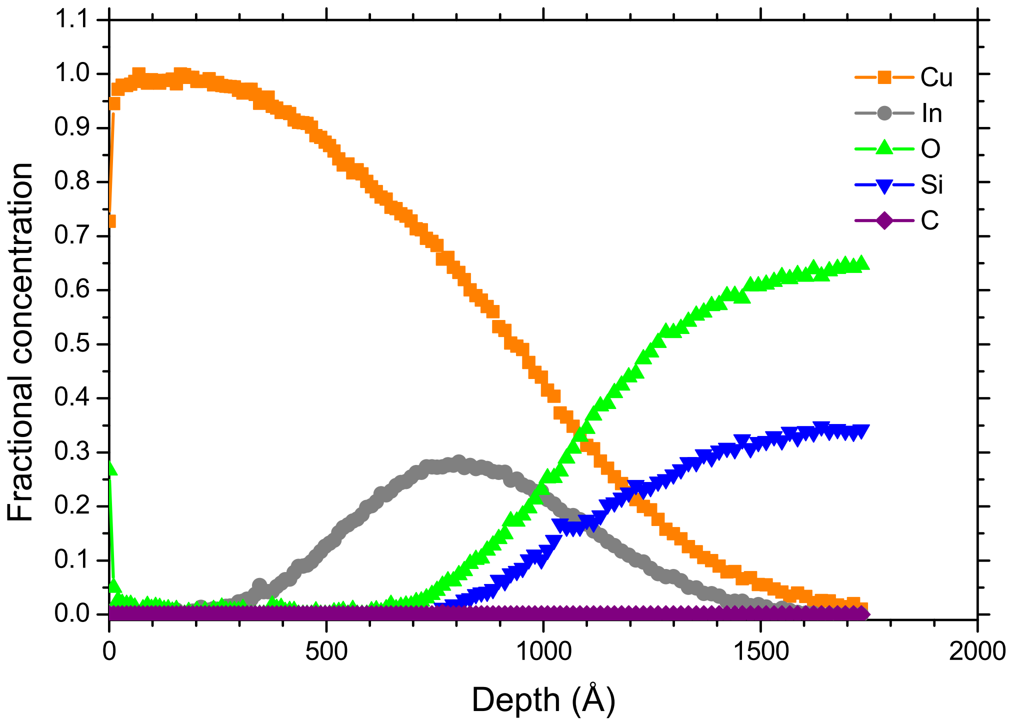

Figure 5.8: A fully quantified In/Cu thin fimls depth profile.

$$\dot{z}(t) = \sum_{i=1}^{n} C_i(t)\dot{z}_i, \tag{5.3}$$

where C_i is fractional concentration of element i at sputter time t and $\dot{z}_i$ is the sputter rate for the pure element i.

The sputter rates were obtained for elements (In; Cu; SiO_2 and C) comprising the sample (Figure 5.7(b)). Therefore, using equation 5.3 the depth profile shown in figure 5.7(b) was converted to a fully quantified depth profile shown in figure 5.8. All the depth profiles discussed in section 6.2 were quantified using this method.

5.3 Cu(In) alloy preparation and analysis

Polycrystalline Cu crystals (0.70 mm thick and 10 mm diameter) were obtained from a high purity (99.99 %) polycrystalline Cu. One side of the crystals was chosen as the front side and was mechanically polished to 0.05 μm using a diamond suspension solution. The masses of the crystals were measured using a calibrated Mettler M3 mass balance and tabulated in table 5.2.

Table 5.2: The masses of the Cu crystals, samples after first deposition (third column), after second deposition (fourth column), deposited Cu and In layers.

Samples	Crystal mass (±0.015 mg)	Sample mass (±0.015 mg)	Sample mass (±0.015 mg)	Cu layer mass (mg)	In layer mass (mg)
A1	433.772	435.210	435.461	0.251	1.187
A2	421.494	423.048	423.309	0.261	1.293
A3	449.205	450.690	450.944	0.254	1.231

On the back side of the crystals, an In layer with thickness of 15580 Å was deposited by means of electron beam deposition. The In layer was then coated with Cu layer with thickness of 3520 Å (for the first deposition process). In the second deposition process, another layer of Cu with exactly the same thickness (3520 Å) was deposited on top of the previous Cu layer. After the first and second deposition process, the samples masses were obtained and are listed in table 5.2.

The thickness of the In layer d_{In} required for approximately 0.1 at% bulk concentration was determined using the expression

$$d_{\mathrm{In}} = \frac{m_{\mathrm{In}} \rho_{\mathrm{Cu}}}{m_{\mathrm{Cu}} \rho_{\mathrm{In}}} d_{\mathrm{Cu}} \tag{5.4}$$

where d_{Cu} is the crystal thickness, ρ_{Cu} is the Cu density, ρ_{In} is the In density, m_{Cu} is the mass of the Cu crystal (see table 5.2) and m_{In} is the mass of the In layer (0.784 mg) to be deposited.

The mass of the In layer in equation 5.4 is given by

$$m_{\mathrm{In}} = \frac{M_{\mathrm{In}} X_{\mathrm{In}}^{B}}{M_{\mathrm{Cu}}(1 - X_{\mathrm{In}}^{B})} m_{\mathrm{Cu}} \tag{5.5}$$

where X_{In}^{B} is the In bulk concentration to be added into the crystal, M_{In} and M_{Cu} is the molar mass of the In and Cu respectively.

Furthermore, samples (A1-A3) were placed in a ceramic boat that was placed inside a quartz tube at the centre of the oven for annealing (Figure 5.9). The tube was first pumped down to 10^{-5} Torr and then filled with Ar gas to a pressure of 500 Torr at a slow flow rate of 3 l.min^{-1} and left at this pressure for 10 min. After 10 min, the tube was again pumped down to 10^{-5} Torr for 10 min and then filled with Ar gas to a pressure of 500 Torr and this procedure was repeated five times. Finally, the tube was filled with Ar gas to a pressure of 500 Torr for annealing. The annealing temperature was set as shown in table 5.3. Immediately after annealing cycle at 300 ℃ for 48 hours, the annealing furnace was cooled to room temperature. Once again, the tube was pumped down to 10^{-5} Torr for 10 min and then filled with Ar gas to a pressure of 500 Torr and this procedure was repeated five times to pump out any possible gases from the samples. Once again, the tube was filled with Ar gas to a pressure of 500 Torr for annealing. The temperature was slowly increased to 380 ℃ and the annealing was completed for all the temperatures and times shown in table 5.3.

Figure 5.9: A photo of the annealing system.

Table 5.3: The Cu-In secondary phases and the corresponding melting or transition temperatures obtained from Ref. [16], the annealing temperature and time.

Materials and secondary phases	Melting/Transition temperature (℃)	Annealing temperature (℃)	Annealing time (hours)
In	155.5	-	-
$CuIn_2$	<150	150	48
$Cu_{11}In_9$	305.8	300	48
η-Cu_2In	388.3	380	48
δ-Cu_7In_3	632.2	625	48
η'-Cu_2In	670.2	650	48
γ-Cu_7In_3	684.1	670	48
β-Cu_4In	711.3 and 679	700	48
α-Cu	>800	750	48
Cu	1084.87	900	456

The 456 hours annealing time was calculated using equation 3.11 and gives a uniformity of 99.99 % in the crystal (see figure 5.10).

After annealing, the masses of the samples were obtained and are tabulated in

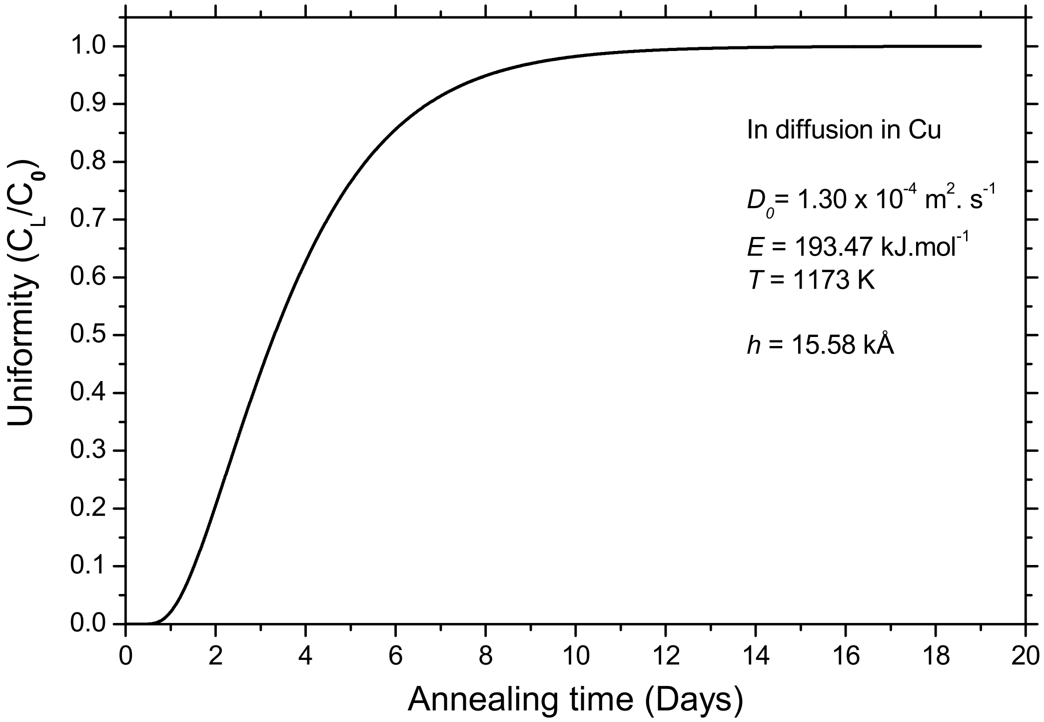

Figure 5.10: Uniformity in the crystal as function of annealing time where $L = 0.70$ mm, D_0 and Q values are obtained from Ref. [10].

table 5.4. From the masses of the Cu and In layers shown in table 5.2, it follows that 30 % of the mass gained by crystals (Table 5.4) is from Cu thin layers and 70 % is from In thin layers. Therefore, the mass of the Cu and In thin layers were obtained and listed in table 5.4. As result, the In bulk concentration X^B_{In} was obtained and listed in table 5.4.

Table 5.4: The masses of the Cu crystals, samples after annealing, Cu and In thin layers and the In bulk concentration.

Samples	Crystal mass (±0.015 mg)	Sample mass (±0.015 mg)	Added mass (mg)	Cu added mass (mg)	In added mass (mg)	X^B_{In} (at%)
A1	433.772	434.431	0.659	0.196	0.463	0.059
A2	421.494	422.22	0.726	0.209	0.517	0.068
A3	449.205	449.947	0.742	0.217	0.525	0.065

Figure 5.11: A photo of the PHI 590 SAM.

5.3.1 AES segregation measurements

The AES segregation measurements were performed on a PHI 590 scanning Auger system shown in figure 5.11. Figure 5.12 shows a schematic diagram of the experimetal setup used for segregation measurements. A 5.0 keV electron beam (that was used for segregation measurements) was scanned across the edge of the Faraday cup (with a hole of 600 μm) and the SED signal was obtained and plotted in figure 5.13(a). The derivative of the SED signal with respect to distance was obtained and plotted in figure 5.13(b). In figure 5.13(b), the diameter of a 5.0 keV primary electron beam was obtained as 13.3 μm.

A crystal (sample A1) was mounted on a heater inside the ultra high vacuum (UHV) chamber (P = 1.0×10^{-9} Torr). The junction of the chromel-alumel thermocouple (Type K), was placed on the ceramic and the back of the crystal was pressed onto the junction with a stainless steel screw cap (see the heater

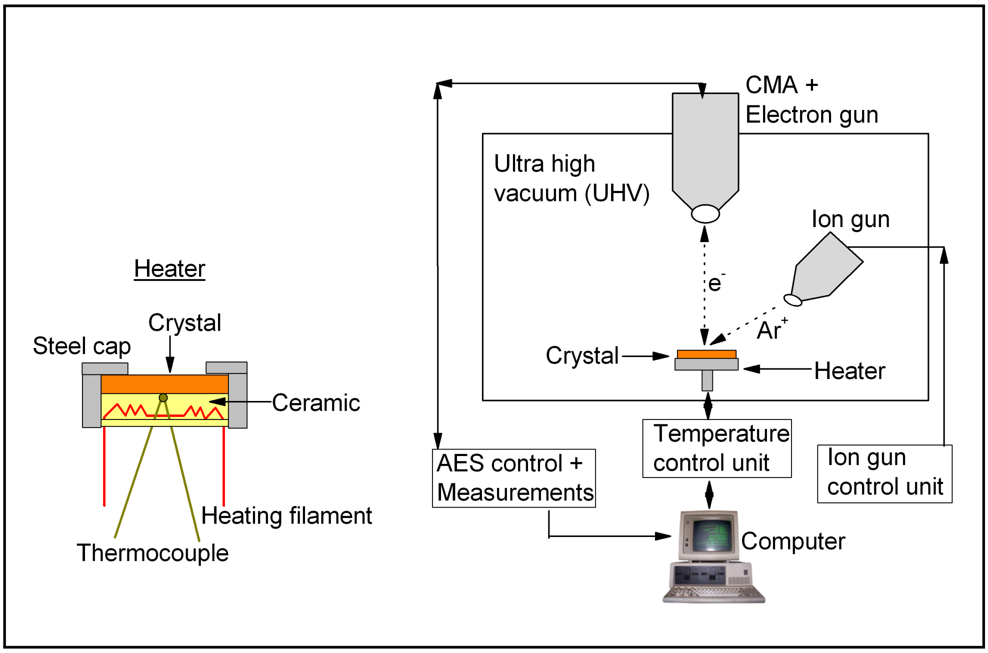

Figure 5.12: A schematic diagram of the experimental setup used for segregation measurements.

schematic diagram in figure 5.12). The temperature was measured from the back of the crystal. The heating filament was embedded in the ceramic. A heater is connected to a control unit that is connected to a computer (Figure 5.12). The temperature of a crystal was controlled with a computer.

A 5.0 keV primary electron beam with a current of 0.7 μA, modulation energy of 2 eV, the scan rate of 5 eV.s^{-1} and a time constant of 0.1 s was used for the AES measurements. The AES measurements were controlled with *Visi-scan* computer software (Figure 5.12).

An ion gun was used for sputter cleaning. It was operated at the beam energy of 2.0 keV, pressure of P = 1.5 × 10^{-5} Torr and the beam was rastered over a 2 mm × 2 mm area. The crystal was tilted with the normal of the crystal surface at a 30° with respect to the direction of the incident electron beam.

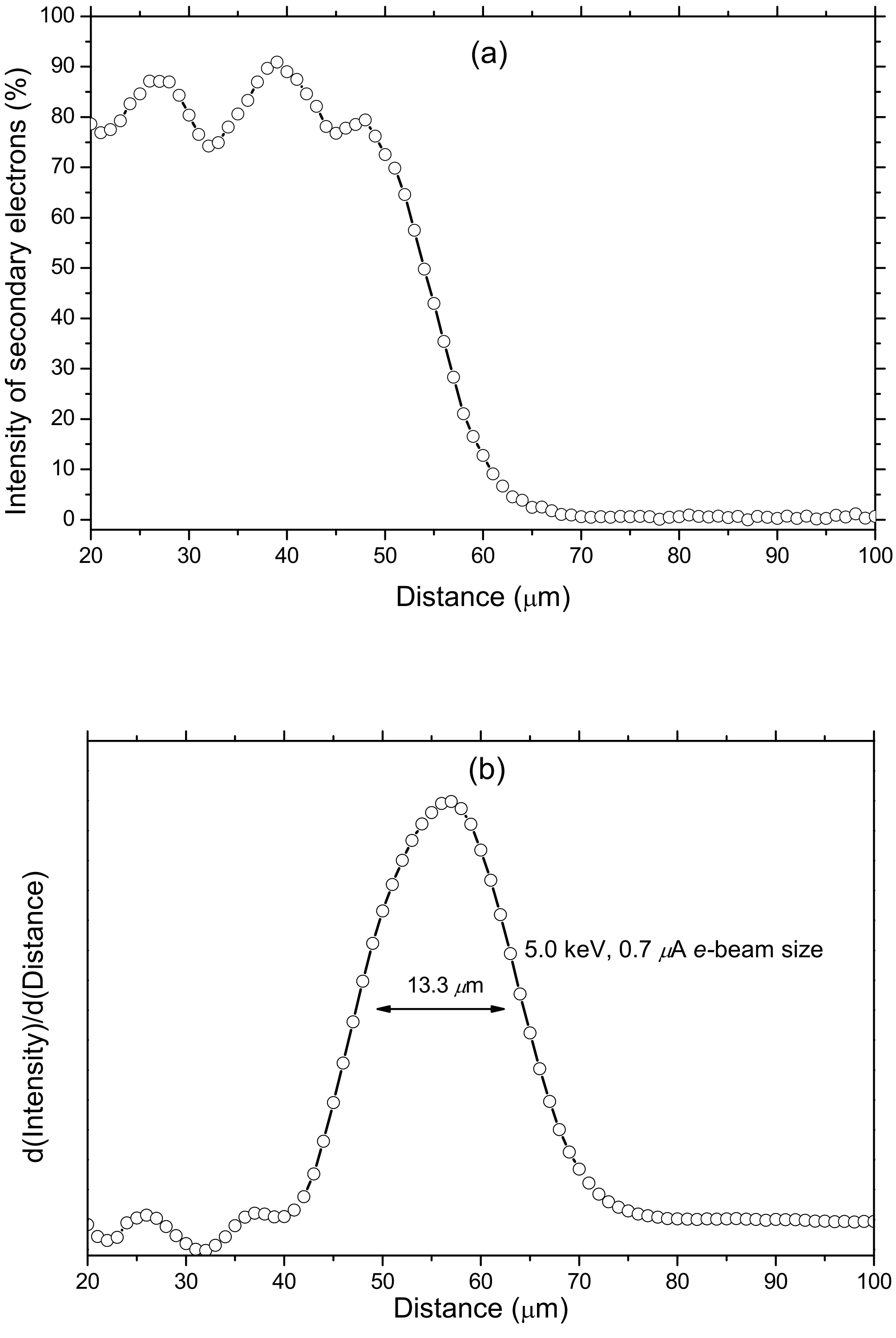

Figure 5.13: (a) The intensity of secondary electrons as function of scan distance across the edge of the Faraday cup and (b) the diameter of 5.0 keV primary electron beam.

AES linear temperatures measurements were carried out from 373 K to 1073 K at heating rates of 0.025; 0.05; 0.1 and 0.2 $K.s^{-1}$ for each run. Before each run, the crystal was pre-heated at 1073 K for 24 hours and cooled to 373 K at rate of -0.05 $K.s^{-1}$ (to restore the initial condition of the crystal). The crystal was also pre-heated at 373 K for 1 hour and sputter cleaned for exactly 30 s. Immediately after sputtering, the APPHs were recorded as a function of time for Cu (922 eV), S (153 eV) and In (405 eV).

AES Constant temperature measurements were performed for temperatures 733 K; 763 K; 793 K; 823 K and 853 K. At each temperature, the crystal was pre-heated for 1 hour and sputter cleaned for 30 s. After sputtering APPHs were recorded as a function of time for Cu (922 eV), S (153 eV) and In (405 eV). Once again, before each temperature run the crystal was pre-heated at 1073 K for 24 hours and cooled to 373 K at a rate of -0.05 $K.s^{-1}$.

5.3.2 AES quantification (a monolayer segregation)

For monolayer segregation the following assumption is made:

i. The segregation is restricted to the surface monolayer only and the concentration of impurities beneath this layer is equal to the bulk concentration.

The Auger intensity of element A is given by [26, 28, 29]

$$I_A = I_p \sigma_A(E_p)[1 + r^M(E_A, \alpha)]T(E_A)D(E_A) \times \int_0^\infty n_A^M(z) e^{(-z/\lambda_M(E_A) cos\theta)} dz \quad (5.6)$$

where

I_p is the primary electron current,

$\sigma_A(E_p)$ is the ionization cross section of atom A by electrons with energy E_p,

$r^M(E_A, \alpha)$ is the backscattering term dependent on both the matrix M and the binding energy for the core level electron involved in the transition leading to an Auger electron with energy E_A,

$T(E_A)$ is the transmission efficiency of the spectrometer,

$D(E_A)$ is the efficiency of the electron detector,

$n_A^M(z)$ is the atomic density (in atoms/m^3) of element A at a depth z from the surface,

$\lambda_M(E_A)$ is the inelastic mean free path in the matrix M and

θ is the angle of emission.

To reduce unknown parameters in equation 5.6 the following assumptions are made:

i. The instrument factors $T(E_A)$ and $D(E_A)$ are constant for all energy electrons.

ii. The concentration distribution ($N_A(z)$) is constant.

Therefore, equation 5.6 can be written as

$$I_A = k\,\sigma_A(E_p)\,R_A \times \int_0^\infty N_A(z) e^{(-z/\lambda_M(E_A)\cos\theta)} dz \tag{5.7}$$

where $R = 1 + r$ and k is a constant.

Dividing the crystal in planes parallel to the surface, each separated by the interplanar distance d equation 5.7 reduces to

$$I_A = k\,\sigma_A(E_p)\,R_A \sum_{n=0}^{\infty} N_A(nd) e^{(-nd/\lambda_{AD} \cos\theta)} \tag{5.8}$$

where $N_A(nd)$ is the atom density (in atoms/m^2) at a distance of nd from the surface.

Similar equation can be derived for the pure element A and that is

$$I_A^{\infty} = k\,\sigma_A(E_p)\,R_A^{\infty} \times \sum_{n=0}^{\infty} N_A^{\infty}(nd^{\infty}) e^{(-nd_A^{\infty}/\lambda_{AD}^{\infty} \cos\theta)} \tag{5.9}$$

The Auger yield for the element A in the alloy (note that the expression is not restricted to binary alloys) is given by [26, 28, 29]

$$I_A = k\,\sigma_A(E_p)\,R_A\,N_A \left[X_A^{\phi} + \sum_{n=1}^{\infty} X_A^{bulk} e^{(-nd/\lambda_{AD} \cos\theta)} \right] \tag{5.10}$$

where X_A^{ϕ} is the surface concentration and X_A^{bulk} is the bulk concentration of element A. N_A is the layer density.

Solving for $\sigma_A(E_p)$ from equation 5.9 and substituting in equation 5.10 the following expression is obtained.

$$I_A = I_A^{\infty} \frac{R_A}{R_A^{\infty}} \frac{N_A}{N_A^{\infty}} \frac{1}{\sum_{n=1}^{\infty} e^{(-nd_A^{\infty}/\lambda_{AD}^{\infty} \cos\theta)}} \left[X_A^{\phi} + \sum_{n=1}^{\infty} X_A^{bulk} e^{(-nd/\lambda_{AD} \cos\theta)} \right] \tag{5.11}$$

A similar expression can be written for other elements. Thus, taking the ratio of the Auger intensity of any two components A and B it follows that

$$\frac{I_A}{I_B} = \frac{I_A^{\infty}}{I_B^{\infty}} \frac{R_A}{R_B} \frac{R_B^{\infty}}{R_A^{\infty}} \frac{N_A}{N_B} \frac{N_B^{\infty}}{N_A^{\infty}} \frac{\sum_{n=0}^{\infty} e^{(-nd^B/\lambda_{BD}^{\infty}\mathsf{cos}\theta)}}{\sum_{n=0}^{\infty} e^{(-nd^A/\lambda_{AD}^{\infty}\mathsf{cos}\theta)}} \times \frac{X_A^{\phi} + X_A^{bulk} \sum_{n=1}^{\infty} e^{(-nd/\lambda_{AD}\mathsf{cos}\theta)}}{X_B^{\phi} + X_B^{bulk} \sum_{n=1}^{\infty} e^{(-nd/\lambda_{BD}\mathsf{cos}\theta)}} \tag{5.12}$$

Let

$$\alpha_{AB} = \frac{I_A^{\infty}}{I_B^{\infty}} \frac{R_A}{R_B} \frac{R_B^{\infty}}{R_A^{\infty}} \frac{N_A}{N_B} \frac{N_B^{\infty}}{N_A^{\infty}} \frac{\sum_{n=0}^{\infty} e^{(-nd^B/\lambda_B^B\mathsf{cos}\theta)}}{\sum_{n=0}^{\infty} e^{(-nd^A/\lambda_A^A\mathsf{cos}\theta)}} \tag{5.13}$$

$$\beta_A = \sum_{n=1}^{\infty} e^{(-nd/\lambda_{AD}\mathsf{cos}\theta)} \quad \textsf{and} \quad \beta_B = \sum_{n=1}^{\infty} e^{(-nd/\lambda_{BD}\mathsf{cos}\theta)} \tag{5.14}$$

Therefore, equation 5.12 is re-written as

$$\frac{I_A}{I_B} = \alpha_{AB} \frac{X_A^{\phi} + \beta_A X_A^{bulk}}{X_B^{\phi} + \beta_B X_B^{bulk}} \tag{5.15}$$

Parameters in α_{AB} and β terms:

I^{∞} is the sensetivity factor measured from pure elemental standards.

$R = 1 + r$ is the backscattering factor given by Shimizu [39] as

$$r = (0.462 - 0.777Z^{0.2})U_0^{-0.32} + (1.15Z^{0.2} - 1.05) \tag{5.16}$$

where Z is the mean atomic number of the matrix in the near surface region, $U_0 = \frac{E_0}{E_b}$, E_0 is the energy of the primary electron beam and E_b is the binding energy of the core level involved in the Auger transition.

In this work, $E_0 = 5.0\,\text{keV}, E_b^{Cu} = 931\,\text{eV}, E_b^{In} = 664\,\text{eV}$and $E_b^S = 164\,\text{eV}$.

According to Seah [26] $N_A^\infty = a_A^{-3}$ and $N_A^\infty = a_{AB}^{-3} X_A$, where a_A^3 is the atomsize of A derived from $1000\rho_M N a_M^3 = A_M$ and ρ_M is the density, N is Avogadro's number and A_M the mean atomic weight of the matrix atoms.

$a_{Cu}^\infty = 2.28\,\text{Å}, a_{In}^\infty = 2.97\,\text{Å}$ and $a_S^\infty = 2.95\,\text{Å}$

$a_A^M = a_B^M = (a_A^\infty X_A^{bulk} + a_B^\infty X_B^{bulk})$

$N_A^\infty = (a_A^\infty)^{-3}$ and $N_B^\infty = (a_B^\infty)^{-3}$

$N_A = N_B = (a_A^\infty X_A^{bulk} + a_B^\infty X_B^{bulk})^{-3}$

n is the integer representing number of layers. $n = 0$ is taken as the first layer and $n \geq 1$ as subsurface layers extending into a bulk.

$d(alloy)$, $d^A(pure)$ and $d^B(pure)$ values are taken as the mean atomic size from Seah [26].

$\lambda_A(pure), \lambda_B(pure)$ and $\lambda_A(alloy)$ values are calculated using TPP-2M formula [40] for inelastic mean free path (IMFP).

The TPP-2M formula is given by

$$\lambda = \frac{E}{E_p^2[\beta\, ln(\gamma E) - (C/E) + (D/E^2)]} \tag{5.17}$$

where

E is the electron energy,

$E_p = 28.8 \left(\frac{N_V \rho}{M}\right)^{0.5}$ is the Free-electron plasmon energy (in eV), N_V is the number of valence electrons per atom (11 for Cu, 3 for In and 6 for S), ρ is the density (in g/cm^3) and M is the atomic mass,

$\beta = -0.10 + 0.944/(E_P^2 + E_g^2)^{0.5} + 0.069\rho^{0.1}$ (E_g is the band-gap energy),

$\gamma = 0.191\rho^{-0.5}$,

$C = 1.97 - 0.91U$,

$D = 53.4 - 20.8U$,

$U = \frac{N_V \rho}{M}$.

θ is the angle of emission of Auger electrons and is taken as 42° for a cylindrical mirror analyser following from Seah [38].

$X_{\mathrm{S}}^{bulk} = 0.0008\,\mathrm{at\%}$ and $X_{\mathrm{In}}^{bulk} = 0.059\,\mathrm{at\%}$

All parameters in α_{AB} and β terms are known. Therefore, equation 5.15 can be solved to give the required surface concentration (X^{ϕ}) of any element in the alloy. The Auger intensity I_A or I_B in equation 5.15 is taken as APPH of corresponding element. AES segregation measurements discussed in section 6.3.2 were quantified using the method discussed in this section.

Part III

RESULTS AND CONCLUSION

6

Results and Discussion

6.1 Introduction

To understand the interdiffusion taking place at the interface of In/Cu thin layers, In/Cu thin films were deposited onto SiO_2 and the samples were annealed in vacuum. The In/Cu thin films were characterized with XRD and the depth profiles of those films were obtained with AES.

The In/Cu layers were also deposited onto Cu crystal and the Cu crystal was annealed in Ar gas atmosphere for doping of Cu crystal with small concentration of In. After annealing, the Cu crystal was loaded inside ultra high vacuum chamber for AES segregation measurements.

In this chapter, the results obtained from In/Cu thin films will be discussed first then the results obtained from AES segregation measurements.

6.2 In/Cu thin films results

It is mentioned in the previous section that In/Cu thin films were deposited onto SiO_2 and also onto polycrystalline Cu crystal. The In/Cu films deposited onto SiO_2 were characterized with XRD and the AES depth profiles of these films were obtained.

This section discusses the XRD results and the AES depth profiles of the In/Cu thin films that were deposited onto SiO_2 substrate.

6.2.1 In/Cu thin films XRD results

Figure 6.1 shows the XRD data of the as-prepared (un-annealed) In/Cu films for both the 500 Å and 1000 Å Cu cover layers (see the insert). From the XRD data it is clear that two phases namely $CuIn_2$ and $Cu_{11}In_9$ form at low temperature (26-39 ℃) during the film deposition. The XRD peaks corresponding to these two phases are shown in figure 6.1. The formation of these two phases ($CuIn_2$ and $Cu_{11}In_9$) at a low temperature is consistent with observation found in literature [18]. According to Keppner [18] $CuIn_2$ form at low temperatures and is only stable below 150 ℃. A $Cu_{11}In_9$ phase also forms at low temperatures and is stable below 305.8 ℃ [16].

For the un-annealed sample with the 500 Å Cu layer, a smaller Cu peak is seen at 43.262 ° that indicates that more Cu reacted in the formation of the $CuIn_2$ (at 34.455 °) and $Cu_{11}In_9$ (at 41.478 °) phases. For the un-annealed sample with the 1000 Å Cu layer, a larger Cu peak is seen at 43.262 ° that indicates that more unreacted Cu is left for the thicker Cu layer after the formation of the $CuIn_2$ and

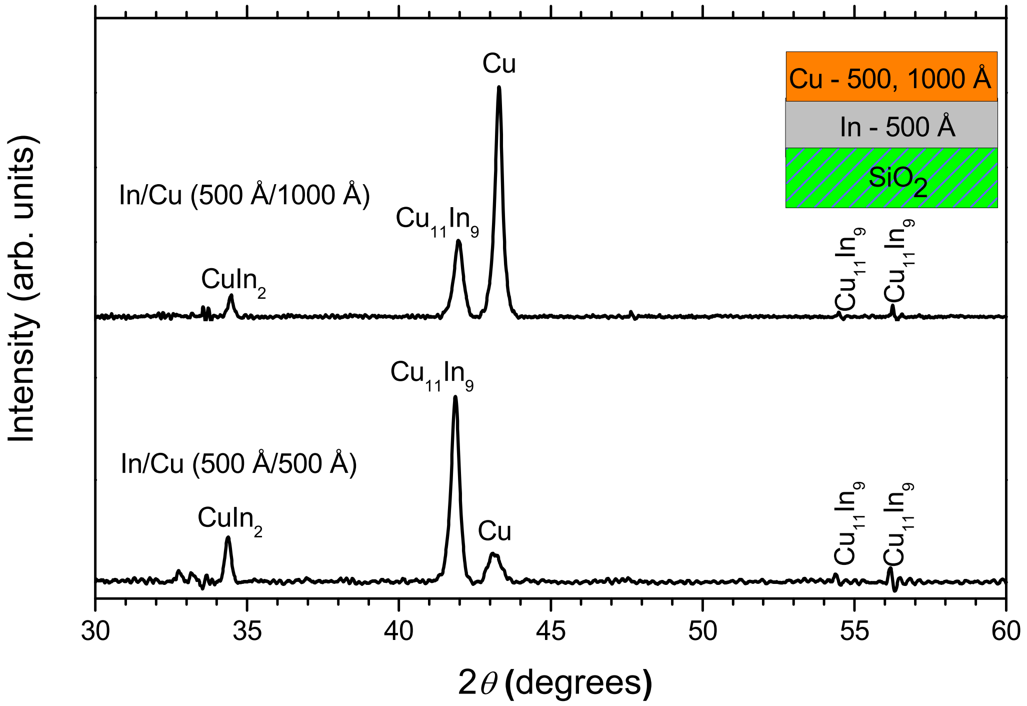

Figure 6.1: XRD data of the as-prepared (un-annealed) In/Cu thin films on a SiO_2 substrate.

$Cu_{11}In_9$ phases, as is expected. For both samples there are no pure or elemental In peaks visible in the spectra, suggesting that all pure metallic In was consumed in the phase formation process.

The standard XRD peak positions (2θ) for Cu, In, $CuIn_2$, $Cu_{11}In_9$ and Cu_2In are summarized in table 6.1. The standard data in table 6.1 is shown only in the 2θ range between 30 ° and 60 °. The XRD standards for Cu, In, $Cu_{11}In_9$, Cu_2In are from the Joint Committee on Powder Diffraction Standards (JCPDS) data files number 04-0836, 05-0642, 41-0883, 42-1475 respectively while $CuIn_2$ XRD data are those used by Keppner *et al.* [18] and Başol *et al.* [41].

The XRD data of the annealed In (500 Å)/Cu (1000 Å) thin films are shown in figure 6.2. In figure 6.2, graphs labeled A and B shows the diffraction spectra of region A and B at low intensities (at background level). The thin films were

Table 6.1: The XRD obtained data from figure 6.1 and figure 6.2. The phases indexed to the data are shown with JCPDS data (intensities are in parentheses). The bold text shows the JCPDS data corresponding to the obtained data.

Obtained data	**JCPDS data**				
	Cu	In	$CuIn_2$	$Cu_{11}In_9$	Cu_2In
2θ (°)	2θ (°)	2θ (°)	2θ (°)	2θ (°)	2θ (°)
33.453	–	32.964 (100)	33.305 (12)	**32.979** **(80)**	–
33.641	–	–	–	**32.979** **(80)**	–
34.455	–	36.327	**34.454** **(100)**	34.400 (50)	34.263 (15)
41.796	–	39.169 (36)	38.559 (24)	**41.478** **(100)**	–
42.142	–	–	43.016 (43)	42.126 (100)	**42.160** **(100)**
43.262	**43.297** **(100)**	–	43.254 (25)	–	–
54.399	50.433 (46)	54.475 (24)	–	**54.983** **(50)**	–
56.171	–	56.591 (12)	59.854 (31)	**57.256** **(60)**	58.367 (10)

annealed for 49 minutes at temperatures 150 ℃, 200 ℃, 250 ℃ and 300 ℃. After annealing the thin film at 150 ℃ for 49 minutes the $CuIn_2$ peak at 34.455 ° disappeared from the XRD spectrum while the 41.796 ° peak of $Cu_{11}In_9$ increased relative to the 43.262 ° peak of Cu. There also appeared new peaks at 33.453 °, 33.641 °, 54.399 ° and 56.171 ° corresponding to the $Cu_{11}In_9$ phase. Annealing the thin film at 200 ℃ for 49 minutes all the $Cu_{11}In_9$ peaks grew in size relative to the 43.262 ° peak of Cu (shows $Cu_{11}In_9$ phase growth). A new peak at 42.142 ° appeared in the spectrum for the thin film annealed at 250 ℃ for 49 minutes. This new peak corresponds to the 42.160 ° peak of the Cu_2In phase.

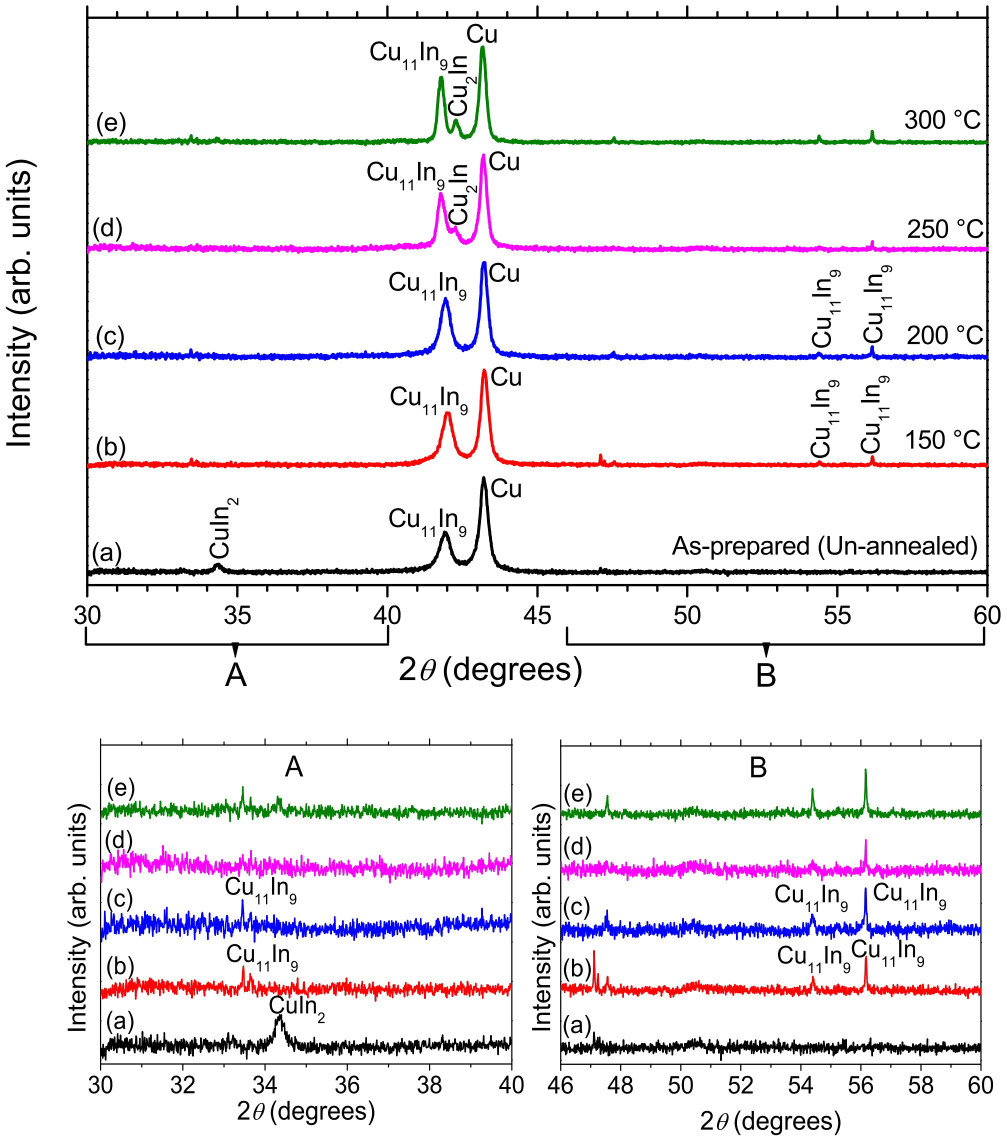

Figure 6.2: XRD data of the annealed In (500 Å)/Cu (1000 Å) thin films for 49 minutes.

6.2.2 In/Cu thin films AES results

Figure 6.3(a), shows the AES depth profiles of the as-prepared (un-annealed) In (500 Å)/Cu (1000 Å) thin film. From this depth profile it is clear that the Cu have diffused through the 500 Å In layer. This is in agreement with the XRD results, where no pure In peaks were seen.

It can be seen from the depth profile of the In (500 Å)/Cu (1000 Å) film annealed at 150 ℃ for 49 minutes (Figure 6.3(b)) that the In have diffused deeper into the Cu layer. This is clearly seen by looking at the 5 % In concentration marker. For the un-annealed sample the marker is at 400 Å (Figure 6.3(a)) while for the annealed (150 ℃) sample the marker is at 300 Å (Figure 6.3(b)) clearly showing that In diffused (100 Å) deeper into the Cu layer.

In figure 6.4(a),when the samples were annealed at 200 ℃ for 49 minutes the In diffused throughout the Cu layer and start to segregate onto the surface. The In concentration on the surface increased to 26 %. But instead of having a classical interdiffusion shape the depth profile had two plato regions indicating the formation of a phase. The phase that formed was identified with XRD data as $Cu_{11}In_9$. For the samples that were annealed at 250 ℃ and 300 ℃ for 49 minutes (Figure 6.4(b) and 6.5) the plato regions grew more prominent and the concentration levels changed, indicating the formation of new phase. This new phase that formed was identified with XRD data as Cu_2In. It was also clear from the 200 ℃, 250 ℃ and 300 ℃ AES depth profiles that In was enriched on the surface. This suggests that In segregated from a Cu matrix during a heat treatment. Therefore, In can be expected to segregate in Cu crystal.

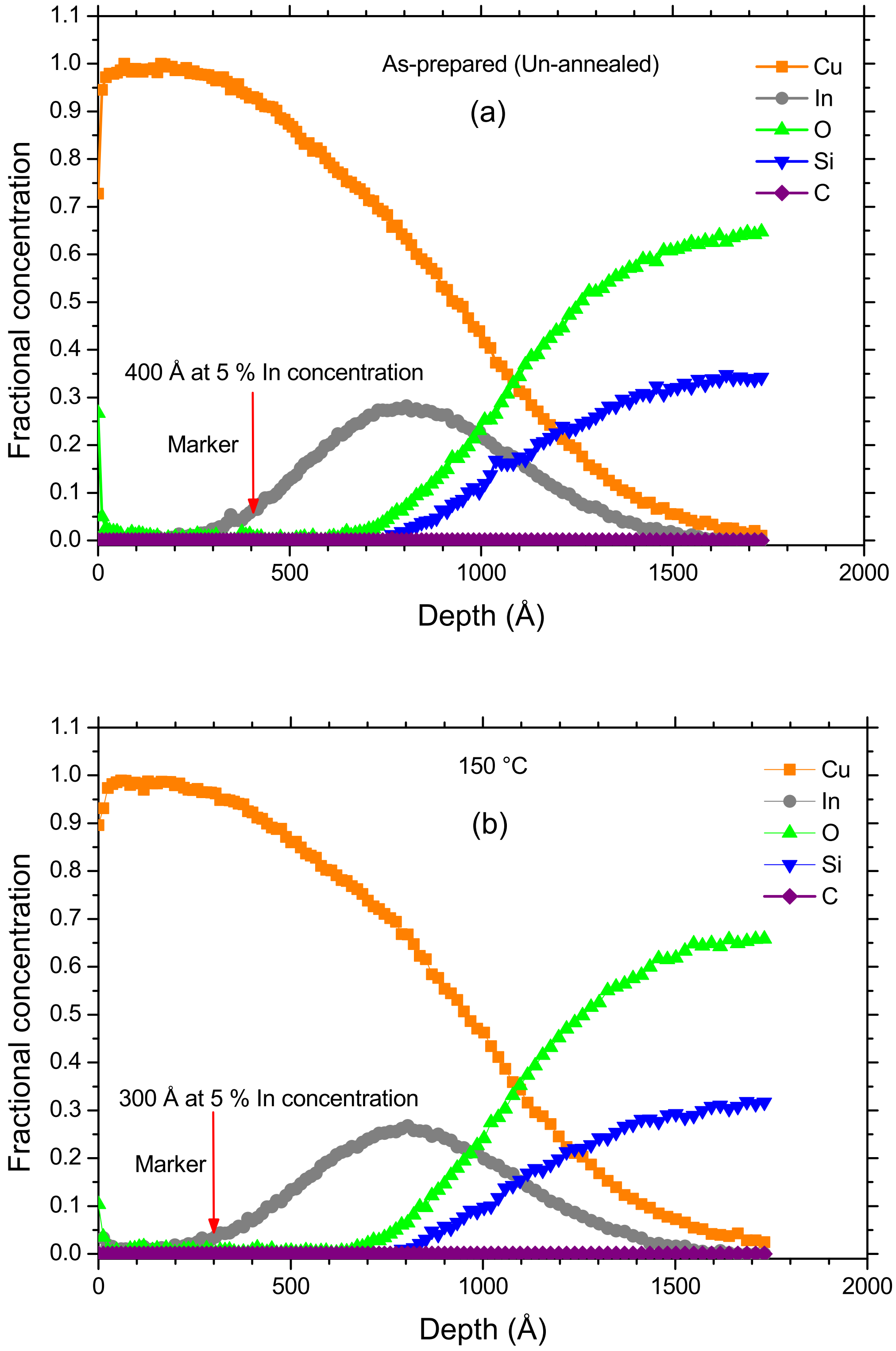

Figure 6.3: (a) AES depth profiles of the as-prepared (un-annealed) In/Cu thin films on SiO_2 substrate and (b) AES depth profiles of the annealed In/Cu thin films at 150 °C.

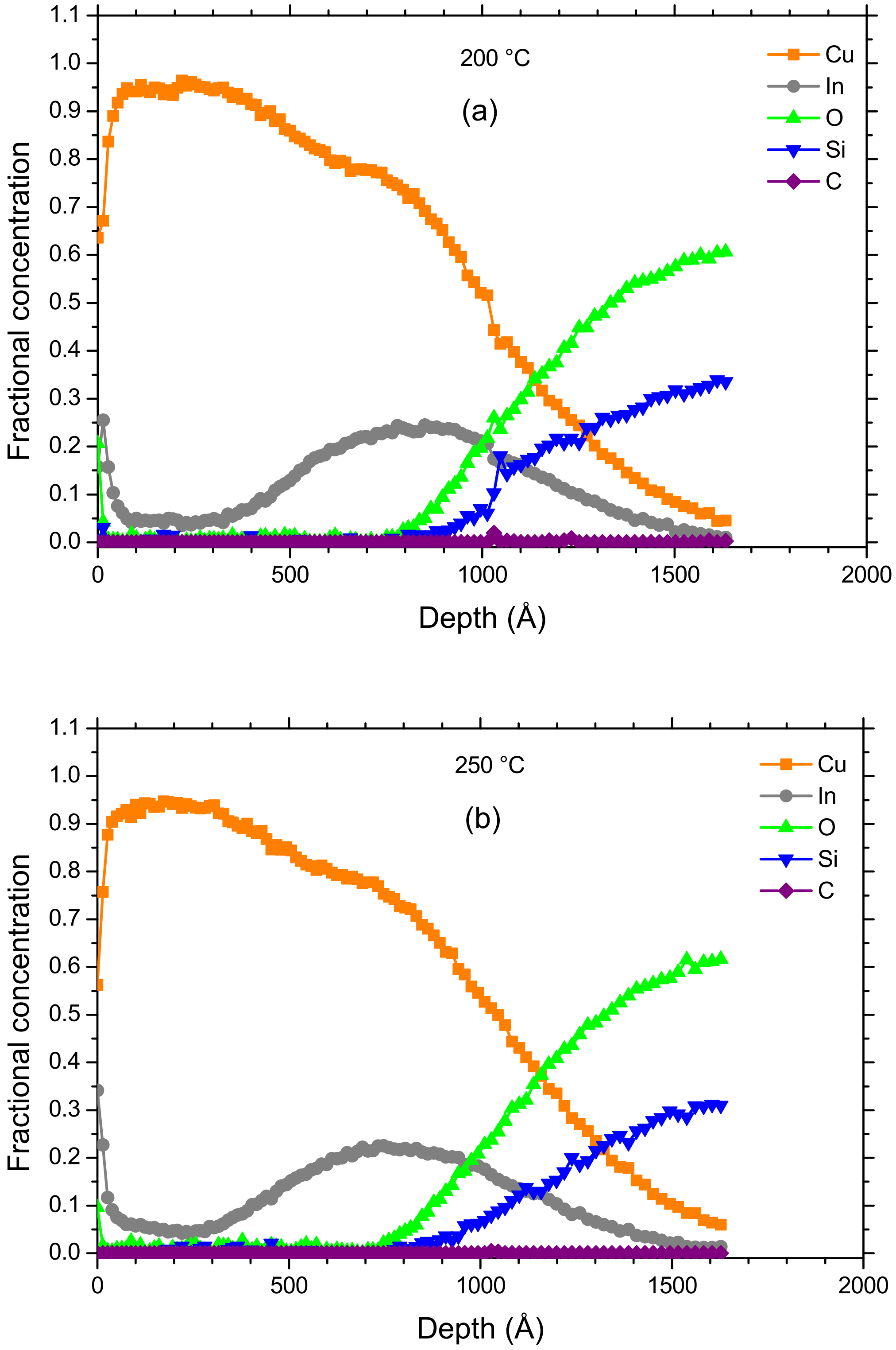

Figure 6.4: AES depth profiles of the annealed In/Cu thin films at (a) 200 ℃ and (b) 250 ℃.

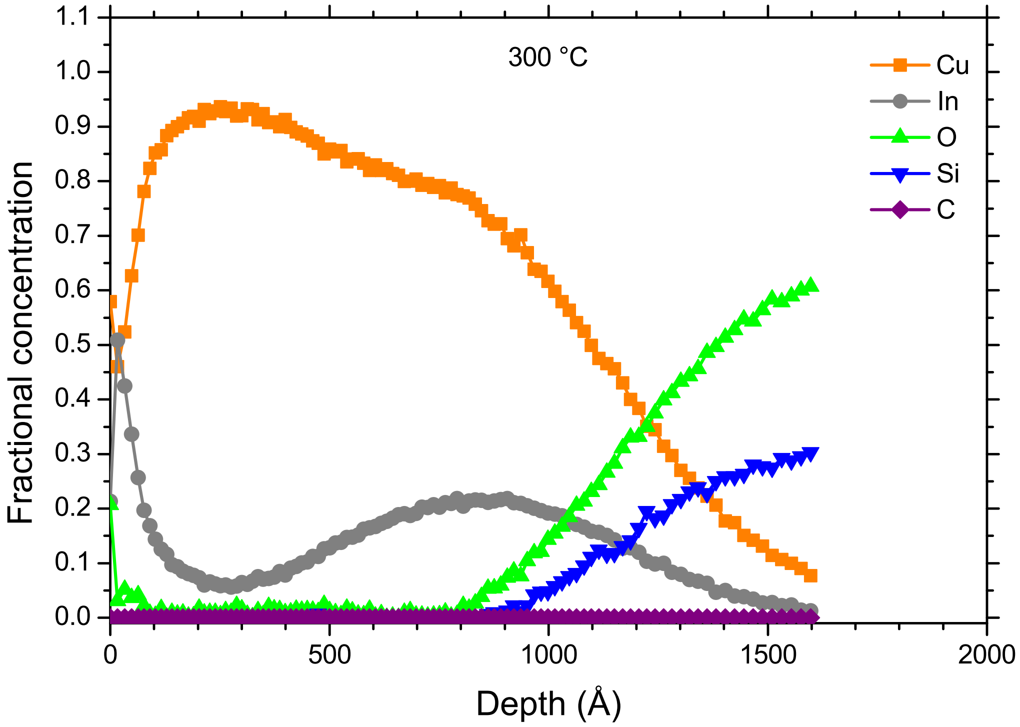

Figure 6.5: AES depth profiles of the annealed In/Cu thin films at 300 °C.

6.3 Cu(0.059 at% In) alloy results

The Cu(0.059 at% In) alloy was prepared through diffusion where a layer of In (15580 Å) coated with a Cu layer (3520 Å × 2) was deposited onto the backside of a polycrystalline Cu crystal that was further annealed in an Ar gas atmosphere for few days. The XRD data of the Cu crystal with In/Cu layers and after the Cu crystal doping process was obtained. The XRD data of the crystal will be discussed in this section.

The Cu(0.059 at% In) alloy was heated using linear temperatures and constant temperatures inside an ultra high vacuum (UHV) chamber. During heating process, AES was used to record segregation profiles by monitoring the surface condition of the Cu(0.059 at% In) alloy.

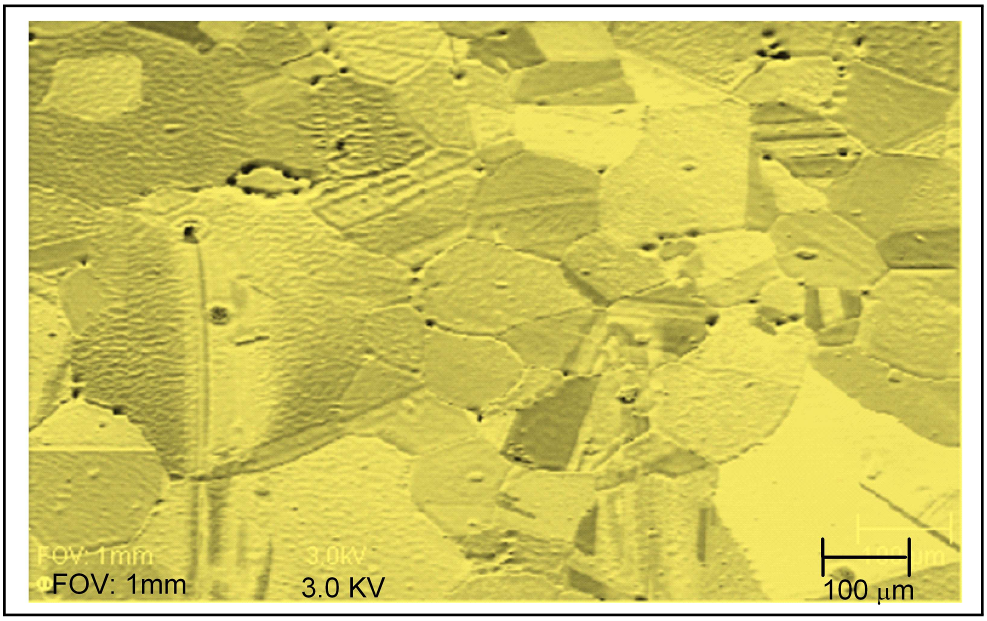

Figure 6.6: The micro-structure of polycrystalline Cu crystal after segregation measurements with an average grain size of 112 μm.

In this section, the segregation profiles obtained using both linear temperature and constant temperature measurements will be discussed. The fits of the segregation models (Fick's and Guttmann model) and the Darken simulations of segregation profiles will form part of this discussion.

Figure 6.6 shows the micro-structure of the polycrystalline Cu crystal with an average grain size of 112 μm immediately after segregation measurements. The micro-structure of the crystal surface was otained by sputtering the crystal surface with 2.0 kV argon ion beam with a current of 2.0 μA, raster area of 2mm × 2mm and the sputter rate of 8.5 nm min^{-1} for 5 min. After sputtering, a 3.0 kV primary electron beam was scanned across the crystal surface to obtain a micro-structure image.

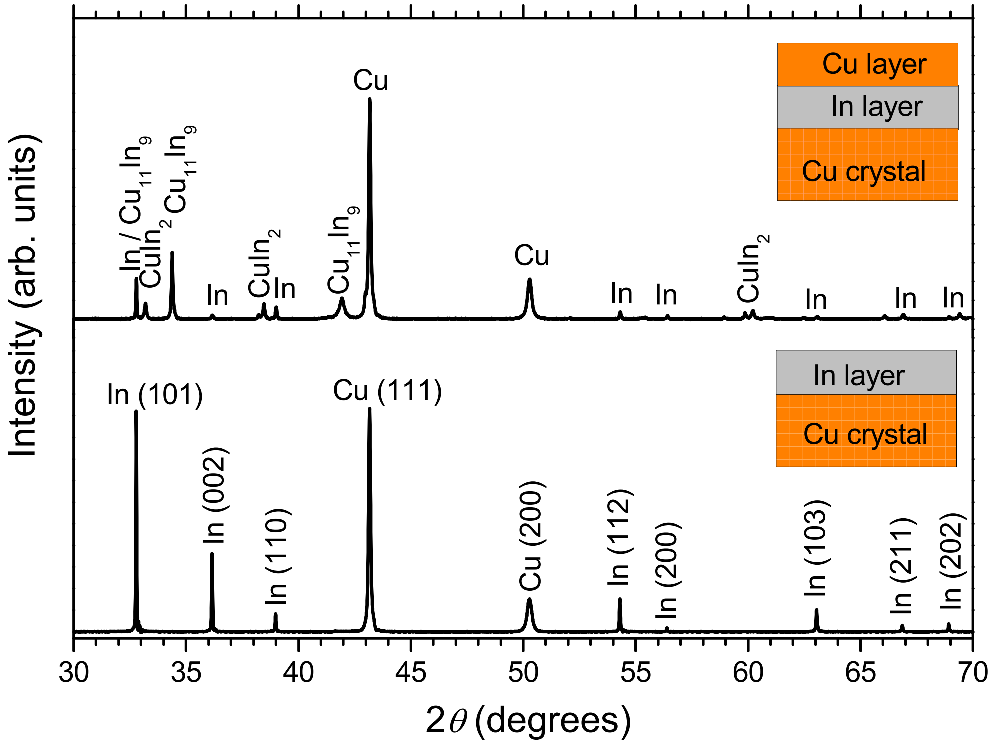

Figure 6.7: XRD data of the un-annealed Cu crystal with deposited In and Cu thin films as shown in the insert.

6.3.1 Cu(0.059 at% In) alloy XRD results

Figure 6.7 shows the XRD data of the un-annealed polycrystalline Cu crystal after In (15580 Å) and Cu (3520 Å × 2) layers deposition (see the insert). The Cu-In phases were assigned to peaks using the JCPDS data as discussed in section 6.2.1. Figure 6.7 shows the phases $CuIn_2$ and $Cu_{11}In_9$ that formed during the deposition process. This is in good agreement with the thin films results discussed in section 6.2.1.

In the sample where only an In layer (15580 Å) is deposited onto the Cu crystal (see figure 6.7), there are no phases observed. In addition, the annealing of the crystal at low annealing temperatures (below the In melting point of 156.6 ℃) will require a very long annealing time. If the annealing time is not sufficiently long to cause a complete interdiffusion of the In layer and a Cu crystal, the annealing temperature higher than 156.6 ℃ (the melting point of In) will cause In to melt and wet the crystal and likely to evaporate.

In the sample where the In layer (15580 Å) is coated with a Cu layer (3520 Å × 2) (Figure 6.7) the In that did not react during deposition will react with excess Cu during the first annealing temperature at 150 ℃ for 48 hours. It was mentioned in section 6.2.1 that $CuIn_2$ is only stable below 150 ℃. Therefore, $CuIn_2$ will decompose and react with excess Cu forming a phase that is reach in Cu ($Cu_{11}In_9$). After first annealing at 150 ℃ for 48 hours, $Cu_{11}In_9$ will be the only phase present on the Cu crystal (see section 6.2.1). Therefore, the melting point of the In/Cu layers on the Cu crystal will be that of $Cu_{11}In_9$ (305.8 ℃). The second annealing temperature at 300 ℃ for 48 hours will cause $Cu_{11}In_9$ to decompose and react with excess Cu forming a phase that is richer in Cu. In section 6.2.1, the phase was identified with XRD data as Cu_2In with the melting point of 388.3 ℃. As a result, the stepwise annealing from low to high annealing temperatures at short times increases the melting point of the In/Cu layers on the Cu crystal through interdiffusion.

Figure 6.8 shows the XRD data of the un-annealed polycrystalline Cu crystal (pure crystal) and annealed polycrystalline Cu crystal (after the full diffusion doping process). The XRD Cu(111) peak increased in the intensity from un-annealed to annealed polycrystalline Cu crystal as is shown in figure 6.8. The XRD Cu (111) peak grew at the expense of other XRD peaks suggesting that the Cu(111) grain grew at the expense of other Cu grains.

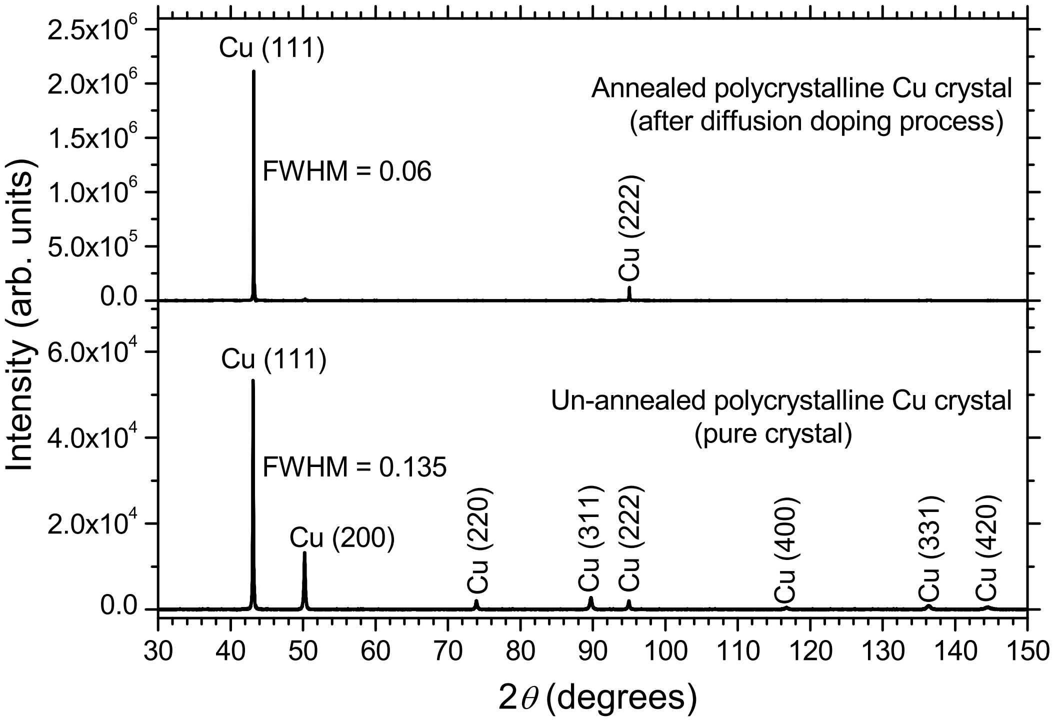

Figure 6.8: XRD data of the annealed and unannealed polycrystalline Cu crystal.

6.3.2 Cu(0.059 at% In) alloy AES segregation results

Linear temperature measurements

Figure 6.9, 6.10, 6.11(a) and 6.11(b) shows the surface enrichment of In and S in a dilute polycrystalline Cu crystal alloy obtained with the linear heating method. In Figure 6.9(a) there are four different regions shown:

In region A, the crystal temperatures are low and hence the bulk diffusion coefficient of In and S impurities is low. As a result, the impurities do not enrich the surface layer.

In region B (the In kinetic region), In segregated to the surface and reach a maximum coverage of 25 %. The surface maximum coverage of In is determined

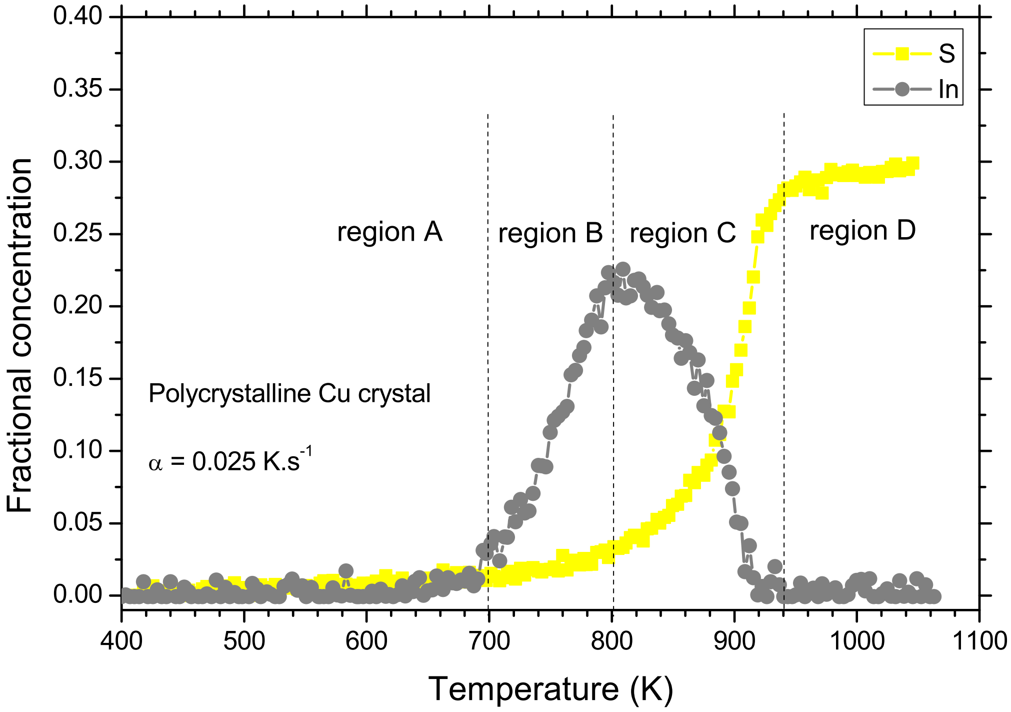

Figure 6.9: Fractional concentration as a function of temperature measured from a polycrystalline Cu crystal at heating rate of 0.025 K.s^{-1}.

by the segregation energy of In and the atomic interaction between In, Cu and S atoms.

In region C (the S kinetic region), the segregation rate of S increased, thus increasing the surface coverage of S. S as it segregates to the surface it replaces the In from the surface layer. The In replacement by S could be as result of the segregation energy for S that could be greater (more negative) than that of In.

In region D (the equilibrium region), S reached a surface maximum coverage of 29-32 % and the In surface maximum coverage is almost zero after being displaced by S. According to the Guttmann model (discussed in section 4.6), this is an indication of a large difference between the segregation energies of In and S. A maximum surface coverage of S is determined by its segregation energy (that could be more negative) and the atomic interaction between S, Cu and In

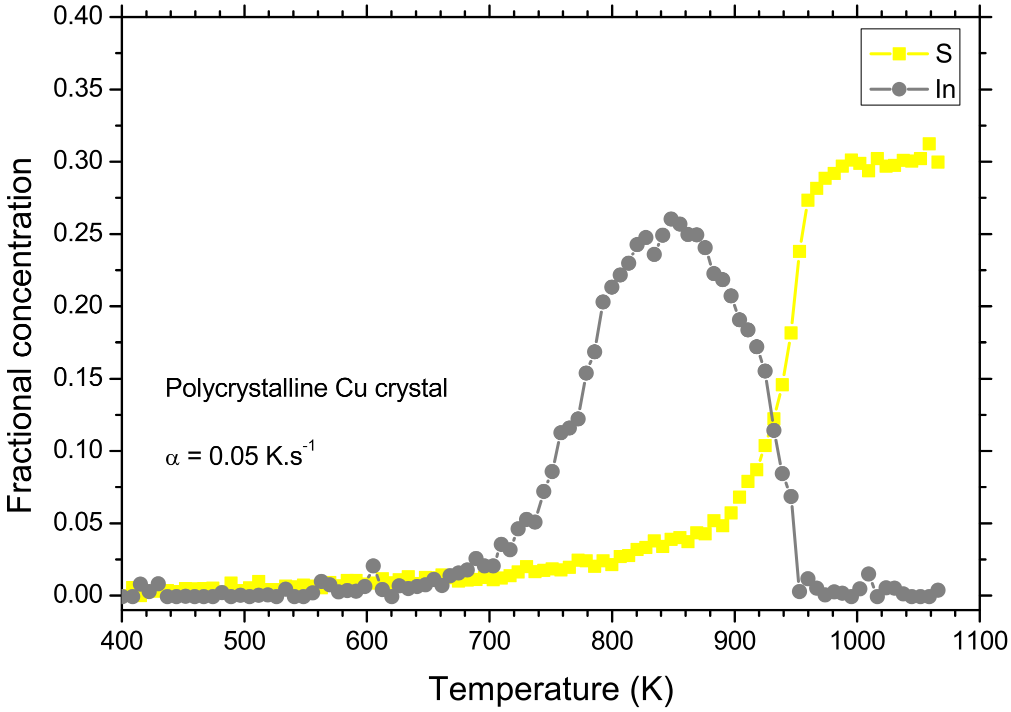

Figure 6.10: Fractional concentration as a function of temperature measured from a polycrystalline Cu crystal at heating rate of 0.05 K.s^{-1}.

atoms. Swart *et. al.* [37] have demonstrated that a repulsive interaction between two segregating species (In and S in this study) lead to a higher equilibrium concentration of specie 2 (S in this study) and a lower equilibrium concentration of specie 1 (In in this study).

Next, region B, C and D will be fitted with segregation models to yield the segregation parameters that will be used as starting parameters in Darken model simulation (that will yield the final segregation parameters).

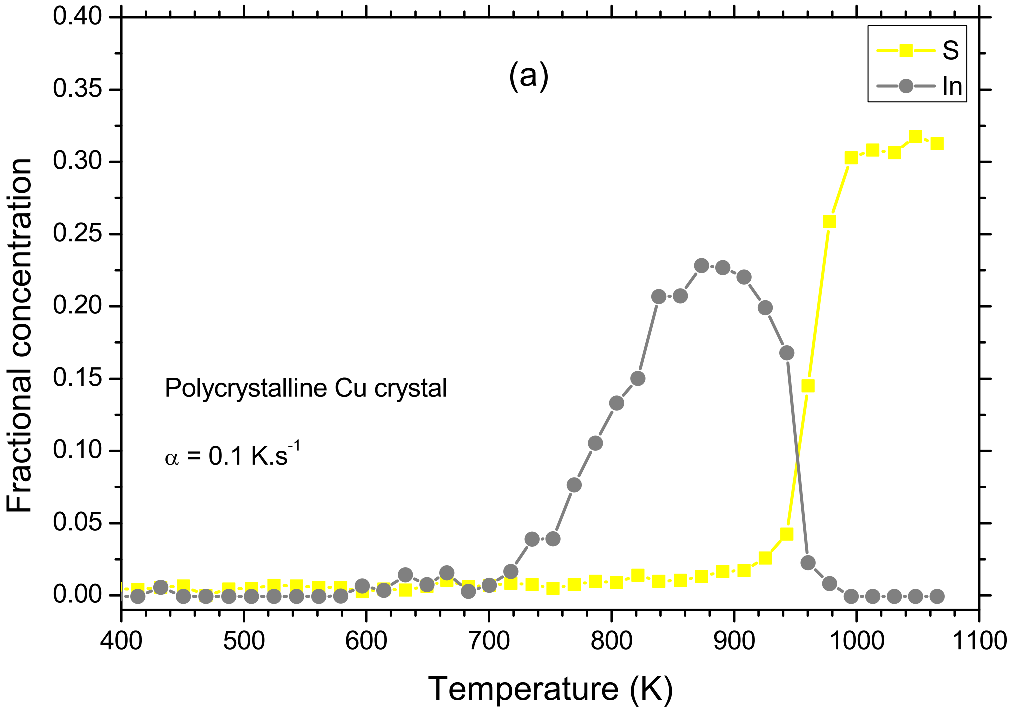

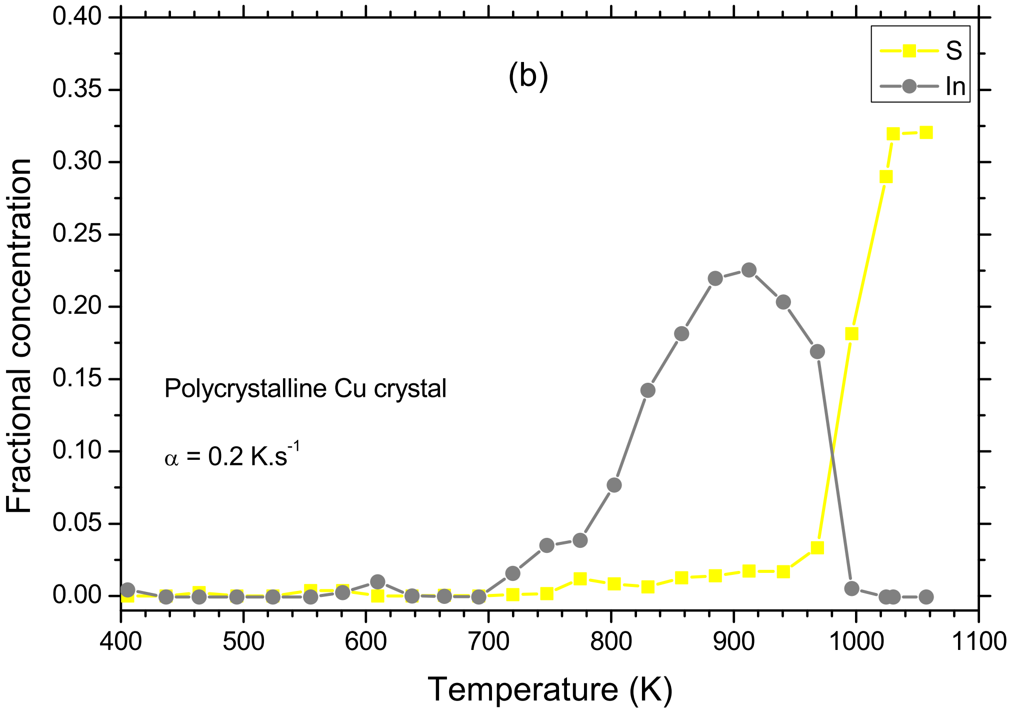

Figure 6.11: Fractional concentration as a function of temperature measured from a polycrystalline Cu crystal at heating rate of (a) 0.1 and (b) 0.2 K.s^{-1}.

Modified semi-infinity model of Fick fittings

The modified semi-infinity model of Fick given by equation 3.17 in section 3.3 is given here as equation 6.1 for fitting clarification.

$$\beta^2 = \frac{4D_0}{\pi \alpha d^2} \int_{T_0}^{T_E} e^{-Q/RT} dT \tag{6.1}$$

where $\beta = (C^{\phi} - C^{B})/(C^{B})$ with C^{ϕ} the surface concentration for In and S, C^{B} the bulk concentration for In and S (listed in table 6.2) and d the thickness of the segregated layer taken as 2.28 Å[1].

Table 6.2: The bulk concentration C^B for In and S.

Impurities	C^B (at%)
In	0.059
S	0.0008

Equation 6.1 was fitted in region B and C (the kinetic region) to obtain the parameters D_0 and Q for In and S respectively as is shown in figure 6.12, 6.13, 6.14 and 6.15 and the parameters are listed in table 6.3, 6.4, 6.5 and 6.6 respectively.

---

[1] Atom size from Seah [26]

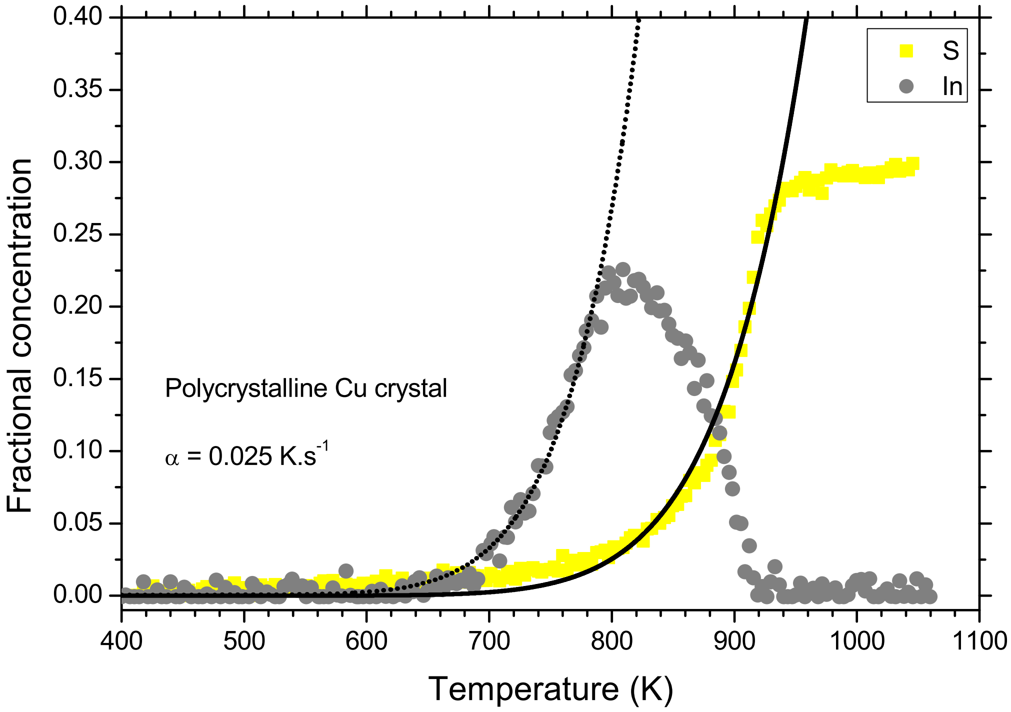

Figure 6.12: Fractional concentration as a function of temperature measured from a Cu crystal at heating rate of 0.025 K.s^{-1}. The solid and broken lines are the best fit of the modified semi-infinity model of Fick that yield D_0 and Q.

Table 6.3: Parameters obtained from the best fit of the modified semi-infinity model of Fick at heating rate of 0.025 K.s^{-1} (see figure 6.12).

Heat rate α (K.s^{-1})	Impurities	Q (kJ.mol^{-1})	D_0 (m^2.s^{-1})
0.025	In	183.4	1.4×10^{-5}
	S	206.7	2.1×10^{-2}

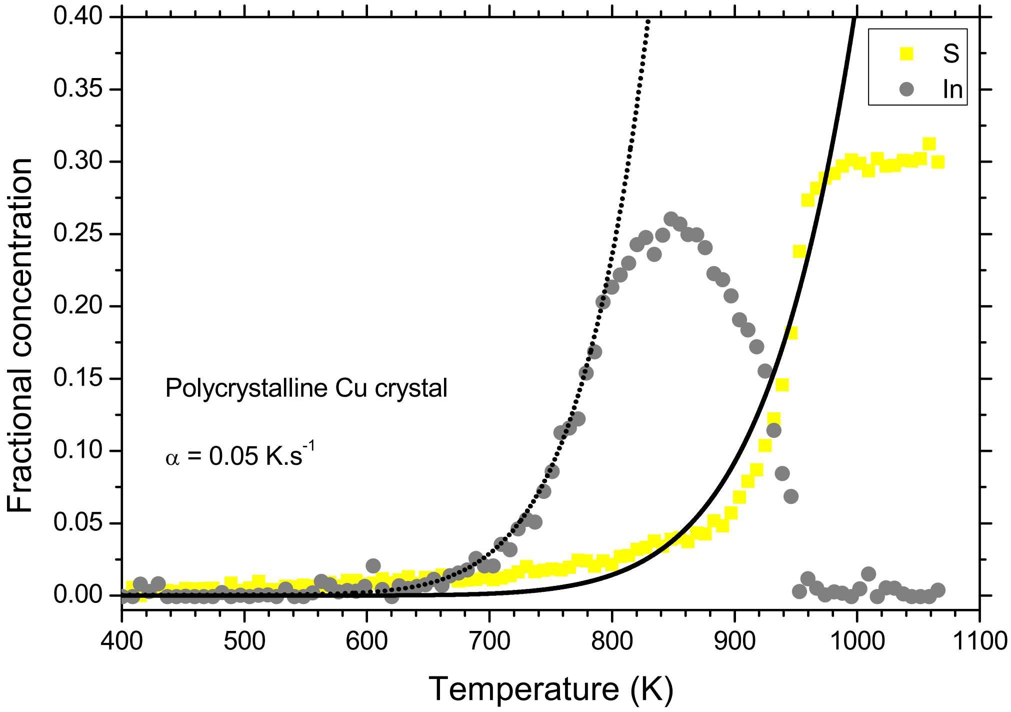

Figure 6.13: Fractional concentration as a function of temperature measured from a Cu crystal at heating rate of 0.05 K.s^{-1}. The solid and broken lines are the best fit of the modified semi-infinity model of Fick that yield D_0 and Q.

Table 6.4: Parameters obtained from the best fit of the modified semi-infinity model of Fick for heat rate of 0.05 K.s^{-1} (see figure 6.13).

Heat rate α (K.s^{-1})	Impurities	Q (kJ.mol^{-1})	D_0 (m^2.s^{-1})
0.05	In	184.1	2.0×10^{-5}
	S	208.6	1.8×10^{-2}

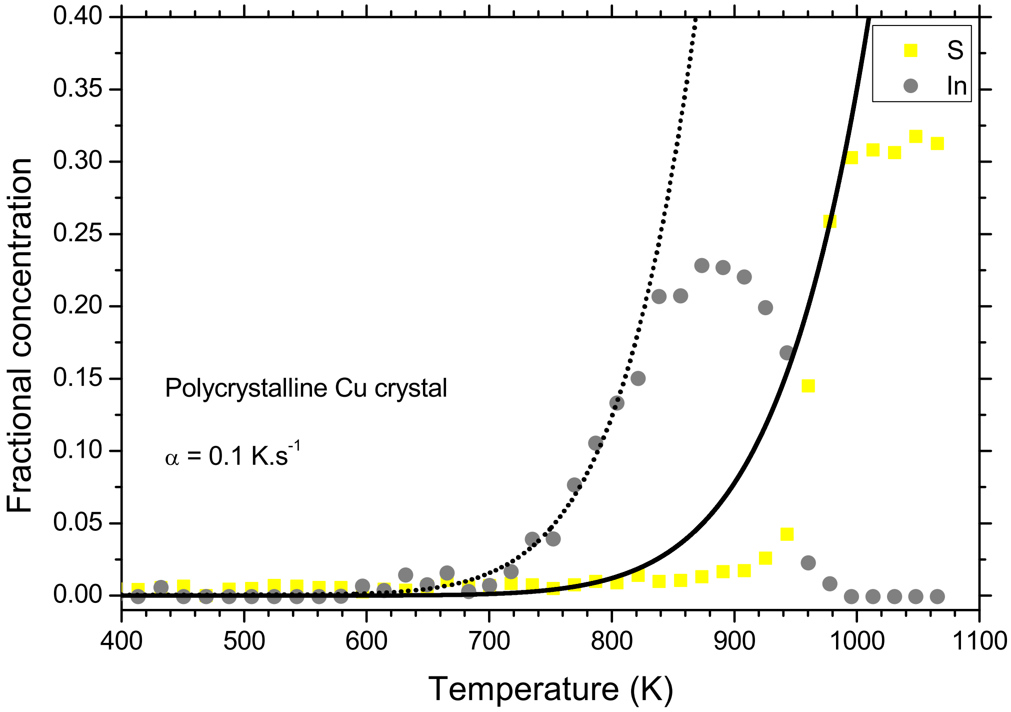

Figure 6.14: Fractional concentration as a function of temperature measured from a Cu crystal at heating rate of 0.1 K.s^{-1}. The solid and broken lines are the best fit of the modified semi-infinity model of Fick that yield D_0 and Q.

Table 6.5: Parameters obtained from the best fit of the modified semi-infinity model of Fick for heat rate of 0.1 K.s^{-1} (see figure 6.14).

Heat rate α (K.s^{-1})	Impurities	Q (kJ.mol^{-1})	D_0 (m^2.s^{-1})
0.1	In	184.1	1.1×10^{-5}
	S	209.5	2.9×10^{-2}

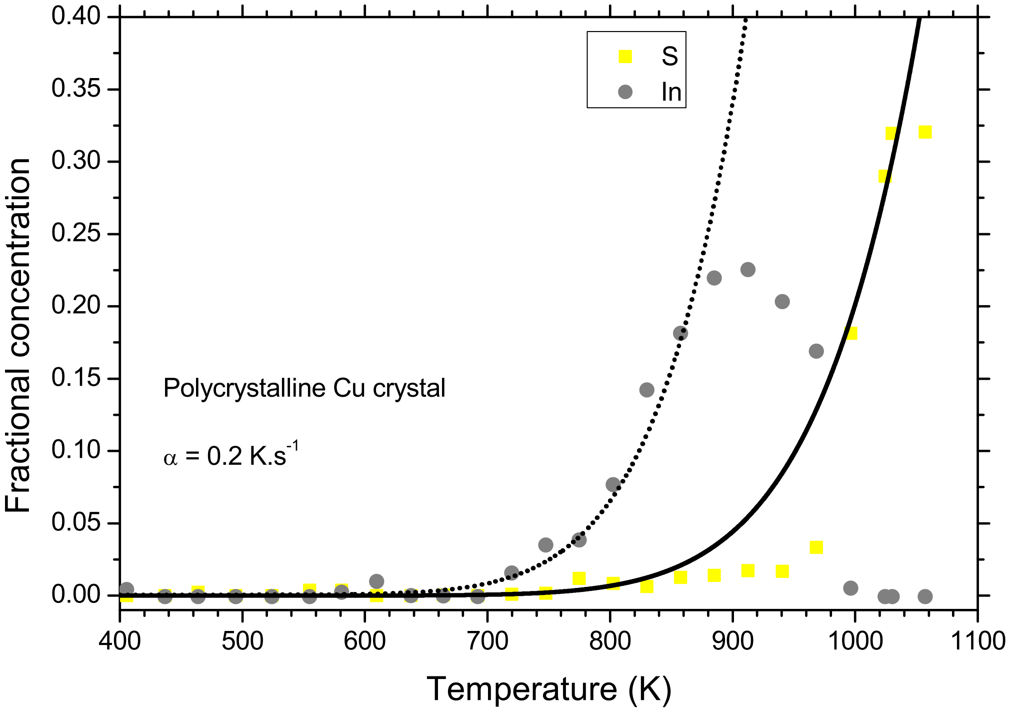

Figure 6.15: Fractional concentration as a function of temperature measured from a Cu crystal at heating rate of 0.2 K.s^{-1}. The solid and broken lines are the best fit of the modified semi-infinity model of Fick that yield D_0 and Q.

Table 6.6: Parameters obtained from the best fit of the modified semi-infinity model of Fick for heat rate of 0.2 K.s^{-1} (see figure 6.15).

Heat rate α (K.s^{-1})	Impurities	Q (kJ.mol^{-1})	D_0 (m^2.s^{-1})
0.2	In	184.0	0.6×10^{-5}
	S	211.3	2.4×10^{-2}

A summary of all fit parameters obtained from the fittings of the modified semi-infinity model of Fick is shown in table 6.7. The segregation parameters measured for all heat rates are equivalent.

In table 6.7 it can be seen that the activation energy (Q) and the pre-exponential factor D_0 for In bulk diffusion are smaller than for S. Therefore, S atoms have high bulk diffusivity than In atoms in Cu crystal. At low temperatures (region B in figure 6.9) In segregated first and faster than S and that could be as a result of the lower activation energy for In ($Q = 183.9$ kJ.mol^{-1}) which is lower than that for S ($Q = 209.0$ kJ.mol^{-1}) and high bulk concentration of In (0.059 at%) which is much higher than that of S (0.0008 at%).

Table 6.7: A summary of all fit parameters obtained from the fittings of the modified semi-infinity model of Fick.

Heat rate	In		S	
α (K.s^{-1})	Q (kJ.mol^{-1})	D_0 (m^2.s^{-1})	Q (kJ.mol^{-1})	D_0 (m^2.s^{-1})
0.025	183.4	1.4×10^{-5}	206.7	2.1×10^{-2}
0.05	184.1	2.0×10^{-5}	208.6	1.8×10^{-2}
0.1	184.1	1.1×10^{-5}	209.5	2.9×10^{-2}
0.2	184.0	0.6×10^{-5}	211.3	2.4×10^{-2}
Average:	183.9	1.3×10^{-5}	209.0	2.3×10^{-2}

Note that Fick fits ignores the interaction energies between atoms as it is derived with the assumption that there is no interaction between atoms during segregation. The average values of parameters D_0 and Q will be used as starting parameters in Darken simulations.

Guttmann model fittings

The Guttmann equations listed as equation 4.32, 4.33, 4.34, 4.35 and equation 4.36 in section 4.6 are shown here as equation 6.2, 6.3, 6.4, 6.5 and equation 6.6 for the fitting purpose.

$$X_1^{\phi} = \frac{X_1^B \exp(\Delta G_1/RT)}{1 - X_1^B + X_1^B \exp(\Delta G_1/RT) - X_2^B + X_2^B \exp(\Delta G_2/RT)} \tag{6.2}$$

$$X_2^{\phi} = \frac{X_2^B \exp(\Delta G_2/RT)}{1 - X_2^B + X_2^B \exp(\Delta G_2/RT) - X_1^B + X_1^B \exp(\Delta G_1/RT)} \tag{6.3}$$

where

$$\Delta G_1 = \Delta G_1^0 + 2\Omega_{13}(X_1^B - X_1^{\phi}) + \Omega'(X_2^{\phi} - X_2^B) \tag{6.4}$$

$$\Delta G_2 = \Delta G_2^0 + 2\Omega_{23}(X_2^B - X_2^{\phi}) + \Omega'(X_1^{\phi} - X_1^B) \tag{6.5}$$

and

$$\Omega' = \Omega_{12} - \Omega_{13} - \Omega_{23} \tag{6.6}$$

with ΔG_i the segregation energy of species i and Ω_{ij} is the interaction energy between species i and j.

X_1^ϕ and X_2^ϕ are calculated surface concentrations for In and S respectively. X_1^B and X_2^B are the bulk concentrations for In and S respectively (listed in table 6.2). Ω_{12} is the interaction energy for In and S atoms, Ω_{13} is the interaction energy for In and Cu atoms and Ω_{23} is the interaction energy for S and Cu atoms. ΔG_i^0 is the standard segregation energy for specie i segregation between the surface and the bulk.

In the Guttmann equations the starting parameters (ΔG_i^0 and Ω_{ij}) are substituted in the equations and the surface concentration X_i^ϕ is calculated and compared to the measured surface concentrations for the best fits. The best fits of the Guttmann equations yields the segregation parameters (ΔG_i and Ω_{ij}). The best fits of Guttmann model through segregation data are shown in figure 6.16, 6.17, 6.18 and 6.19 and the parameters are listed in table 6.8, 6.9, 6.10 and 6.11 respectively.

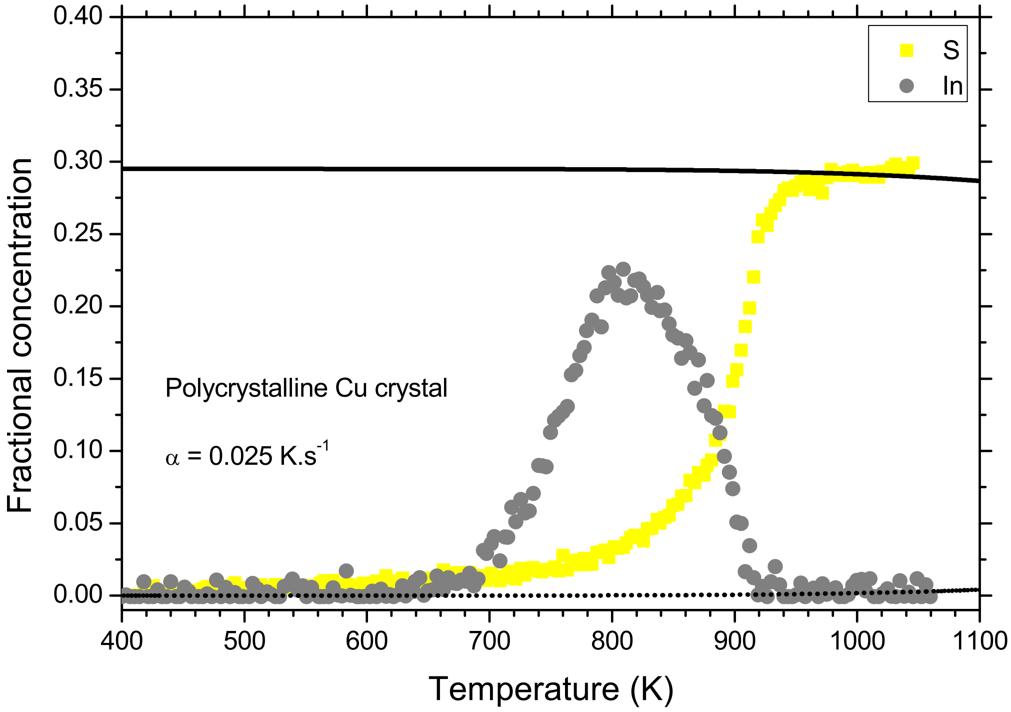

Figure 6.16: Fractional concentration as a function of temperature measured from a polycrystalline Cu crystal at heating rate of 0.025 K.s^{-1}. The solid and broken lines are the best fit of the Guttmann model that yield ΔG and Ω.

Table 6.8: Parameters obtained from the best fit of the Guttmann model (see figure 6.16). X in the parameter $\Omega_{\text{X-Cu}}$ denotes either In or S.

Heat rate α (K.s^{-1})	Impurities	ΔG (kJ.mol^{-1})	$\Omega_{\text{X-Cu}}$ (kJ.mol^{-1})	$\Omega_{\text{In-S}}$ (kJ.mol^{-1})
0.025	In	−57.2	3.1	–
	In/S	–	–	−4.2
	S	−120.2	23.2	–

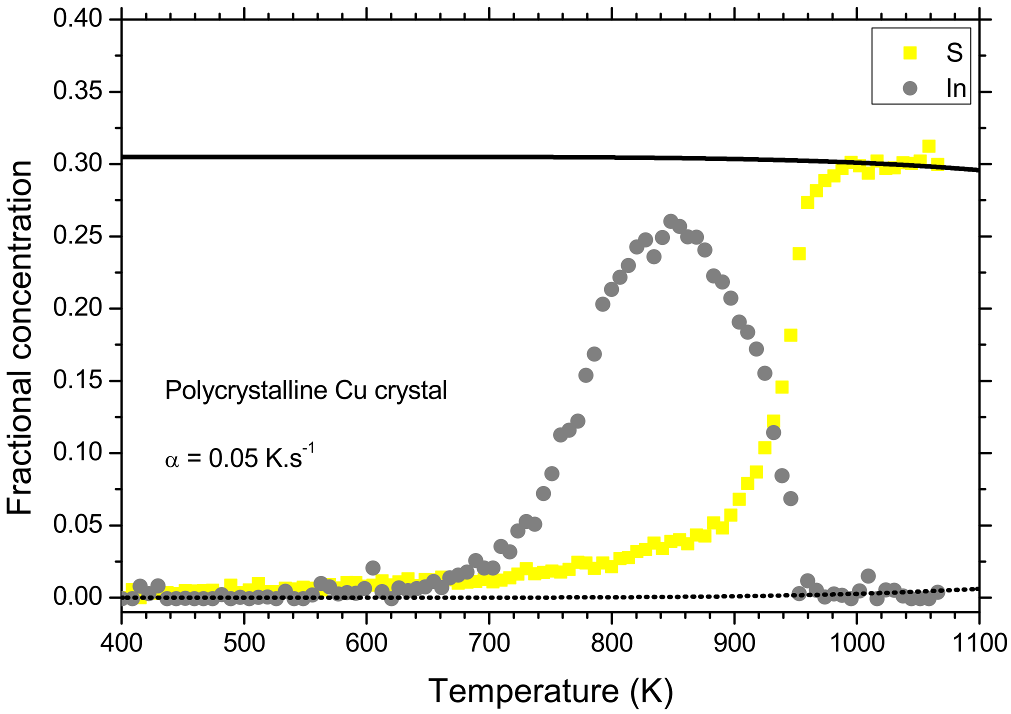

Figure 6.17: Fractional concentration as a function of temperature measured from a polycrystalline Cu crystal at heating rate of 0.05 K.s^{-1}. The solid and broken lines are the best fit of the Guttmann model that yield ΔG and Ω.

Table 6.9: Parameters obtained from the best fit of the Guttmann model (see figure 6.17). X in the parameter $\Omega_{\text{X-Cu}}$ denotes either In or S.

Heat rate α (K.s^{-1})	Impurities	ΔG (kJ.mol^{-1})	$\Omega_{\text{X-Cu}}$ (kJ.mol^{-1})	$\Omega_{\text{In-S}}$ (kJ.mol^{-1})
0.05	In	−62.8	3.1	–
	In/S	–	–	−4.2
	S	−120.2	25.3	–

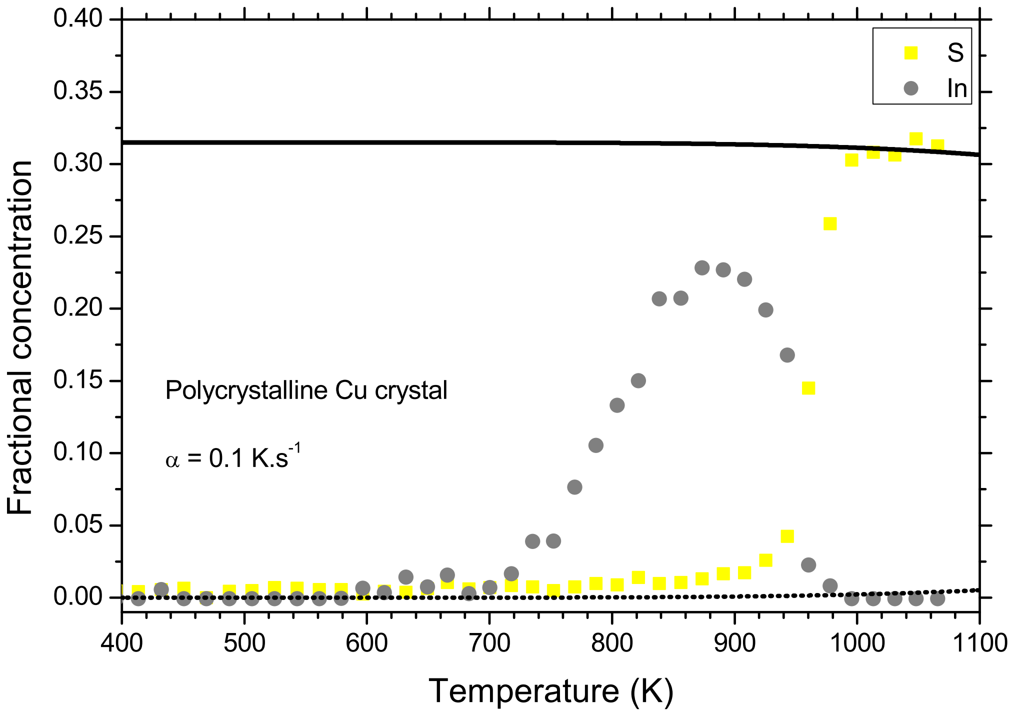

Figure 6.18: Fractional concentration as a function of temperature measured from a polycrystalline Cu crystal at heating rate of 0.1 K.s^{-1}. The solid and broken lines are the best fit of the Guttmann model that yield ΔG and Ω.

Table 6.10: Parameters obtained from the best fit of the Guttmann model (see figure 6.18). X in the parameter $\Omega_{\text{X-Cu}}$ denotes either In or S.

Heat rate α (K.s^{-1})	Impurities	ΔG (kJ.mol^{-1})	$\Omega_{\text{X-Cu}}$ (kJ.mol^{-1})	$\Omega_{\text{In-S}}$ (kJ.mol^{-1})
0.1	In	−60.0	3.4	–
	In/S	–	–	−4.2
	S	−120.2	24.5	–

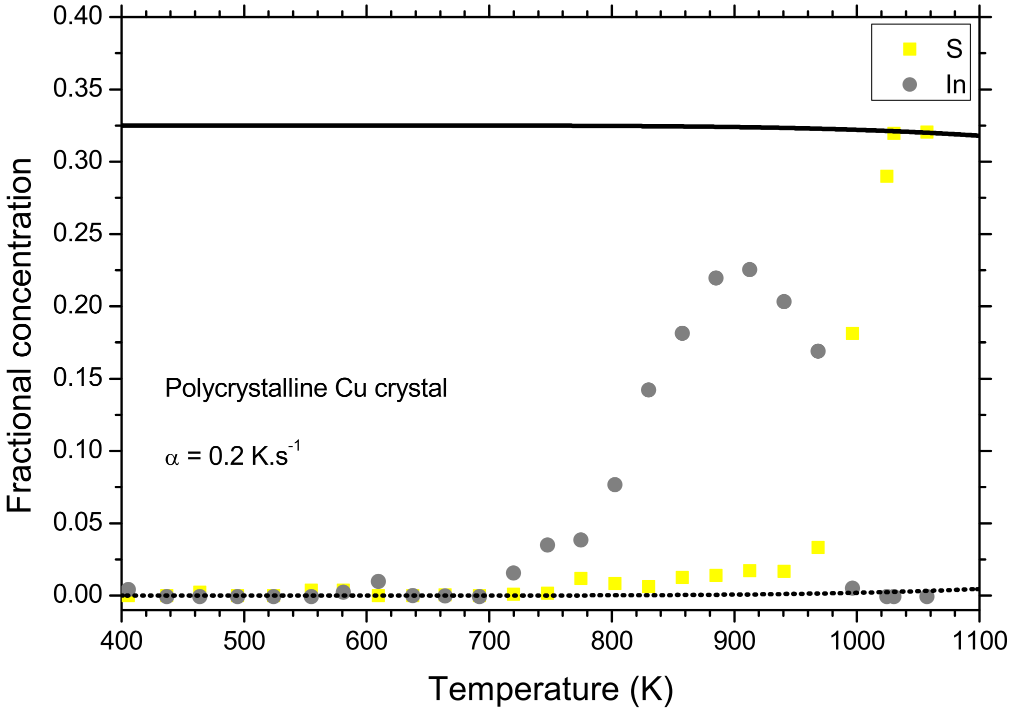

Figure 6.19: Fractional concentration as a function of temperature measured from a polycrystalline Cu crystal at heating rate of 0.2 K.s^{-1}. The solid and broken lines are the best fit of the Guttmann model that yield ΔG and Ω.

Table 6.11: Parameters obtained from the best fit of the Guttmann model (see figure 6.19). X in the parameter $\Omega_{\text{X-Cu}}$ denotes either In or S.

Heat rate α (K.s^{-1})	Impurities	ΔG (kJ.mol^{-1})	$\Omega_{\text{X-Cu}}$ (kJ.mol^{-1})	$\Omega_{\text{In-S}}$ (kJ.mol^{-1})
0.2	In	−61.4	3.3	–
	In/S	–	–	−4.0
	S	−120.8	26.4	–

A summary of all fit parameters (segregation and interaction energies) obtained from the fittings of the Guttmann model at different heating rates is shown in table 6.12. The average values of segregation parameters ΔG and Ω are shown. According to Guttmann equations, the equilibrium conditions depend on the segregation and the interaction energies and independent of the bulk diffusivity.

From Guttmann fits, it is noticeable that there is a large difference in segregation energies of In ($\Delta G = -60.4$ kJ.mol^{-1}) and S ($\Delta G = -120.5$ kJ.mol^{-1}) and that elaborates displacement of In in the surface by S. A strong attraction between the atoms of In and Cu ($\Omega_{\text{In-Cu}}$) has an energy of 3.2 kJ.mol^{-1}. A strong attraction between the atoms of S and Cu ($\Omega_{\text{S-Cu}}$) has an energy of 24.9 kJ.mol^{-1}. There is also a strong repulsion between two impurities (In and S) atoms ($\Omega_{\text{In-Cu}}$) and it has an energy of -4.1 kJ.mol^{-1}.

Table 6.12: A summary of fit parameters obtained from the fittings of the Guttmann model for different heat rates.

Heat rate	In		S		In/S
α (K/s)	ΔG (kJ/mol)	$\Omega_{\text{In-Cu}}$ (kJ/mol)	ΔG (kJ/mol)	$\Omega_{\text{S-Cu}}$ (kJ/mol)	$\Omega_{\text{In-S}}$ (kJ/mol)
0.025	−57.2	3.1	−120.2	23.2	−4.2
0.05	−62.8	3.1	−120.2	25.3	−4.2
0.1	−60.0	3.4	−120.2	24.5	−4.2
0.2	−61.4	3.3	−120.8	26.4	−4.0
Average:	−60.4	3.2	−120.5	24.9	−4.1

The average values shown in table 6.12 will be used as starting parameters in Darken simulations.

The modified Darken model simulations

The Darken equations listed as equation 4.29 in section 4.5 are listed here as equation 6.7 for segregation profiles simulations discussion. The Darken model calculates the concentration change of specie i in discrete layers as a function of time (that is for both the kinetic region and the equilibrium region). Therefore, with Darken model a complete simulation of segregation profiles can be obtained including a set of segregation parameters (D_0, Q, ΔG and Ω).

$$\begin{aligned}
\frac{\partial X_i^{\phi}}{\partial t} &= \left[\frac{M_i^{(B_1\to\phi)}X_i^{B_1}}{d^2}\Delta\mu_i^{(B_1\to\phi)}\right]; \\
\frac{\partial X_i^{B_1}}{\partial t} &= \left[\frac{M_i^{(B_2\to B_1)}X_i^{B_2}}{d^2}\Delta\mu_i^{(B_2\to B_1)} - \frac{M_i^{(B_1\to\phi)}X_i^{B_1}}{d^2}\Delta\mu_i^{(B_1\to\phi)}\right]; \\
&\vdots \\
\frac{\partial X_i^{j}}{\partial t} &= \left[\frac{M_i^{(j+1\to j)}X_i^{(j+1)}}{d^2}\Delta\mu_i^{(j+1\to j)} - \frac{M_i^{(j\to j-1)}X_i^{j}}{d^2}\Delta\mu_i^{(j\to j-1)}\right] \qquad (6.7)
\end{aligned}$$

The mobility of specie i is related to the diffusion coefficient via $M_i = D_i/RT$. The segregation energy ΔG_i and the interaction energy Ω_{ij} are carried out in the chemical potential term $\Delta\mu_i$. The bulk concentration X^B of In and S are listed in table 6.2 and d the thickness of the segregated layer is 2.28 Å.

Equation 6.7 is solved numerically with computer program.

The initial segregation parameters used in the Darken model are obtained from the fits of modified semi-infinity model of Fick and the Guttmann model. The best Darken simulations of segregation profiles are shown in figure 6.20, 6.21, 6.22 and 6.23 and the parameters are listed in table 6.13, 6.14, 6.15 and 6.16 respectively.

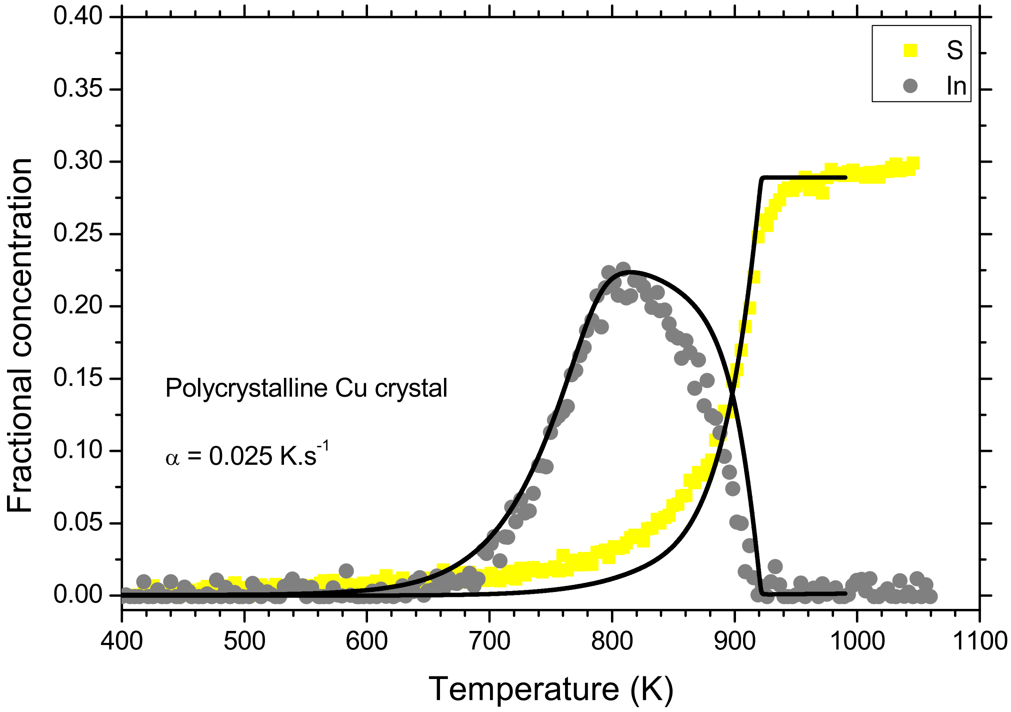

Figure 6.20: Fractional concentration as a function of temperature measured from a polycrystalline Cu crystal at heating rate of 0.025 K.s^{-1}. The solid lines are the Darken simulation that incorporate parameters D_0, Q, ΔG and Ω.

Table 6.13: Parameters obtained from the Darken simulation (see figure 6.20) at heat rate of 0.025 K.s^{-1}. X in the parameter $\Omega_{\text{X-Cu}}$ denotes either In or S.

Impurities	D_0 (m^2.s^{-1})	Q (kJ.mol^{-1})	ΔG (kJ.mol^{-1})	$\Omega_{\text{X-Cu}}$ (kJ.mol^{-1})	$\Omega_{\text{In-S}}$ (kJ.mol^{-1})
In	1.8×10^{-5}	183.3	−57.2	3.0	–
In/S	–	–	–	–	−4.0
S	9.6×10^{-3}	210.2	−120.0	23.0	–

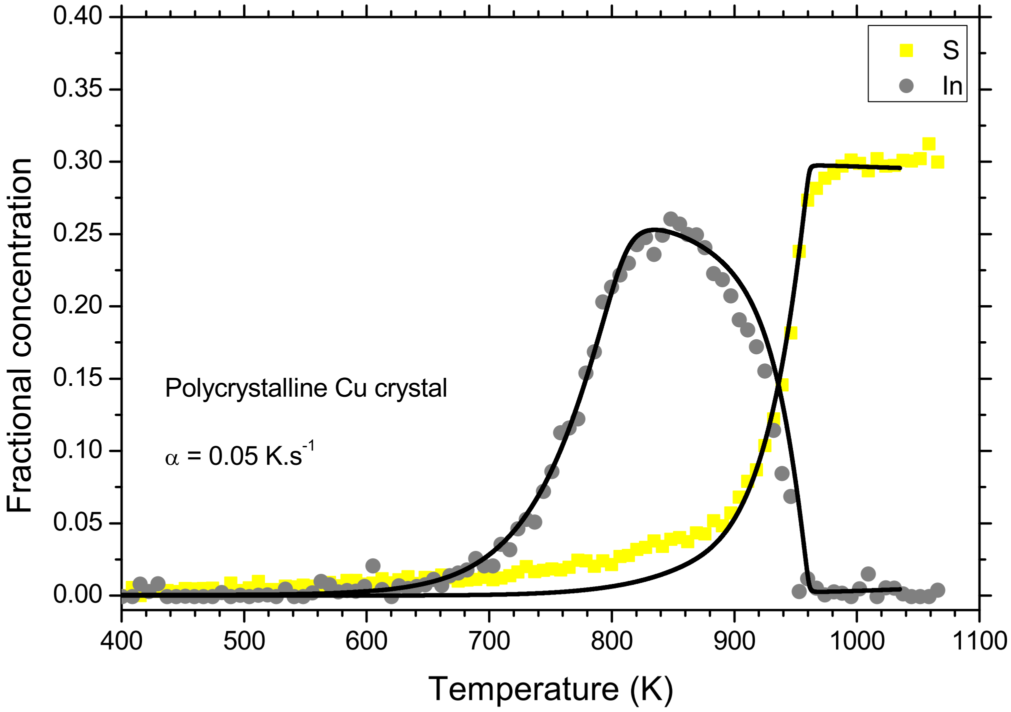

Figure 6.21: Fractional concentration as a function of temperature measured from a polycrystalline Cu crystal at heating rate of 0.05 K.s^{-1}. The solid lines are the Darken simulation that incorporate parameters D_0, Q, ΔG and Ω.

Table 6.14: Parameters obtained from the Darken simulation (see figure 6.21) at heat rate of 0.05 K.s^{-1}. X in the parameter $\Omega_{\text{X-Cu}}$ denotes either In or S.

Impurities	D_0 (m^2.s^{-1})	Q (kJ.mol^{-1})	ΔG (kJ.mol^{-1})	$\Omega_{\text{X-Cu}}$ (kJ.mol^{-1})	$\Omega_{\text{In-S}}$ (kJ.mol^{-1})
In	2.5×10^{-5}	184.3	-62.8	3.0	–
In/S	–	–	–	–	-4.0
S	8.8×10^{-3}	213.0	-120.0	23.0	–

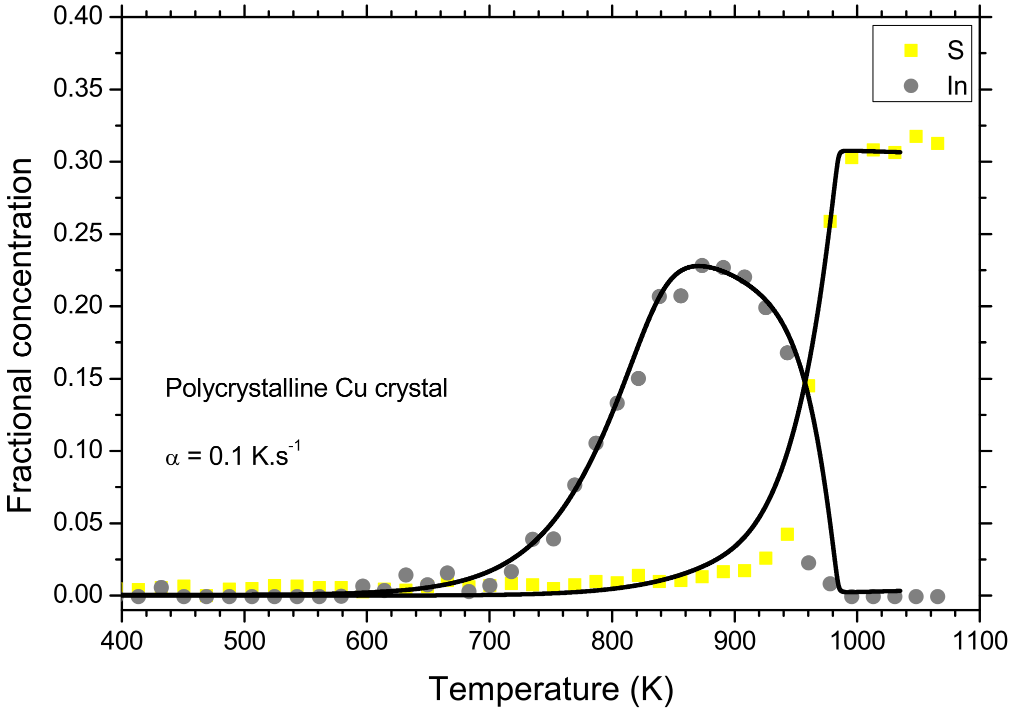

Figure 6.22: Fractional concentration as a function of temperature measured from a polycrystalline Cu crystal at heating rate of 0.1 K.s^{-1}. The solid lines are the Darken simulation that incorporate parameters D_0, Q, ΔG and Ω.

Table 6.15: Parameters obtained from the Darken simulation (see figure 6.22) at heat rate of 0.1 K.s^{-1}. X in the parameter $\Omega_{\text{X-Cu}}$ denotes either In or S.

Impurities	D_0 (m^2.s^{-1})	Q (kJ.mol^{-1})	ΔG (kJ.mol^{-1})	$\Omega_{\text{X-Cu}}$ (kJ.mol^{-1})	$\Omega_{\text{In-S}}$ (kJ.mol^{-1})
In	1.4×10^{-5}	184.3	-60.0	3.0	–
In/S	–	–	–	–	-4.0
S	9.0×10^{-3}	212.6	-120.0	23.0	–

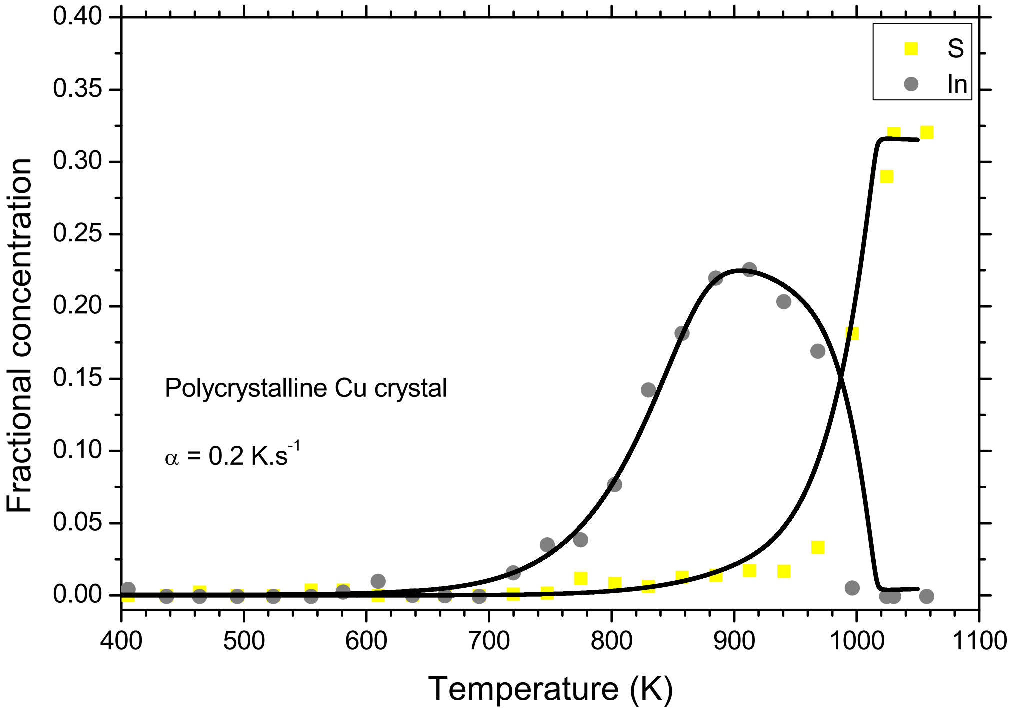

Figure 6.23: Fractional concentration as a function of temperature measured from a polycrystalline Cu crystal at heating rate of 0.2 K.s^{-1}. The solid lines are the Darken simulation that incorporate parameters D_0, Q, ΔG and Ω.

Table 6.16: Parameters obtained from the Darken simulation (see figure 6.23) at heat rate of 0.2 K.s^{-1}. X in the parameter $\Omega_{\text{X-Cu}}$ denotes either In or S.

Impurities	D_0 (m^2.s^{-1})	Q (kJ.mol^{-1})	ΔG (kJ.mol^{-1})	$\Omega_{\text{X-Cu}}$ (kJ.mol^{-1})	$\Omega_{\text{In-S}}$ (kJ.mol^{-1})
In	1.0×10^{-5}	184.5	-61.4	3.0	–
In/S	–	–	–	–	-4.0
S	9.1×10^{-3}	213.6	-120.0	23.0	–

A summary of segregation parameters of In and S in Cu crystal obtained from Darken simulations is shown in table 6.17, 6.18 and 6.19. The segregation parameters measured for all heat rates are equivalent. In table 6.17, 6.18 and 6.19 the average values of segregation parameters D_0, Q, ΔG and Ω are shown for In and S. The activation energy (Q) and the pre-exponential factor (D_0) for In are smaller than for S. Therefore, it can be mentioned that S atoms have a high bulk diffusivity than In atoms in Cu crystal. The segregation energy for S ($\Delta G = -120.0$ kJ.mol^{-1}) is much higher (more negative) than that of In ($\Delta G = -60.4$ kJ.mol^{-1}). As a result, the segregation of S in more favourable than that of In, hence S replaced In in the surface during segregation measurements. A positive (attractive) interaction parameters for In ($\Omega_{\text{In-Cu}} = 3.0$ kJ.mol^{-1}) and S ($\Omega_{\text{S-Cu}} = 23.0$ kJ.mol^{-1}) interactions with Cu atoms and the negative (repulsive) paramenter for interaction of In and S atoms ($\Omega_{\text{In-Cu}} = -4.0$ kJ.mol^{-1}) lead to higher surface concentrations of In and S.

Table 6.17: A summary of In segregation parameters in Cu crystal obtained from Darken simulations.

Heat rate α (K.s^{-1})	In D_0 (m^2.s^{-1})	 Q (kJ.mol^{-1})	 ΔG (kJ.mol^{-1})	 $\Omega_{\text{In-Cu}}$ (kJ.mol^{-1})
0.025	1.8×10^{-5}	183.3	-57.2	3.0
0.05	2.2×10^{-5}	184.3	-62.8	3.0
0.1	1.4×10^{-5}	184.3	-60.0	3.0
0.2	1.0×10^{-5}	184.5	-61.4	3.0
Average:	1.6×10^{-5}	184.1	-60.4	3.0

Table 6.18: A summary of S segregation parameters in Cu crystal obtained from Darken simulations.

Heat rate	S			
α	D_0	Q	ΔG	$\Omega_{\text{S-Cu}}$
(K.s^{-1})	(m^2.s^{-1})	(kJ.mol^{-1})	(kJ.mol^{-1})	(kJ.mol^{-1})
0.025	9.6×10^{-3}	210.2	−120.0	23.0
0.05	8.8×10^{-3}	213.0	−120.0	23.0
0.1	9.0×10^{-3}	212.6	−120.0	23.0
0.2	9.1×10^{-3}	213.6	−120.0	23.0
Average:	9.1×10^{-3}	212.4	−120.0	23.0

Table 6.19: A summary of the interaction energies of In and S ($\Omega_{\text{In-S}}$) in Cu.

Heat rate α (K.s^{-1})	$\Omega_{\text{In-S}}$ (kJ.mol^{-1})
0.025	−4.0
0.05	−4.0
0.1	−4.0
0.2	−4.0
Average:	−4.0

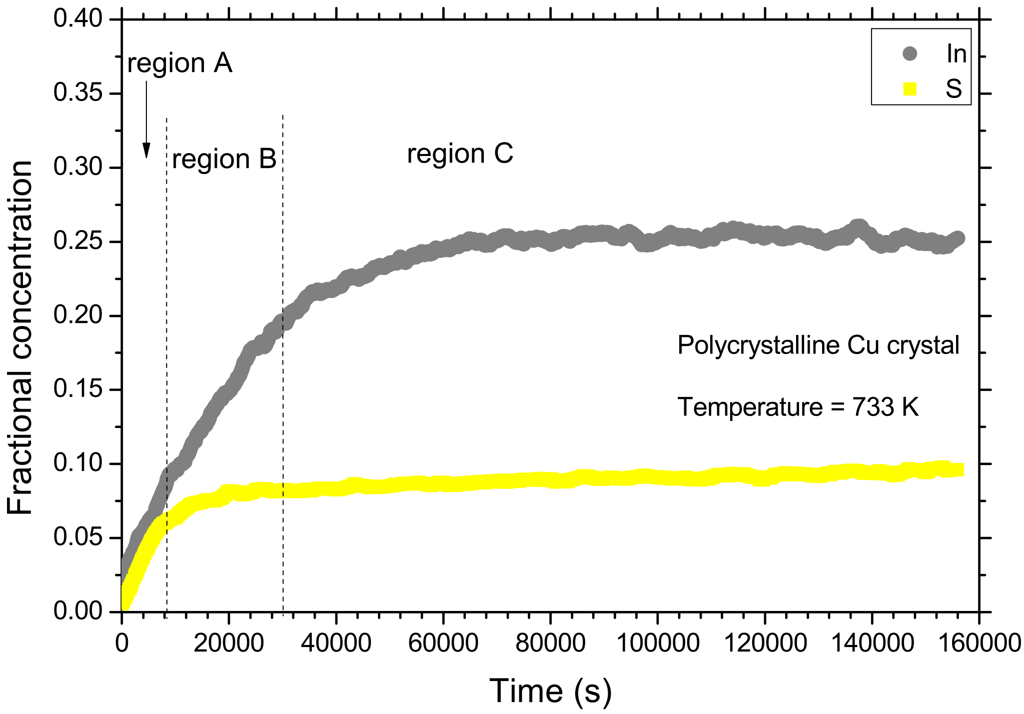

Figure 6.24: Fractional concentration as a function of time measured from a polycrystalline Cu crystal at a constant temperature of 733 K.

Constant temperature measurements

Figure 6.24, 6.25(a), 6.25(b), 6.26(a) and 6.26(b) shows the surface enrichment profiles of In and S in a dilute polycrystalline Cu crystal obtained with the constant temperature method for temperatures 733 K, 763 K, 793 K, 823 K and 853 K respectively. For a segregation profiles, there are three distinctive regions (shown in figure 6.24):

In region A, it can be seen that initially both In and S segregated to the surface and the segregation rate of both In and S is high. There is no interaction observed at these low surface concentrations. Therefore, a ternary Cu(In,S) alloy behaves as two Cu(In) and Cu(S) classical binary systems (this behaviour was demonstrated by Swart *et. al.* [37]).

In region B, the segregation rate of S decreased significantly and continued at slow rate. The segregation rate of In is still high from region A. A high segregation rate of In is due to high bulk concentration of In (0.059 at%), that is much higher than that of S (0.0008 at%). This statement can be supported by looking at the bulk diffusion rate ($D = D_0 \exp(-Q/RT)$) of In and S. Using the values of the activation energy (Q) and the pre-exponential factor (D_0) of In (Q = 184.1 kJ.mol^{-1} and $D_0 = 1.6 \times 10^{-5}$ m^2.s^{-1}) and S (Q = 212.4 kJ.mol^{-1} and $D_0 = 9.1 \times 10^{-3}$ m^2.s^{-1}) listed in table 6.17 and table 6.18 respectively. At temperature of 733 K, the diffusion rate of In is 1.2×10^{-18} m^2.s^{-1} and that of S is 6.6×10^{-18} m^2.s^{-1}. Evidently, the bulk diffusion rate of S is higher compared to that of In. Therefore, In is dominating the surface due to high bulk concentration.

In region C, the segregation rate of In decreased significantly and In reached a maximum coverage of $\approx$ 25 % (at temperatures 733 K, 763 K and 793 K) and $\approx$ 16 % (at temperatures 823 K and 853 K) and started to desegregate at slower rate. It can be seen clearly in figure 6.26(a) and 6.26(b) that at high temperatures the segregation rate of S is increasing and S atoms are replacing In atoms in the surface. Looking at the segregation energy for In (-60.4 kJ.mol^{-1}) and S (-120.0 kJ.mol^{-1}) (listed in table 6.17 and table 6.18) it follows that the segregation of S is more favourable than that of In hence S is replacing In.

In figure 6.24 the regions where there is a high bulk-to-surface segregation rate of S (region A) and In (region A to B) were fitted with semi-infinite solution of Fick's equation (Equation 3.15) as is shown in figure 6.27. The fittings were obtained for all temperatures (see figure 6.28(a), 6.28(b), 6.29(a) and 6.29(b)).

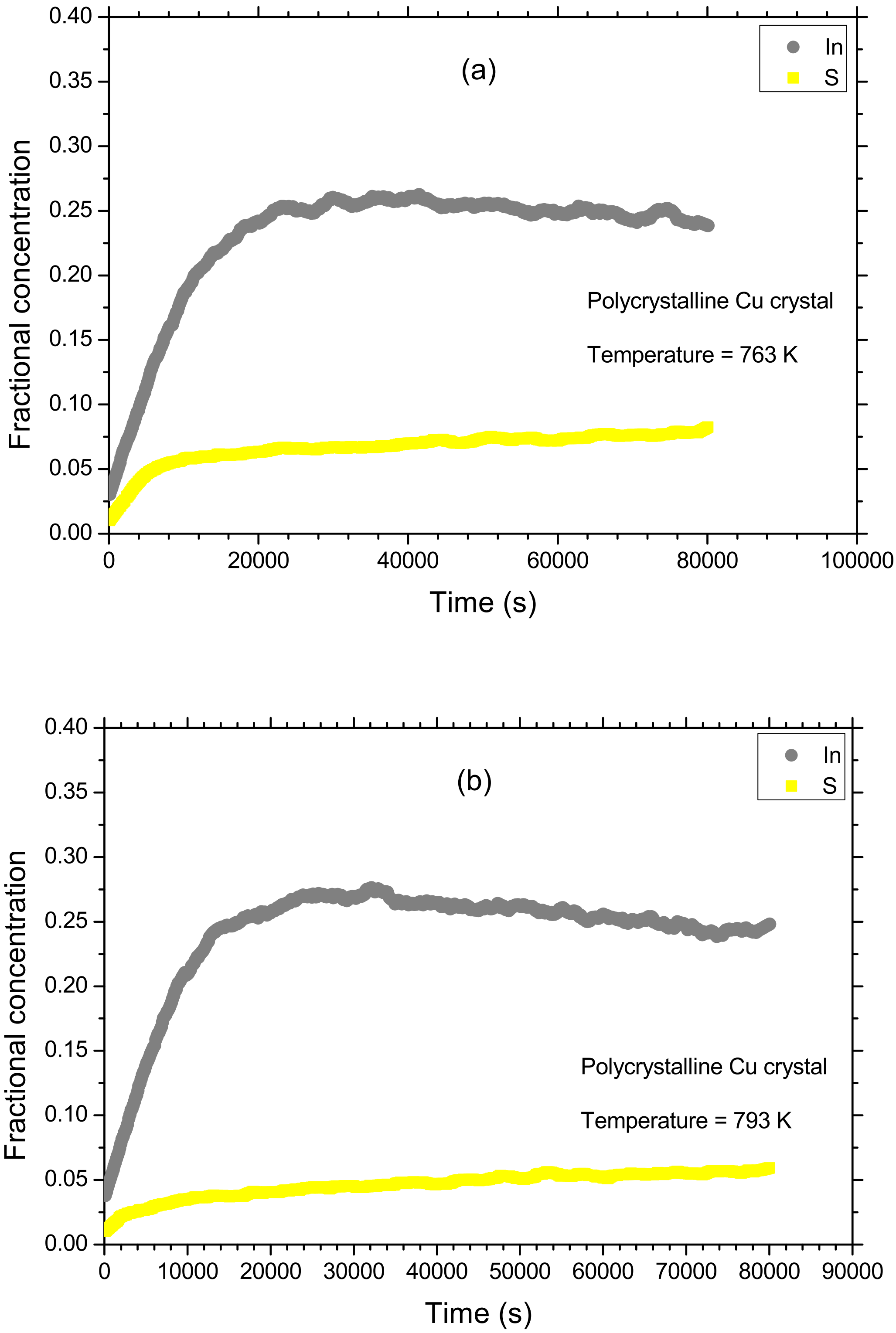

Figure 6.25: Fractional concentration as a function of time measured from a polycrystalline Cu crystal at a constant temperature of (a) 763 and (b) 793 K.

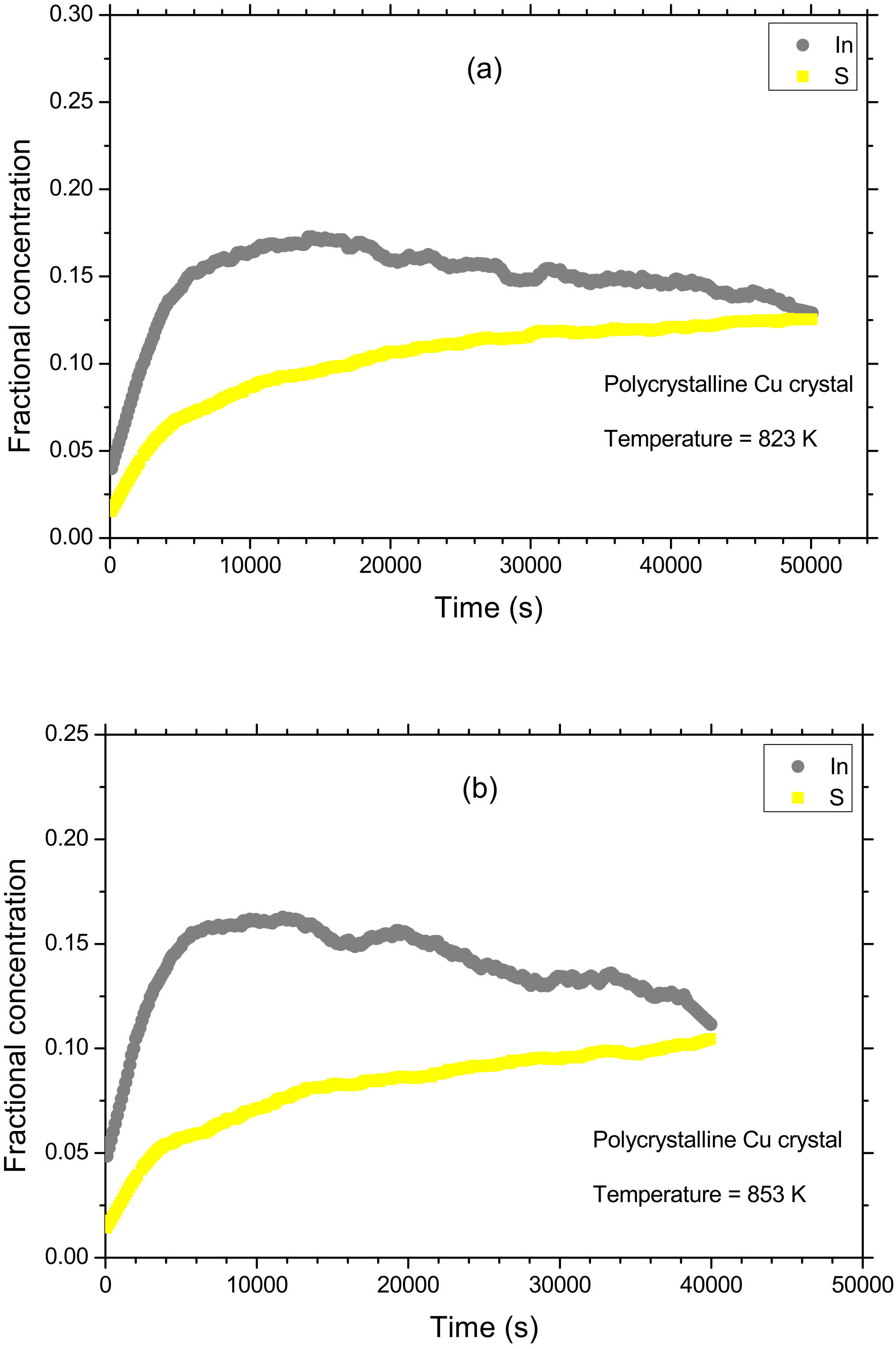

Figure 6.26: Fractional concentration as a function of time measured from a polycrystalline Cu crystal at a constant temperature of (a) 823 and (b) 853 K.

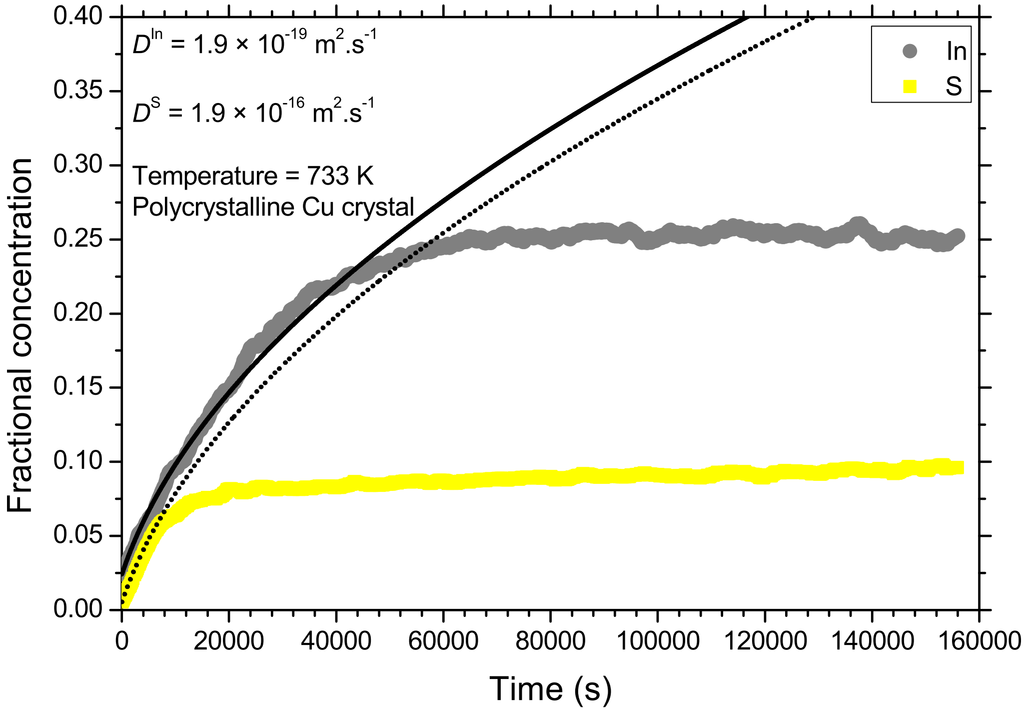

Figure 6.27: Fractional concentration as a function of time measured from a polycrystalline Cu crystal at a constant temperature of 733 K. The solid and broken lines are the best fit of the semi-infinite solution of Fick's equation that yield parameters D_0 and Q.

From each fit shown in figure 6.27, 6.28(a), 6.28(b), 6.29(a) and 6.29(b) the diffusion coefficients were obtained for both In and S and tabulated in table 6.20.

Table 6.20: Diffusion coefficients obtained from the best fit of the semi-infinite solution of Fick's equation for both In and S diffusion in Cu crystal.

Temperature (K)	In diffusion coefficient (D) (m^2.s^{-1})	S diffusion coefficient (D) (m^2.s^{-1})
733	1.9×10^{-19}	1.9×10^{-16}
763	1.0×10^{-18}	1.0×10^{-15}
793	2.0×10^{-18}	1.6×10^{-15}
823	9.9×10^{-18}	8.9×10^{-15}
853	1.5×10^{-17}	2.1×10^{-14}

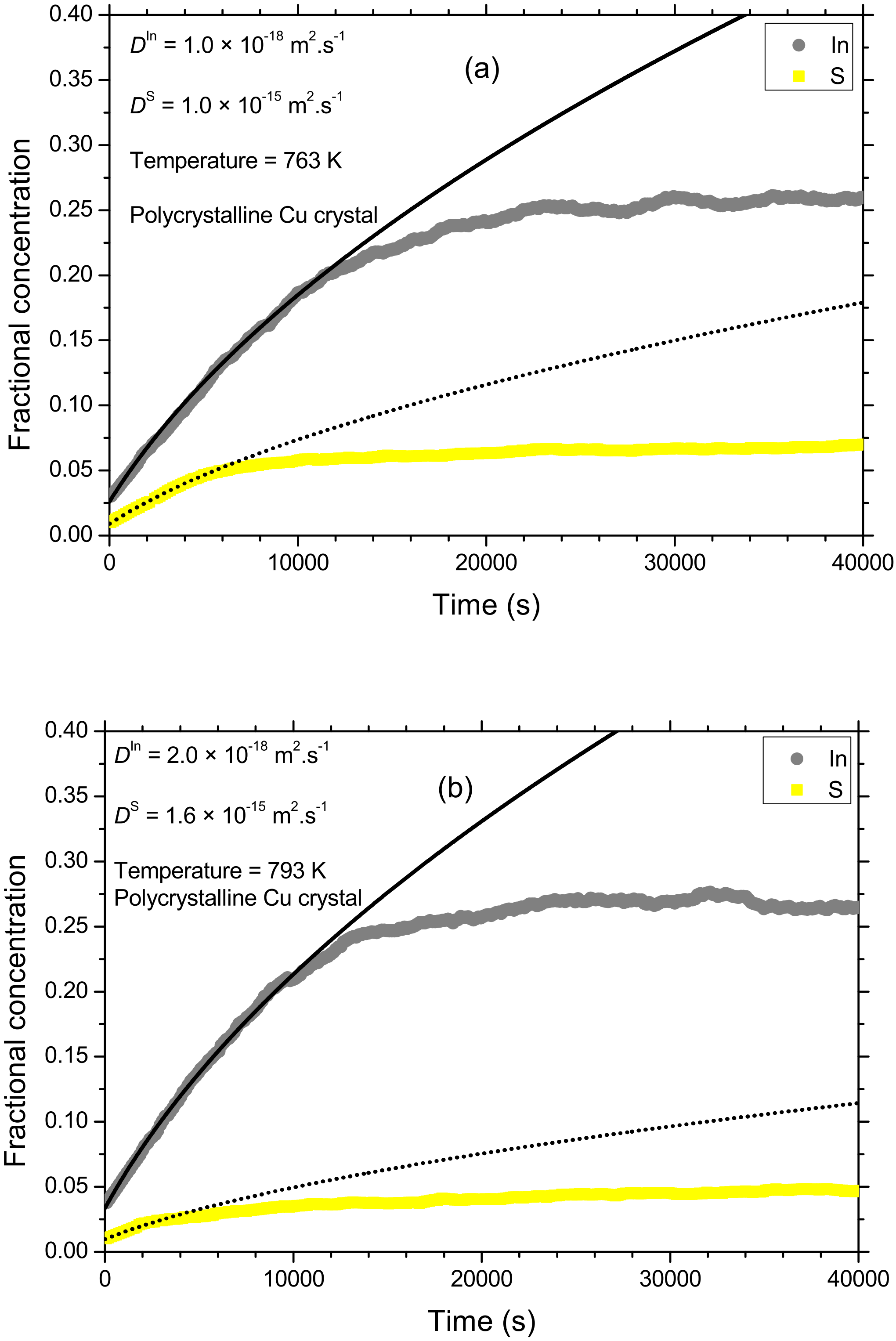

Figure 6.28: Fractional concentration as a function of time measured from a polycrystalline Cu crystal at a constant temperature of (a) 763 and (b) 793 K. The solid and broken lines are the best fit of the semi-infinite solution of Fick's equation that yield parameters D_0 and Q.

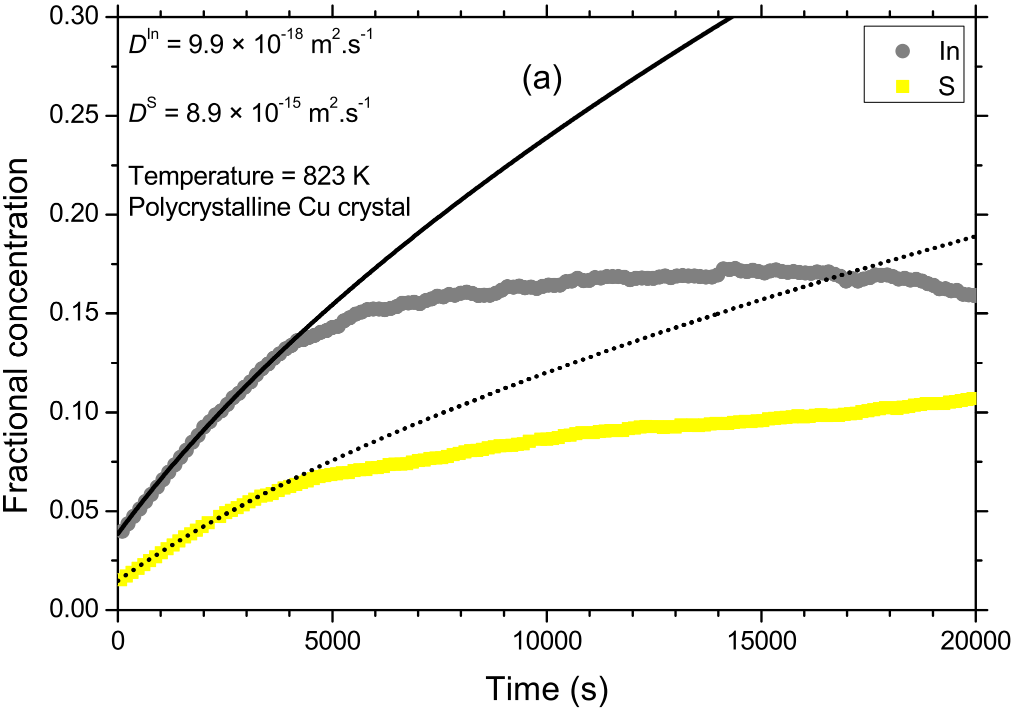

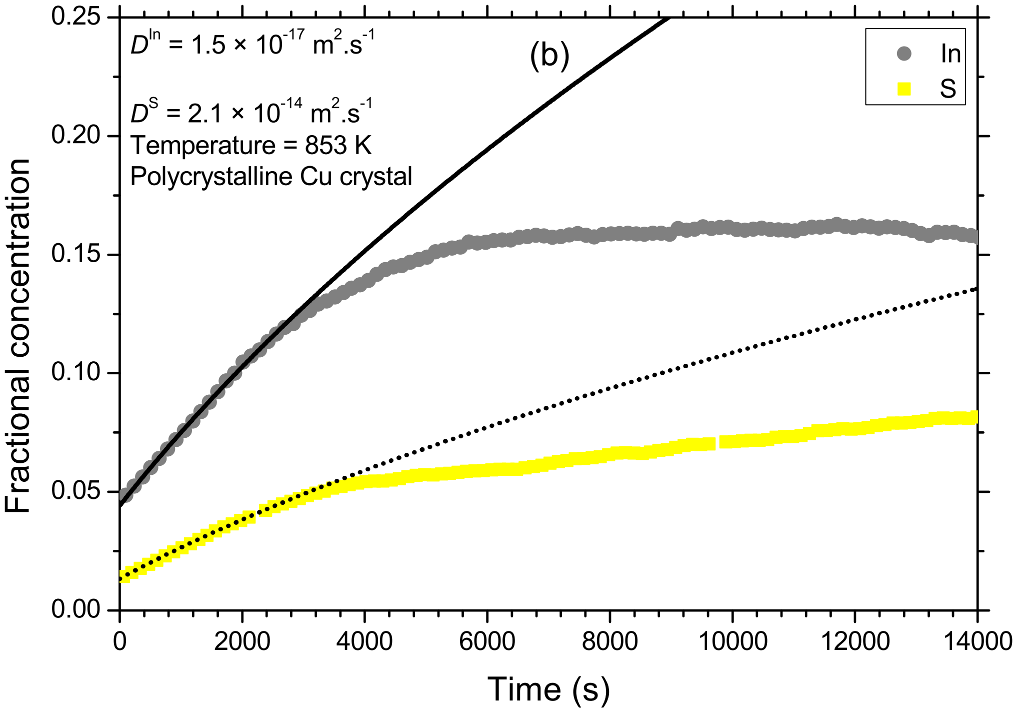

Figure 6.29: Fractional concentration as a function of time measured from a polycrystalline Cu crystal at a constant temperature of (a) 823 and (b) 853 K. The solid and broken lines are the best fit of the semi-infinite solution of Fick's equation that yield parameters D_0 and Q.

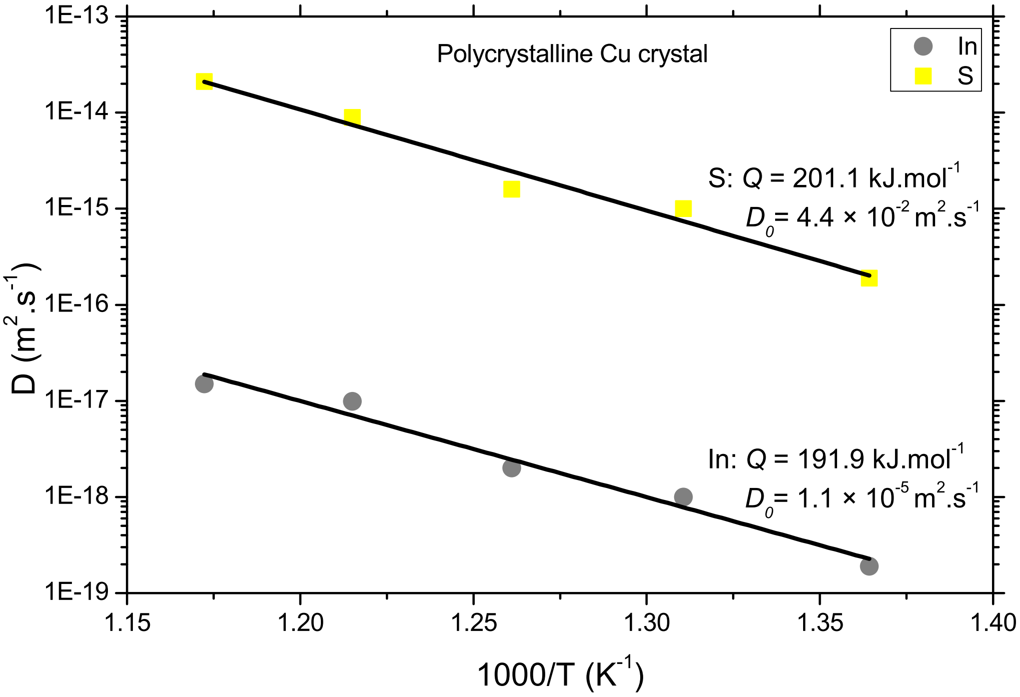

Figure 6.30: Arrhenius plot of diffusion coefficients obtained from the best fit of the semi-infinite solution of Fick's equation for both In and S segregation in polycrystalline Cu crystal.

The parameters shown in table 6.20 were plotted as an Arrhenius plot in figure 6.30 and from the best fit line through the data points the segregation parameters (Q and D_0) were obtained for both In and S segregation in polycrystalline Cu crystal and listed in table 6.21.

Table 6.21: The segregation parameters of In and S in polycrystalline Cu crystal obtained from constant temperature measurements.

Impurities	D_0 ($m^2.s^{-1}$)	Q ($kJ.mol^{-1}$)
In	1.1×10^{-5}	191.9
S	4.4×10^{-2}	201.1

In figure 6.30 it is clear that S has a higher bulk diffusion coefficient than In. Therefore, fast In enrichment in the surface was due to high bulk concentration.

7

Conclusive Summary

In In/Cu thin films, the In layer reacted with the Cu layer during deposition to form two intermetallic phases namely $CuIn_2$ and $Cu_{11}In_9$. The In/Cu thin films results of the annealed thin films showed that in the temperature range between 150 and 300 ℃ the phases that formed, were $CuIn_2$ followed by $Cu_{11}In_9$ and lastly the formation of Cu_2In. The XRD data was supported by In/Cu AES depth profiles that illustrated that In diffused deeper into the Cu layer. A phase transition in In/Cu thin films correspond to a change in the melting point of Cu_xIn_y phases from low temperatures ($<$ 150 ℃) to high temperatures ($<$ 1084.6 ℃) as Cu diffuse into the In rich side of In/Cu films. This phenomenon was successfully used to dope polycrystalline Cu crystals with In that has a very low melting point.

Bulk-to-surface segregation of In in polycrystalline Cu crystal was observed. A regular impurity S (a strong segregant), of a Cu crystal segregated with In. From the segregation profiles, the segregation parameters were successfully obtained for surface segregation of In and S in polycrystalline Cu crystal using both the linear and constant temperature method. The parameters were listed in table 7.1, 7.2 and 7.3.

Table 7.1: Segregation parameters of In segregation in Cu crystal.

Method	In			
	D_0 ($m^2.s^{-1}$)	Q ($kJ.mol^{-1}$)	ΔG ($kJ.mol^{-1}$)	$\Omega_{\text{In-Cu}}$ ($kJ.mol^{-1}$)
Linear heat	1.6×10^{-5}	184.1	-60.4	3.0
Constant heat	1.1×10^{-5}	191.9	-	-

Table 7.2: Segregation parameters of S segregation in Cu crystal.

Method	S			
	D_0 ($m^2.s^{-1}$)	Q ($kJ.mol^{-1}$)	ΔG ($kJ.mol^{-1}$)	$\Omega_{\text{S-Cu}}$ ($kJ.mol^{-1}$)
Linear heat	9.1×10^{-3}	212.4	-120.0	23.0
Constant heat	4.4×10^{-2}	201.1	-	-

Table 7.3: The interaction energy of In and S ($\Omega_{\text{In-S}}$) in Cu crystal.

Method	$\Omega_{\text{In-S}}$ ($kJ.mol^{-1}$)
Linear heat	-4.0

The activation energy (Q) and the pre-exponential factor D_0 for In bulk diffusion are smaller than for S. Therefore, S diffuses faster in the bulk than In. The activation energy for In is lower than that for S. As a result In segregates first (before S) at low temperatures. From the segregation energy for In ($\Delta G = -60.4$ $kJ.mol^{-1}$) and S ($\Delta G = -120.0$ $kJ.mol^{-1}$) it follows that the segregation of S is more favourable than that of In. The attractive interaction energy between In atoms and Cu atoms ($\Omega_{\text{In-Cu}} = 3.0$ $kJ.mol^{-1}$) indicates a tendency of compound formation between In and Cu atoms. Similarly, the attractive interaction energy between S atoms and Cu atoms ($\Omega_{\text{S-Cu}} = 23.0$ $kJ.mol^{-1}$) indicates a tendency of compound formation between S and Cu atoms. A strong repulsion energy between the In and S atoms ($\Omega_{\text{In-S}} = -4.0$ kJ.mol^{-1}) shows less or no tendency of In-S compound formation.

The segregation parameters (Q and D_0) obtained in this study for In segregation ($Q = 191.9$ kJ.mol^{-1}, $D_0 = 1.1 \times 10^{-5}$ m^2.s^{-1} for constant temperature mesurements and $Q = 184.1$ kJ.mol^{-1}, $D_0 = 1.6 \times 10^{-5}$ m^2.s^{-1} for linear temperature mesurements) from a Cu crystal compare well with those reported in literature for In tracer diffusion ($Q = 196.3$ kJ.mol^{-1}, $D_0 = 1.9 \times 10^{-4}$ m^2.s^{-1} [9], $Q = 193.5$ kJ.mol^{-1}), $D_0 = 1.3 \times 10^{-4}$ m^2.s^{-1} [10] and $Q = 178.0$ kJ.mol^{-1}, $D_0 = 0.2 \times 10^{-4}$ m^2.s^{-1} [11]) in a Cu(In) bulk system.

The segregation parameters (Q and D_0) obtained in this study for S segregation ($Q = 201.1$ kJ.mol^{-1}, $D_0 = 4.4 \times 10^{-2}$ m^2.s^{-1} for constant temperature mesurements and $Q = 212.4$ kJ.mol^{-1}, $D_0 = 9.1 \times 10^{-3}$ m^2.s^{-1} for linear temperature mesurements) from a Cu crystal compare well with those reported in literature for both S segregation ($Q = 216.0$ kJ.mol^{-1}, $D_0 = 8.1 \times 10^{-3}$ m^2.s^{-1} for constant temperature mesurements [5] and $Q = 212.0$ kJ.mol^{-1}, $D_0 = 1.8 \times 10^{-3}$ m^2.s^{-1} for linear temperature mesurements [5]) from a Cu crystal and S tracer diffusion ($Q = 205.1$ kJ.mol^{-1}, $D_0 = 2.3 \times 10^{-4}$ m^2.s^{-1} [42]) in a Cu(S) bulk system.

7.1 Suggestions for future work

This study can be carried out in Cu single crystals to observe how different surface orientations of Cu single crystals influences the bulk diffusion of In in Cu crystals. Cu single crystals can be doped with different bulk concentrations of In to observe the effect of different In bulk concentration on the segregation behaviour of In in

Cu crystal. Furthermore, Copper-Indium-Selenium ($CuInSe_x$) is used as absorber in solar cell industry. Cu(In) alloy can be doped with Se to observe how Se influences the segregation behaviour of In.

A

Appendix

A.1 Conferences/Contributions

1. **Auger electron spectroscopy and X-ray diffraction study of thin films**

   MJ Madito, HC Swart and JJ Terblans

   8th Annual Inkaba yeAfrica Workshop at GeoSynthesis 2011, CTICC, Cape Town, South Africa.

2. **Quantitative Investigation of Cu/In thin Films Deposited onto SiO_2 by Electron Beam Evaporation**

   MJ Madito, HC Swart and JJ Terblans

   Inkaba yeAfrica-Platinum Value Chain BMBF-AMREP Programme Initiative Definition Workshop 2011, Rustenburg, South Africa.

3. **Ion sputtering yield coefficients from In thin films bombarded by different energy Ar^+ ions**

   MJ Madito, HC Swart and JJ Terblans

   56th Annual Conference of the South African Institute of Physics (SAIP) 2011, UNISA, Pretoria, South Africa.

4. **AES and XRD study of In/Cu thin films deposited onto SiO_2 by electron beam evaporation**

   MJ Madito, HC Swart and JJ Terblans

   56th Annual Conference of the South African Institute of Physics (SAIP) 2011, UNISA, Pretoria, South Africa.

5. **Quantitative Investigation of Cu/In thin Films Deposited onto SiO_2 by Electron Beam Evaporation**

   MJ Madito, HC Swart and JJ Terblans

   55th Annual Conference of the South African Institute of Physics (SAIP) 2010, CSIR, Pretoria, South Africa.

Bibliography

[1] W.H. Lee, B.S. Cho, B.J. Kang, H.J. Yang, and J.G. Lee, Applied Physics Letters 79 (2001) 3962.

[2] S. Takayama and N. Tsutsui, Journal of Vacuum Science and Technology B 14 (1996) 3257.

[3] C.S. Hsu, H.Y. Hsieh, J.S. Fang, Journal of Electronic Materials 37 (2008) 6.

[4] E.C. Viljoen and J. du Plessis, Surface and Interface Analysis 22 (1994) 598.

[5] E.C. Viljoen and J. du Plessis, Surface and Interface Analysis 23 (1995) 110.

[6] J.J. Terblans. and G.N. van Wyk, Surface and Interface Analysis 36 (2004) 935.

[7] J.Y. Wang, J. du Plessis, J.J. Terblans and G.N. vanWyk, Surface Science 423 (1999) 12.

[8] J.J. Terblans, H.C. Swart, e-Journal of Surface Science and Nanotechnology 7 (2009) 480.

[9] G. Krautheim, A. Neidhardt, U. Reinhold, Kristall und Technik (13) 11 (1978) 1335.

[10] V.A. Gorbachev, S.M. Klotsman, Ya.A. Rabovskiy, V.K. Talinskiy and A.N. Timofeyev, Fiz Metal Metalloved (34) 4 (1972) 884.

[11] W. Gust, C. Ostertag, B. Predel, U. Roll, A. Lodding, H. Odelius, Philosophical Magazine A (47) 3 (1983) 395.

[12] A.M. Alfantazi , R.R. Moskalyk, Minerals Engineering 16 (2003) 687.

[13] J. Hertz, K. El Aissaoui, L. Bouirden, Journal of Phase Equilibria (23) 6 (2002) 473.

[14] A.A. Wronkowska, A. Wronkowski, Ł. Skowroński, Journal of Alloys and Compounds 479 (2009) 583.

[15] J.S. Fang, H.Y. Hsieh, Journal of Electronic Materials (36) 2 (2007) 129.

[16] Z. Bahari, E. Dichi, B. Legendre, J. Dugué, Thermochimica Acta 401 (2003) 131.

[17] W. William, S.S. Choe, R. Chuang, C.C. Lee, Thin Solid Films 376 (2000) 164.

[18] W. Keppner, R. Wesche, T. Klas, J. Voigt and G. Schatz, Thin Solid Films 143 (1986) 201.

[19] Ž. Marinković, V. Simić, Thin Solid Films 217 (1992) 26.

[20] K.A. Lindahl, J.J. Moore, D.L. Olson, R. Noufi, B. Lanning, Thin Solid Films 290 (1996) 518.

[21] V. Simić, Ž. Marinković, Thin Solid Films 209 (1992) 181.

[22] I. Manna, S. Bader, W. Gust, B. Predel, Physica Status Solidi (a) 119 (1990) K9.

[23] P.T. Vianco, A.C. Kilgo, R. Grant, Journal of Materials Science (30) (1995) 4871.

[24] D.G. Kim, C.Y. Lee, S.B. Jung, Journal of Materials Science: Materials in Electronics 15 (2004) 95.

[25] D.R. Askeland, P.P. Phulé, The Science and Engineering of Materials, Canada, Thomson, 2006.

[26] M.P. Seah, in: Practical Surface Analysis by Auger and X-ray Photoelectron Spectroscopy, Volume 1, 2nd edition, D. Briggs and M.P. Seah (Editors), Chichester, John Wiley & Sons Ltd., 1990.

[27] J. Crank, The Mathematics of Diffusion, 2nd edition, Clarendon Press, Oxford, 1975.

[28] J. Du Plessis, Solid State Phenomena - Part B, Volume 11 (Diffusion and Defect Data), Sci-Tech Publications, Brookfield USA, 1990.

[29] J. Du Plessis, P. E. Viljoen, and G. N. Van Wyk, Surface Science 244 (1991) 277.

[30] E.C. Viljoen, J. du Plessis, Surface Science 431 (1999) 128.

[31] P.A. Dowben, A.H. Miller, R.W. Vook, Gold Bull 20 (1987) 3.

[32] H.D. Joubert, H.C. Swart, J.J. Terblans, Surface and Interface Analysis 37 (2005) 1027.

[33] C.H.P. Lupis, Chemical Thermodynamics of Materials, North-Holland, Amsterdam, 1983.

[34] S. Stølen, T. Grande, Chemical Thermodynamics of Materials, John Wiley & Sons Ltd, 2004.

[35] G.N. Lewis, M. Randall, Thermodynamics, 2^{nd} edition, McGraw-Hill, New York, 1961.

[36] F.F.D. Chabert, F. Tancret, F. Christien, R.L. Gall, J. Castagne. Journal of Material Science 4 (2007) 9765.

[37] H.C. Swart, W.D. Roos and J.J. Terblans, Surface and Interface Analysis 36 (2004) 285.

[38] J.M. Walls, Methods of Surface Analysis, Cambridge University Press, 1989.

[39] R. Shimizu, Japanese Journal of Applied Physics 22 (1983) 1631.

[40] S. Tanuma, C.J. Powell and D.R. Penn, Surface and Interface Analysis 36 (2004) 1.

[41] B.M. Başol, Thin Solid Films 361 (2000) 514.

[42] R.C. Weast, M.J. Astle (Editors), CRC Handbook of Chemistry and Physics, 63^{rd} edition, CRC Press, Inc., 1982.